ALAA SAMIR OUDA

STRATEGIES FOR CONTROLLING NUCLEATION AND CRYSTAL GROWTH IN MEMBRANE DISTILLATION CRYSTALLISATION

SCHOOL OF WATER, ENERGY AND ENVIRONMENT
WATER

PhD
Academic Year: 2018- 2023

Supervisor: Professor Ewan McAdam
Associate Supervisor: Dr Yadira Bajón Fernández
June 2023

SCHOOL OF WATER, ENERGY AND ENVIRONMENT
WATER

PhD

Academic Year 2018 - 2023

ALAA SAMIR OUDA

STRATEGIES FOR CONTROLLING NUCLEATION AND CRYSTAL GROWTH IN MEMBRANE DISTILLATION CRYSTALLISATION

Supervisor: Professor Ewan McAdam
Associate Supervisor: Dr Yadira Bajón Fernández
June 2023

This thesis is submitted in partial fulfilment of the requirements for the degree of PhD

© Cranfield University 2023. All rights reserved. No part of this publication may be reproduced without the written permission of the copyright owner.

ACADEMIC INTEGRITY DECLARATION

I declare that:

- the thesis submitted has been written by me alone.
- the thesis submitted has not been previously submitted to this university or any other.
- that all content, including primary and/or secondary data, is true to the best of my knowledge.
- that all quotations and references have been duly acknowledged according to the requirements of academic research.

I understand that to knowingly submit work in violation of the above statement will be considered by examiners as academic misconduct.

Abstract

Membrane distillation crystallisation (MDC) is a promising technology that can address the primary restriction of regulating supersaturation rate in conventional crystallisation technologies, thus affording good control over nucleation and crystal growth. The supersaturation rate (R') was used as a key parameter to govern the onset of nucleation (induction time) instead of irreversible flux decline, which is typically used in previous MDC studies. In this work, in-line turbidimetry enabled the precise determination of the induction time and metastable zone width (MSZW), which have been correlated to the supersaturation rate for a detailed characterisation of the nucleation kinetics and growth mechanism. The supersaturation at which nucleation occurred was measured within the interfacial boundary layer and bulk solution to differentiate between two scaling mechanisms (crystal adhesion or deposition) associated with the underlying nucleation mechanism based on classical nucleation theory. This allowed the MDC to decouple surface scaling from bulk nucleation at specific MSZW regions where the achieved crystallisation trajectory could balance between crystal quality and reduced membrane scaling. The increased supersaturation rate independent of the boundary layer enabled the transition towards a homogeneous nucleation mechanism where scaling is minimised, which aligns with classical nucleation theory but contradicts previous MDC studies. The consistent and reproducible nucleation kinetics obtained in this study while controlling multiple supersaturation factors suggested crystallisation to be inherently scalable, which is a unique facet compared to conventional crystallisers. Furthermore, the ability to sustain the supersaturation profile following nucleation enabled the system to reposition the crystallisation trajectory close to the MSZW threshold, providing high potential for nucleation kinetic control while regulating crystal size, size distribution and yield. Therefore, the kinetic framework established in this work offers advanced control over the nucleation mechanism and growth phase, which can be employed to fulfil commercial requirements for zero liquid discharge and more valuable crystalline products.

Keywords: Hollow fibre; Nucleation; Crystal growth; Scale-up; Induction time; MSZW; Scaling.

Acknowledgements

"Say, indeed, my prayer, my rites of sacrifice, my living, and my dying are for Allah, Lord of the worlds". I am thankful to Almighty Allah, who guided and helped me complete this journey.

First and foremost, I would like to express my deepest gratitude to my supervisor, Prof. Ewan McAdam, for his endless support, for sharing his knowledge, and for having confidence in me. Thanks also to Dr. Yadira Bajón Fernández for her guidance and suggestions. I am also very grateful to Dr. Chris, Dr. Mehrez, and Dr. Navya for their valuable technical assistance.

My heartfelt gratitude goes to my small family, Hasan and Eman, for their smiles, and to my large family in Palestine, especially my mother and father, for their love and encouragement.

Rawan, thanks for being here and for your unwavering support during my PhD journey; you were my pillar of strength.

To our Palestinian martyrs, prisoners, and injured, you will always be remembered, hoping for Palestine to be liberated.

Lastly, I always say, "Where should we go after the last frontiers, where should the birds fly after the last sky?"

Table of Contents

ACADEMIC INTEGRITY DECLARATION i
Abstract ii
Acknowledgements iv
List of Figures viii
List of Figures for Appendices xii
List of Tables xiv
List of Equations xv
List of Equations for Appendices xviii
List of Abbreviations xix
1 Introduction 1
1.1 Crystallisation concepts and applications 1
1.2 Membrane distillation crystallisation: Next generation of resource recovery 7
1.3 Nucleation and crystal growth control in MDC: including scaling 12
1.4 Aim and objectives 15
1.5 Thesis structure 15
1.6 References 18
2 Modifying supersaturation rate with membrane area to volume ratio: scaling reduction and improved crystal growth control in membrane distillation crystallisation 26
2.1 Introduction 28
2.2 Materials and methods 31
2.2.1 Laboratory set-up for membrane distillation crystallisation experiments 31
2.2.2 Characteristics of produced crystals and membrane surface scaling 33
2.2.3 Mass and heat transfer characterisation in membrane distillation 34
2.2.4 Nucleation kinetics characterisation 35
2.3 Result and discussion 37
2.3.1 Impact of increasing membrane area on nucleation at fixed flux 37
2.3.2 Shifting induction time by using membrane area to increase concentration rate 41
2.3.3 Supersaturation rate defines the primary nucleation mechanism 45
2.3.4 How supersaturation rate determines crystal growth characteristics 52
2.4 Conclusions 55
2.5 Acknowledgements 56
2.6 Appendix A 57
2.7 References 58

3 Methods to modify supersaturation rate in membrane distillation crystallisation: control of nucleation and crystal growth kinetics (including scaling) 64
3.1 Introduction 67
3.2 Materials and methods 69
3.2.1 MDC experimental setup 69
3.2.2 Characterisation of nucleation, crystallisation and surface scaling 71
3.2.3 Data analysis 71
3.3 Result and discussion 75
3.3.1 Characterising flux and induction time to transform into supersaturation rate 75
3.3.2 Supersaturation rate sets the position for nucleation within the metastable zone 78
3.3.3 Supersaturation rate determines extent of membrane scaling in MDC 83
3.3.4 Crystal growth is defined by the MSZW and supersaturation rate 87
3.4 Conclusion 89
3.5 Acknowledgements 91
3.6 Appendix A 91
3.7 References 96
4 Facile supersaturation control strategies for membrane distillation 102
4.1 Introduction 105
4.2 Materials and methods 109
4.2.1 Experimental setup 109
4.2.2 Crystals and membrane scaling analysis 111
4.2.3 Mass and heat transfer in membrane distillation 112
4.2.4 Characterisation of nucleation and crystal growth kinetics 114
4.3 Result and discussion 115
4.3.1 Consistent primary nucleation is achieved with or without in-line filtration 115
4.3.2 Distinct supersaturation profiles develop when increasing membrane area 119
4.3.3 Supersaturation trajectory determines crystal size, size distribution and morphology 126
4.4 Conclusions 134
4.5 Acknowledgements 136
4.6 Appendix A 136
4.7 References 139
5 Discussion 145
5.1 MDC can be described through classical nucleation theory (CNT) 145
5.2 Controlling crystal size, size distribution, and morphology in MDC 148

5.3 The potential to design MDC for sustained and reproducible crystal growth 150
5.4 MDC is more scalable than classical crystallisation systems 152
5.5 References 155
6 Conclusions and future work 159
6.1 Conclusions 159
6.2 Future work 161

List of Figures

Figure 1.1 *The relationship between induction time and supersaturate at induction during transition across MSZW* 2

Figure 1.2 *Thermal boundary layer in Conventional crystalliser* 7

Figure 1.3 *Boundary layer in membrane distillation crystallisation* 10

Figure 1.4 *Thesis structure* 17

Figure 2.1 *MSZW as function of temperature and concentration.* 29

Figure 2.2 *Schematic diagram of the Membrane Distillation Crystallisation setup.* 33

Figure 2.3 *Permeation flux during MCr operation time for different membrane modules: (a) over time; and (b) evidencing flux decline against the progressively supersaturated fluid. Boundary conditions: Tbulk , 55±1°C; ∆Tmembrane, 20±2°C; initial feed NaCl concentration, 23.9 wt.%. Standard error of permeation flux was calculated based on differences in triplicate measurements for each membrane modules; 1 HF, 3.8±0.3; 3HF, 3.4±0.5; 7HF, 3.2±0.3; 19HF, 3.1±0.3; 25HF, 3.3±0.1; 37HF, 2.8±0.1.* 38

Figure 2.4 *Turbidity profile during MCr operation for membranes comprised of increasing surface area: (a) based on operating time; (b) based on bulk supersaturation. Boundary conditions: Tbulk, 55±1°C; ∆Tmembrane, 20±2°C; initial feed NaCl concentration, 23.9 wt.%.* 40

Figure 2.5 *A broad metastable region is created by increasing membrane area at fixed flux. Boundary conditions: Tbulk , 55±1°C; ∆Tmembrane, 20±2°C; initial feed NaCl concentration, 23.9 wt.%.* 41

Figure 2.6 *The CPC and TPC of supersaturation at induction over different concentration rate (LnR'). bulk (°C) = (55±1), ∆T membrane (°C) = (20±2), Velocity of feed and permeate = 0.06 m s^{-1}, initial feed concentration NaCl (wt. %) = 23.9.* 42

Figure 2.7 *(a) The dependence of ∆cfm, max on concentrating rate (ln R') according to equation (20) for different membrane modules, (b) The dependence of induction time on concentrating rate (LnR') for different membrane modules, bulk (°C) = (55 ±1), ∆T membrane (°C) = (20 ±2), velocity of feed and permeate = 0.06 m s^{-1}, initial feed concentration NaCl (wt. %) = 23.9.* 44

Figure 2.8 *Supersaturation degree of bulk and membrane over different concentration rate (LnR'), bulk (°C) = (55 ±1), ∆T membrane (°C) = (20 ±2), velocity of feed and permeate = 0.06 m s^{-1}, initial feed concentration NaCl (wt. %) = 23.9.* 45

Figure 2.9 *Membrane crystal adhesion for modules of different surface area, which indicates the reduction in surface nucleation with an increase in concentration rate.* 46

Figure 2.10 *Scanning electron microscope (SEM) images highlighting reduced surface adhesion (scaling) as concentration rate increases through an increase in membrane area. Scale bar: 1mm.* 47

Figure 2.11 *ln (t_{ind}) versus 1/ln^{2}S for different membrane modules show different nucleation mechanism. The change in slope indicates different nucleation mechanism as reported in* [53]. 48

Figure 2.12 *Scanning electron microscope (SEM) images of membrane pores from membranes used in different sized modules, illustrating how the increase in concentration rate with membrane area reduces nucleation within the pore structure. Scale bar, 50µm. (a) 7HF; (b) 19HF; (C) 25HF.*..... 51

Figure 2.13 *Crystal yield produced in the bulk solution when using membranes modules of different size to increase concentration rate.* 52

Figure 2.14 *Crystals Size Distribution (CSD) based on volume fraction (%).* ... 53

Figure 2.15 *Scanning electron microscope (SEM) images of: (a) crystals produced from 1HF experiment (scale bar, 50µm), (b) crystals produced from 37 HF experiment, evidencing distinct growth patterns upon increasing concentration rate.* 55

Figure 3.1 *Schematic diagram of the MDC setup.* 70

Figure 3.2 *Average permeation flux before induction and supersaturation rate for different primary supersaturation parameters: (A) 37HF, 23.92%wt, ∆T 20±2°C; (B) 7HF, 23.92%wt, ∆T 20±2°C; (C) 37HF, 23.92%wt, ∆T 10±2°C; (D): 37HF, 25.92%wt,∆T= 20°±2C. Boundary conditions: Tbulk,55 ±1°C; feed and permeate velocity, 0.06 m s^{-1}.* 76

Figure 3.3 *Permeation flux for 37 HF module across the solution volumes tested. Boundary conditions: T_{bulk},55±1°C; ∆T membrane, 20±2°C; feed and permeate velocity, 0.06 m s^{-1}; initial feed concentration 23.9wt.% NaCl. Standard error of permeation flux was calculated based on differences in triplicate measurements for each volume; 900 ml, 2.85±0.16; 700 ml, 2.76±0.11; 500 ml, 2.83±0.13; 340 ml, 2.77±0.07; 270 ml, 2.82±0.04.* 77

Figure 3.4 *Turbidity profile for the 37 HF module operation. The supersaturation data reported is based on bulk conditions at different supersaturation rates across the solution volumes tested. Boundary conditions: T_{bulk},55±1°C; ∆T membrane, 20±2°C; feed and permeate velocity, 0.06 m s^{-1}; initial feed concentration 23.9wt.% NaCl.* 78

Figure 3.5 *(a) Bulk and membrane film supersaturation at induction based on concentrating rate (LnR') adjusted by membrane area; (b) Metastable region characterised following the increase in area to volume ratio (A/V_o); (c) dependence of $\Delta c_{fm,max}$ in the film on concentrating rate (LnR') according to*

eq.27. Boundary conditions: T_{bulk},55±1°C; ∆T20±2°C; feed and permeate velocity, 0.06 m s^{-1}; initial feed concentration 23.9 wt.% NaCl. 81

Figure 3.6 *The dependence of $\Delta c_{max,fm}$ in the membrane film on concentrating rate (LnR') for two sets of supersaturation rate parameters: (a) ∆T; and (b) different initial feed concentrations. Boundary conditions: T_{bulk}, 55±1°C; feed and permeate velocity, 0.06 m s^{-1}.* 82

Figure 3.7 *Characterisation of induction time ($ln(_{tind})$) and supersaturation ($1/ln^2S$) at induction for different supersaturation parameters. Two distinct slopes are determined with the shallow slop infers a region dominated by primary heterogenous nucleation, while the steeper slope is characterised by a primary homogeneous nucleation mechanism at higher supersaturation. Boundary conditions: T_{bulk}, 55±1°C; feed and permeate velocity, 0.06 m s^{-1}.* 83

Figure 3.8 *Extent of membrane scaling: (a) 37 HF module using different supersaturation parameters; and (b) comparison of crystal mass recovered from the bulk solution and from the membrane surface when using different supersaturation parameters. Boundary conditions: T_{bulk}, 55±1°C; feed and permeate velocity, 0.06 m s^{-1}.* 86

Figure 3.9 *Crystal size distributions presented as box-whisker plots: (a) ∆T; (b) membrane area; and (c); different initial concentrations. Each parameter provides adjustment of one principal component of either supersaturation rate, supersaturation or induction time. Box represents upper and lower quartiles (25^{th} and 75^{th} percentiles), median size is indicted by the line within the box, and the whiskers represent the limited of the size distribution (0^{th} and 100^{th} percentiles). Boundary conditions: T_{bulk}, 55±1°C; feed and permeate velocity, 0.06 m s^{-1}; initial feed solution volume, 270ml.* 88

Figure 4.1 *(A) An illustration of metastable zone width boundaries; and (B) Schematic representation of the different supersaturation trajectories across the metastable zone width. For trajectory A, supersaturation rate following induction is greater than nucleation rate (R >J); trajectory B, supersaturation rate is equal to nucleation rate following induction (R=J); and trajectory C, supersaturation rate following induction is lower than nucleation rate (R<J).* 107

Figure 4.2 *Schematic diagram of the MDC setup.* 110

Figure 4.3 *Water vapour flux following progressive concentration of concentrated brine solution for different process configurations: (a) without filter device; and (b) with filter device. Inset: evidence for how inclusion of filtration extends residence time in the system. Bulk supersaturation is calculated based on flux mass balance. Conditions: Tbulk 55±1°C; ∆T 20±2°C; initial NaCl concentration, 23.9 Wt.%; feed and permeate velocity, 0.06 m s^{-1}. Standard error of permeation flux was calculated based on differences in triplicate measurements for each membrane modules; (A) 3HF, 3.6±0.4; 7HF, 3.7±0.4; 19HF, 3.5±0.2; 37HF, 2.6±0.1; (B) 3HF, 3.8±0.4; 7HF, 3.4±0.3; 19HF, 3.2±0.2; 37HF, 3.1±0.1.* 116

Figure 4.4 *Turbidity profiles characterising bulk nucleation events for operation: (a) without filter device; and (b) with filter device. Supersaturation at induction is increased by modifying membrane area. Conditions: Tbulk 55±1°C; ∆T 20±2°C; initial NaCl concentration, 23.9 Wt.%; feed and permeate velocity, 0.06 m s^{-1}.* 118

Figure 4.5 *Comparison of induction time between both MDC configurations (with and without in-line filtration) based on turbidity demonstrates that induction is achieved at the same time regardless of whether filtration is employed in the recycle line. Conditions: Tbulk 55±1°C; ∆T 20±2°C; initial NaCl concentration, 23.9 Wt.%; feed and permeate velocity, 0.06 m s^{-1}.* 118

Figure 4.6 *Concentration and temperature polarisation coefficients (CPC and TPC) determined for each module determined when concentrating rate (LnR') is increased by membrane area. Comparison evidences boundary layer characteristics are similar at induction regardless of whether filtration is employed in the recycle line. Conditions: Tbulk 55±1°C; ∆T 20±2°C; initial NaCl concentration, 23.9 Wt.%; feed and permeate velocity, 0.06 m s^{-1}.* 120

Figure 4.7 *The supersaturation achieved at induction is used to construct the metastable zone width (MSZW) using bulk and film concentrations (wt. NaCl/wt., %). Conditions: Tbulk 55±1°C; ∆T 20±2°C; initial NaCl concentration, 23.9 Wt.%; feed and permeate velocity, 0.06 m s^{-1}.* 121

Figure 4.8 *Extent of supersaturation (c/c*) achieved based on the concentrating rate (LnR') imposed by an increase in membrane area; supersaturation attained within bulk and boundary layer (film) are compared. Bulk supersaturation is calculated based on flux mass balance and film concentration is calculated according to CPC values. Conditions: Tbulk 55±1°C; ∆T 20±2°C; initial NaCl concentration, 23.9 Wt.%; feed and permeate velocity, 0.06 m s^{-1}.* 122

Figure 4.9 *The distinction in scaling mechanisms is observed, where the extent of surface adhesion and/or deposition at the membrane surface is dependent on the concentrating rate applied, and the presence of in-line filtration in the recycle line. Increasing concentrating rate (LnR') limits adhesive growth of scalant, while in-line filtration reduces deposition.* 123

Figure 4.10 *Supersaturation profiles that develop before and after the initial primary nucleation event (induction), based on conductivity mass balance for: (a) boundary layer (or film) concentration; and (b) bulk solution concentration. Conditions: Tbulk 55±1°C; ∆T 20±2°C; initial NaCl concentration, 23.9 Wt.%; feed and permeate velocity, 0.06 m s^{-1}.* 125

Figure 4.11 *Supersaturation trajectory during membrane distillation crystallisation, based on different supersaturation rates that are fixed by the membrane area used. In-line filtration is used in each configuration to limit deposition. The theoretical supersaturation profile is calculated based on conductivity mass balance assuming no consumption of NaCl for crystallisation, and compared to actual conductivity data, where the difference evidences where within the metastable zone width that nucleation*

and crystal growth are occurring: (a) 37HF; (b) 19HF; (c)7HF; (d) 3HF. Conditions: Tbulk 55±1°C; ∆T 20±2°C; initial NaCl concentration, 23.9 Wt.%; feed and permeate velocity, 0.06 m s^{-1}. 127

Figure 4.12 *Crystal size distributions (based on volume fraction, %) produced in the absence and presence of filtration to reduce deposition. The key difference is that in-line filtration extends residence time for crystal growth after induction which affects subsequent nucleation, crystal growth and yield. Conditions: Tbulk, 55±1°C; ∆Tmembrane, 20±2°C; initial NaCl concentration, 23.9 wt.%.; feed and permeate velocity, 0.06 m s^{-1}.* 129

Figure 4.13 *Scanning electron microscopy (SEM) of produced crystals at the membrane surface and from the bulk solution: (A) 7HF, with filter device, sampled from membrane (c/c* 1.07, residence time after induction, 89 min); (B) 19HF, with filter device, sampled from membrane (c/c* 1.10, residence time after induction, 33 min); (C) 19HF, sampled from bulk solution in feed vessel, upstream of in-line filter configuration (c/c* 1.04, residence time after induction, 33 min). Distinct crystal growth patterns observed at membrane surface dependent on supersaturating rate, and when crystals are produced in the bulk solution, evidencing the potential to improve crystal morphology.* 132

Figure 4.14 *Indicative illustration for how stage-three flux decline is seemingly dependent upon the system exceeding the supersaturation threshold for primary nucleation. 37 HF configuration used for illustration. Conditions: Tbulk 55±1°C; ∆T 20±2°C; initial NaCl concentration, 23.9 Wt.%; feed and permeate velocity, 0.06 m s^{-1}.* 134

Figure 5.1 *Similar nucleation mechanisms during the transition across MSZW using different supersaturation rate parameters showed distinct scaling behaviour due to different boundary layer characteristics between two approaches.* 147

Figure 5.2 *Crystallisation design across different processes method: (a) batch crystallisation; (b) continuous batch; (c) membrane continuous flow.* 152

List of Figures for Appendices

Figure A 3-1 *Permeation flux for different primary control variable: (A1,A2,A3); based on operating time; (B1,B2,B3); based on bulk supersaturation. Boundary conditions: Tbulk, 55±1°C; Velocity of feed and permeate=0.06 m s^{-1}.* 93

Figure A 3-2 *Turbidity profile during MDC operation based on bulk supersaturation at different primary control variables. (A): 7HF, %wt=23.9, ∆t=20°C; (B): 37HF, %wt=23.9, ∆t=10°C; (C): 37HF, %wt=25.9, ∆t=20°C. Boundary conditions: Tbulk, 55±1°C; Velocity of feed and permeate=0.06 m s^{-1}.* 95

Figure A 4-1 *Population density ln n(no.m^{-4}) versus crystal size (L,μm) plot based on MSMPR model for nucleation rate and crystal growth calculation.* 138

List of Tables

Table 1.1*Summary of advantages and disadvantages of the most common industrial crystallisers.*..... 5

Table 1.2: *Summary of advantages and disadvantages of the different membrane distillation configurations.*..... 11

Table 2.1 *Membrane and module specification.* 32

Table 2.2 *Results analysis of nucleation parameters based on correlation of ln (t_{ind}) versus 1/ln^{2}S.* 50

Table 2.3 *CSD parameters of recovered crystals from different membrane sizes* 54

Table 3.1 *Membrane and module specification.* 70

Table 3.2 Average concentration and temperature polarisation before induction for different supersaturation parameters. 76

Table 3.3 *Analysis of nucleation parameters (based on correlation of ln (tind) versus 1/ln2S according to classical nucleation theory.* 84

Table 4.1 *Membrane and module specification* 109

Table 4.2 *Comparison of crystallisation kinetics at different batch time from 37 HF experiment. Extension in residence time is provided by in-line filtration to reduce deposition.* 129

Table 4.3 *Crystallisation kinetics across different supersaturation profiles developed when using in-line filter configuration.* 131

Table 4.4 *Primary nucleation exceedance (PNT) pattern of different supersaturation profiles* 134

List of Equations

(2-1)..... 34
(2-2)..... 34
(2-3)..... 34
(2-4)..... 34
(2-5)..... 34
(2-6)..... 35
(2-7)..... 35
(2-8)..... 35
(2-9)..... 35
(2-10)..... 35
(2-11)..... 35
(2-12)..... 36
(2-13)..... 36
(2-14)..... 36
(2-15)..... 36
(2-16)..... 36
(2-17)..... 36
(2-18)..... 36
(2-19)..... 37
(2-20)..... 37
(3-1)..... 71
(3-2)..... 72
(3-2)..... 72
(3-3)..... 72
(3-4)..... 72
(3-5)..... 72
(3-6)..... 72
(3-7)..... 72

(3-8)..... 72
(3-9)..... 72
(3-10)..... 72
(3-11)..... 73
(3-12)..... 73
(3-13)..... 73
(3-14)..... 73
(3-15)..... 73
(3-16)..... 73
(3-17)..... 73
(3-18)..... 73
(3-19)..... 74
(3-20)..... 74
(3-21)..... 74
(3-22)..... 74
(3-23)..... 74
(3-24)..... 74
(3-25)..... 74
(3-26)..... 75
(3-27)..... 75
(4-1)..... 111
(4-2)..... 112
(4-3)..... 112
(4-4)..... 112
(4-5)..... 112
(4-6)..... 112
(4-7)..... 112
(4-8)..... 112
(4-9)..... 112

(4-10)..... 113
(4-11)..... 113
(4-12)..... 113
(4-13)..... 113
(4-14)..... 113
(4-15)..... 113
(4-16)..... 113
(4-17)..... 113
(4-18)..... 113
(4-19)..... 114
(4-20)..... 114
(4-21)..... 114
(4-22)..... 114
(4-23)..... 114
(4-24)..... 114

List of Equations for Appendices

(A 2-1) 57
(A 2-2) 57
(A 2-3) 57
(A 2-4) 57
(A 2-5) 57
(A 2-6) 57
(A 2-7) 57
(A 2-8) 57

List of Abbreviations

N	permeate flux, kg m^{-2} h^{-1}
L	hollow fibre length, m
A	effective membrane area, m^2
m	mass of permeate kg
Q	heat transfer, W m^{-2}
Qv	latent heat of evaporation, W m^{-2}
Qc	conductive heat flux through the membrane, W m^{-2}
k_m	membrane thermal conductivity, W m^{-1} K^{-1}
k_p	polymer thermal conductivity, W m^{-1} K^{-1}
k_g	air thermal conductivity, W m^{-1} K^{-1}
k_f	thermal conductivity of feed, W m^{-1} K^{-1}
k_p	thermal conductivity of permeate, W m^{-1} K^{-1}
T_{fm}	feed temperature adjacent to membrane surface, K
T_{pm}	permeate temperature adjacent to membrane surface, K
T_f	bulk temperature in feed, k
T_p	bulk temperature in permeate, k
d_i	outer diameter, mm
d_o	outer diameter, mm
d_{hf}	hydraulic diameter of feed flow channel, m
d_{hp}	hydraulic diameter of permeate flow channel, m
$H_{V,T}$	vapour latent heat, kJ kg^{-1}
h_m	heat transfer coefficient of the membrane, W m^{-2} K^{-1}
h_v	heat transfer coefficient of vapour, W m^{-2} K^{-1}
h_f	film heat transfer coefficients associated of feed side, W m^{-2} K^{-1}
h_p	film heat transfer coefficients associated of permeate side, W m^{-2} K^{-1}
Nu	Nusselt’s number, dimensionless
Re	Reynold’s number, dimensionless
Pr	Prandtl’s number, dimensionless
v	velocity, m s^{-1}
c_p	specific heat of feed/permeate, J kg^{-1} K^{-1}

C_{fm}	interfacial concentration close to the membrane surface, g $_{NaCl}$ g^{-1} $_{solution}$
C_{fb}	feed bulk concentration, g $_{NaCl}$ g^{-1} $_{solution}$
k_s	solute mass transfer coefficient, m s^{-1}
Sh	Sherwood number, dimensionless
Sc	Schmidt number, dimensionless
J	nucleation rate based on CNT, No. m^{-3} s^{-1}
ΔG^*	Gibb's free energy, kJ mol^{-1}
t_{ind}	induction time
k_B	Boltzmann constant, 1.38 x 10^{-23} J K^{-1}
v_o	molecular volume, m^3
M	molar weight, kg mol^{-1}
ρ_{cry}	crystal density, kg m^{-3}
N_a	Avogadro's number (6.022 x 10^{23} molecules mol^{-1})
T	nucleation temperature, K
A	pre-exponential parameter, m^{-3} s^{-1}
B	thermodynamic parameter for nucleation
$\Delta C_{max.fm}$	maximum MSZW at membrane surface, mg g^{-1} solution
R'	concentrating rate, g 100g^{-1} solution h^{-1}
F_p	permeate flow rate, kg h^{-1}
k	nucleation rate constant, No. m^{-3-n} s^{-1+n}
n	nucleation order, dimensionless
n(L)	crystal population density, m^{-4}
n°	population density, m^{-1}
G	growth rate, m s^{-1}
B_o	nucleation rate based on population balance theory, No. m^{-3} s^{-1}

Greek letters

δ_m	membrane thickness, m
ε	membrane porosity, %
ρ	density, kg m^{-3}
μ	viscosity, Pa s^{-1}
γ	interfacial energy, mJ m^{-2}
θ	contact angle, °

1 Introduction

1.1 Crystallisation concepts and applications

Crystallisation is a vital separation method that is widely employed in many chemical manufacturing applications, including fine chemicals, food ingredients and pharmaceuticals products [1,2]. Crystallisation has been acknowledged as a complex process that is governed by two major phases, nucleation and crystal growth [2]. The precise control over these crystallisation phases determines the crystal's purity, morphology, size and size distribution, which have a critical impact on downstream application efficiency [3,4]. Nucleation is the initial phase in the crystallisation which implies the arrangement of solute molecules in a specific pattern to form the initial nuclei of the crystal [5]. The critical size of these nuclei depends on the Gibbs free energy (ΔG^*), which represents the equilibrium between surface-free energy (ΔG_S) and volume-free energy (ΔG_V) [2]. The changes in Gibbs free energy required to overcome the critical barrier energy will determine the likelihood of the transition to the solid phase [17]. The occurrence of nucleation can be classified into two types based on the level of supersaturation achieved: at high supersaturation levels, homogeneous nucleation is dominant, whereas at low supersaturation levels, heterogeneous nucleation becomes more prevalent [6]. At high supersaturation degrees, the system has sufficient energy (ΔG^*_{hom}) to cross the critical barrier energy to form the stable nucleus without the involvement of a foreign substrate [10]. Whereas at lower supersaturation degrees, the foreign substrate or particles can provide the nucleation sites to reduce the energy barrier for heterogeneous nucleation (ΔG^*_{het}) [17]. The growth phase starts when the formed nucleus is thermodynamically stable and larger than the critical size. Once a thermodynamically stable crystal phase is formed, crystal growth can begin to generate visible crystals [7]. Nucleation and crystal growth are driven by the generated supersaturation within the crystalline solution in which supersaturation depends on the mass and heat transfer processes prevailing in the system [8,9]. Supersaturation refers to the difference between the actual concentration of the crystalline solution and the saturation concentration (solubility) [2]. Different methods have been demonstrated to generate supersaturation state, including evaporation, cooling, and anti-solvent addition, among others [2,8]. The rate of supersaturation for each method is regulated to maintain the desired product characteristics and to avoid spontaneous primary nucleation, which is critical for

downstream applications [10,11]. In evaporation crystallisation, supersaturation is created by solvent evaporation from crystallising solutions, in which this method is recognised for bulk chemical production, particularly for those components that show less solubility dependency on temperature (i.e., NaCl) [12]. Cooling crystallisation is usually chosen to recover those components with lower solubility at lower temperatures (i.e. Na_2SO_4) [13]. However, in some cases where the compounds are thermally unstable, an anti-solvent can be used as the driving force for crystallisation, where supersaturation is generated by reducing solute solubility within the saturated solution [14]. Importantly, the target compounds should be insoluble in the anti-solvent liquid, while the solvent should be mixable with the anti-solvent [15].

The region between the maximum supersaturation achieved at nucleation induction and the solubility limit of a solution is termed metastable zone width (MSZW) [16]. According to classical nucleation theory (CNT), the correlation between the induction time and the degree of supersaturation at nucleation induction determines which primary nucleation mechanism will predominate during transposing across MSZW (Figure 1.1) [17].

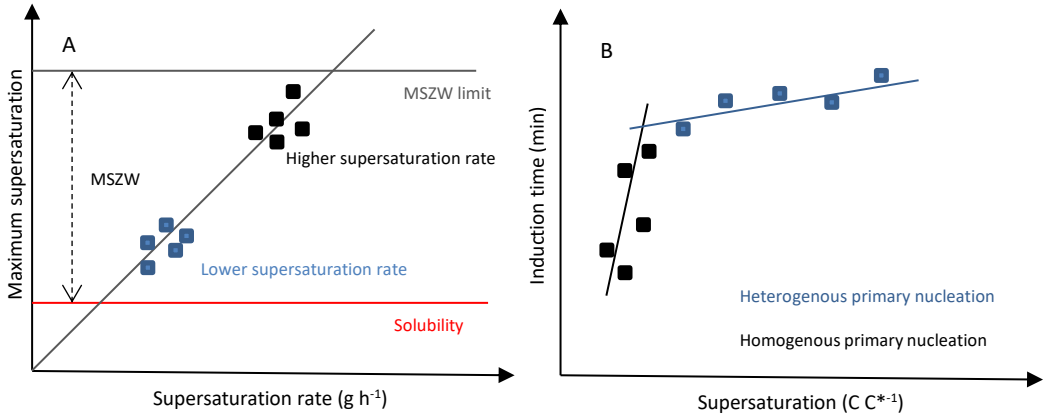

Figure 1.1 *The relationship between induction time and supersaturation at induction during transition across MSZW* **.**

The transition across MSZW can be achieved by adjusting the supersaturation rate, which can be characterised using the approach of Sangwal [18], where a linear relationship between the supersaturation rate and the upper limit of MSZW is implicitly assumed [19]. This relationship describes the nucleation kinetic parameters that govern the crystallisation process [18]. Primary nucleation can occur within various regions of the metastable zone, depending on the supersaturation rate applied [20]. In

general, a high supersaturation rate yields a high nucleation rate where supersaturation reduces the free energy barrier sufficiently for primary nucleation, which favours smaller crystal sizes [10,21]. While the supersaturation driving force for nucleation is lower in the lower area of MSZW, this increases dependency on a heterogeneous host (i.e. crystalliser wall) that can adjust the interfacial energy sufficiently to minimise the Gibbs free energy needed for nucleation where fewer larger crystals can be produced [17,22]. In cooling crystallisation, the faster cooling rate (higher supersaturation rate) results in wider MSZW, as the system seeks nucleation at maximum supersaturation within shortest induction time [23]. Jiang et al. [19] indicated that increasing feed temperature narrows the MSZW because of the increased kinetic energy of molecules, which raises the probability of molecular collisions. This was also observed when the agitation rate was increased, which showed a better diffusive mass transfer mechanism and enhanced molecular interactions [24].

The primary nucleation is typically dominant at the onset of the solid phase forming; however, as the crystallisation progresses, the supersaturation level decreases due to supersaturation consumption by the primary nucleation. Consequently, the supersaturation drops within the metastable zone width (MSZW), where a sufficient population of crystals in the solution promotes the dominance of the secondary nucleation mechanism [5,25]. This occurs as a result of mechanical attrition or fluid shear generated by seed collision with the inner crystalliser wall, stirrer blade or other crystals present in solution, which produces a fragment with a similar crystal structure to the crystal seed [26]. However, Yousuf et al. [27] demonstrated that secondary nucleation could occur without collision, while other studies reveal that it could occur even without attrition of seeds, which results in a polymorphic/chiral crystal structure that differs from the original crystal seed [28,29]. Therefore, the complex nature of secondary nucleation and the different involved mechanisms suggest that it is recommended to prevent or reduce secondary nucleation in industrial crystallisation for further control over the crystal characteristics [5,26]. The direct nucleation control (DNC) strategy has been suggested as a potential solution to minimise secondary nucleation events [30]. Such method enables the system to surpass the metastable boundary and initiate primary nucleation at which the supersaturation level is maintained within a lower saturation threshold (growth only zone) [14]. This can be achieved by controlling the particle number at a predetermined value using feedback

control to regulate the rate of supersaturation, where the system favours the growth phase to reduce the fine crystals and promote a larger final crystal product size [30].

Different types of evaporative and cooling crystallisers are commercially available for the manufacture of fine and bulk chemicals (Table 1.1). The selection of crystalliser depends on several factors, including (i) the composition of the solution undergoing crystallisation and the desired characteristics of the resulting crystals, (ii) the specific requirements for the crystallised product, such as the desired crystal size distribution (CSD) and median size (L_{50}); and (iii) the preferred processing approach, whether it is batchwise, semi-batch, or continuous [31]. Understanding the hydrodynamics, thermodynamics, mass and heat transfer mechanisms, and supersaturation rate is crucial for effectively controlling the nucleation and growth of crystals in crystallisers. This should be combined with precise determination of the MSZW and induction time for designing and controlling the trajectory of crystallisation processes within crystallisers [8].

Table 1.1*Summary of advantages and disadvantages of the most common industrial crystallisers.*

Crystalliser type	Advantages	Disadvantages	References
Stirred draft tube baffle (DTB)	• Suitable for coarse products as the fines can be separated due to the annular settling zone or by dissolving the fines through increased temperature using a heat exchanger. • Narrow the crystal size distribution. • Longer residence times	• Low heat transfer efficiency creates poorly mixed regions which can invoke agglomeration, variable product morphology and size distribution. • Unstable supersaturation profiles in which crystallisation kinetics are hard to control, leading to unexpected particle size distribution	[32,33]
Forced circulation crystalliser (FC)	• Suitable for substances with steady or inverted solubility curves • The least expensive option for large product yield	• Unstable residence time due to flocculated hydrodynamic profiles associated with the incoming solution flow pattern • Broader crystal size distribution is often obtained as a result of a complex interaction between growth and agglomeration	[34,35]
Fluidized bed crystalliser (FBC)	• Large active surface • Stable crystals can be produced due to dominant heterogeneous nucleation. • Fast setting time • Suitable for large products	• High potential of local scaling • Unstable Superficial velocity • Low production rate compared to FC and DTB	[36,37]

However, existing crystallisers have some limitations that impact both final product quality and process efficiency [10]. The design of crystallisers incorporates the heat exchanger independently from the evaporation area, which causes heat dissipation and significant temperature fluctuations within the system, exacerbating the tendency of temperature polarisation [32,33]. This creates a favourable environment at the heat exchanger surface for nucleation and crystal growth (scaling), which leads to modifications in the surface topography and flow patterns in the vicinity of the heat exchanger surface, thereby reducing the heat exchanger's thermal efficiency [31]. This results in an uneven evaporation rate and therefore poor regulation of the supersaturation generation rate (Figure 1.2) [10,38]. Additionally, the limited surface area of heat exchanger leads to a longer induction time to achieve the desired supersaturation level at which nucleation is initiated [39,40]. Furthermore, the complex local and global mixing phenomena caused by the preferential mixing patterns exacerbate poor control over supersaturation, challenging precise control of nucleation kinetics and crystal growth mechanism, resulting in irreproducible final crystal characteristics. [10,33,41]. Currently, there is a lack of well-defined design methodologies and predictive models to effectively address and mitigate these challenges [42]. Meanwhile, the classical scale-up strategies for crystallisers do not consider the geometric and time-dependent variations, leading to ineffective scale-up approaches to meet industrial requirements [43]. Therefore, new technology and crystallisation control strategies by which nucleation and growth mechanisms can be controlled more effectively would be beneficial for affording a potential solution to produce high-value crystalline products and for a more favourable economic return.

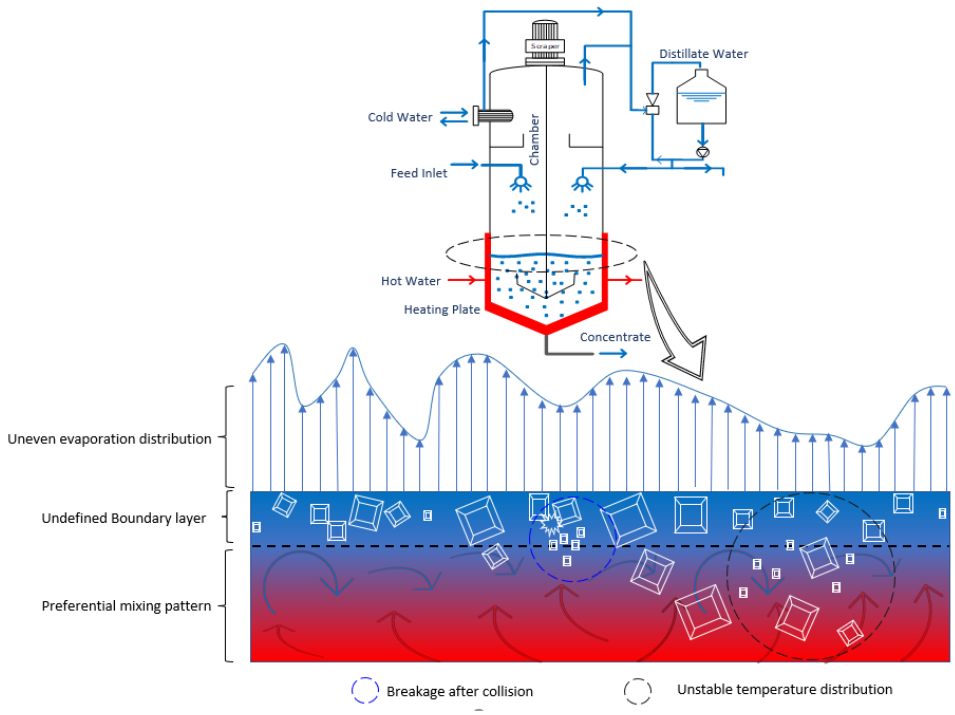

Figure 1.2 *Thermal boundary layer in Conventional crystalliser*

1.2 Membrane distillation crystallisation: Next generation of resource recovery

Membrane distillation crystallisation (MDC) is an emerging and promising technology that combines the principles of membrane distillation and crystallisation to achieve efficient water purification while producing highly valuable chemical products [10,44,45]. MDC employs a hydrophobic membrane to generate a supersaturated phase that can initiate the process of nucleation followed by crystal growth [10,46]. The fixed interfacial area and well-defined boundary layer contribute to consistent heat and mass transfer, which provides a uniform evaporation rate, where well-regulated supersaturation can be achieved to provide well controlled nucleation and crystal growth [47,48]. The higher active surface area to volume ratio in MDC allows for higher distillate recovery under low evaporator temperatures, which is appropriate for the processing of heat-sensitive molecules (protein, enzymes or pharmaceuticals) [44,49]. As a result, MDC provides a higher Gain Output Ratio (GOR), which represents the ratio of recovered distilled water output to the net energy supplied, when compared to classical crystallisers such as evaporation or cooling crystallisers [72]. This is complemented by the lower cost of membrane modules compared to heat exchangers, which makes MDC a more cost-effective and thermally efficient option for crystallisation processes in terms of both capital investment and operating costs.

Different membrane distillation configurations are being used depending on the interaction between feed and permeate sides (Table 1.2) [50]. The choice of DCMD in this study was motivated by the potential for its higher CP/TP values, whose efficiency in such a configuration can be extrapolated to other systems that involve high mass and heat transfer mechanisms. The principal advantage of membrane distillation to existing crystallisation technologies is that the hydrophobic membrane material (high contact angle) promotes heterogeneous nucleation (HEN) at the vicinity of the membrane surface, which reduces the activation energy (energy that must be provided to start a nucleation process), resulting in a short induction time [40,45]. While this can accelerate the crystallisation process, it also poses the challenge of membrane scaling, which reduces the membrane flux and consequently challenges control over the rate of supersaturation [13,51].

Unlike the traditional MD processes used for desalinating seawater or RO retentate with solute concentrations below saturation, MDC systems are designed to treat solutions that are on the threshold of crystallisation or close to saturation for inorganic salts [52]. In MDC systems, the temperature near the membrane surface normally remains lower than the bulk temperature (temperature polarisation) because of direct contact between hot aqueous solutions and colder permeate [21,53]. This is complemented with higher concentration near the membrane surface compared to bulk (concentration polarisation) due to the accumulation of solutes within a boundary layer near the membrane surface as a result of the advective transport of solute towards a nonpermeable boundary and the back-diffusion caused by the concentration gradient [54]. These polarisations not only hinder the driving force for water vapour transport across the membrane, but also promote high film concentration, which advocates nucleation and growth near the membrane surface [21,51]. Consequently, the formation of salt crystals on the membrane surface and within its pores (inorganic scaling), which causes a reduction in the liquid-vapour interface, blocks the diffusion pathway of water vapour and could eventually lead to process failure [55,56].

Many studies have investigated scaling control methods in MDC, but the lack of insight into the kinetic mechanisms associated with the initial nucleation and growth has hindered the development of effective strategies to mitigate and prevent scaling [65]. Furthermore, the drives parameter of scaling mechanism was not fully articulated in the MDC literature, as the obtained results are influenced by specific operating conditions, membrane materials, feed solutions, and experimental setups, leading to

disparities in scaling control recommendations. Some studies have reported that operating at low flow rates increases scaling due to lower turbulence and slower fluid movement, which offer more time to accumulate near the membrane surface (concentration polarisation) [73]. In contrast, some authors observed that increasing the feed flow rate (high shear stress) can lower the probability of membrane scaling by adhesive growth (due to heterogeneous nucleation); however, this does not prevent the deposition of crystals formed within the bulk [54,57]. An analogous pattern was observed by Warsinger et al. [74], who revealed that the scaling mechanism can occur through crystal deposition, specifically via homogeneous primary nucleation, before the crystals are transported and deposited onto the membrane surface. While a higher flow rate or feed velocity can reduce the boundary layer thickness and the solute residence time within the boundary layer, this condition can also enhance the permeate flux and, consequently, the local supersaturation within the membrane boundary layer [65]. This can lead to a misinterpretation of the relevant scaling parameters due to the simultaneous change in permeate flux and boundary layer characteristics. Therefore, a clear demonstration of decoupling surface scaling through either adhesion or deposition is still lacking, despite its significance, as both mechanisms lead to similar effects in reducing flux while being phenomenologically interdependent (Figure 1.3). This can be achieved by an accurate determination of induction time to relate the supersaturation at induction to the kinetics of nucleation and the predominant nucleation mechanism, which has not been elucidated in the existing literature on MDC [54]. Very few MDC studies have reported information on induction times, but the usage of these terms is not always adequate for distinguishing between different nucleation mechanisms [65]. Therefore, a better understanding of induction time within the framework of classical nucleation theory (CNT) after considering the associated concentration and temperature polarisation in the boundary layer is crucial to exploring the underlying nucleation mechanisms for improved scaling mitigation strategies.

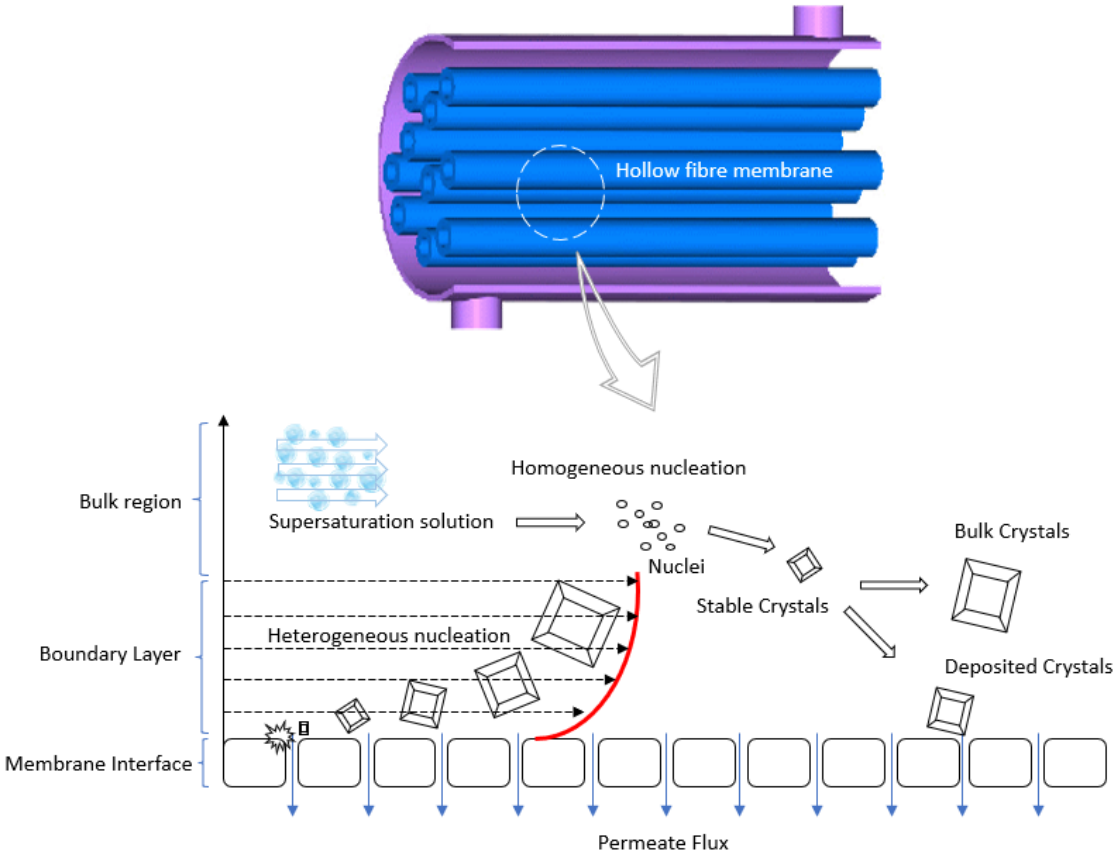

Figure 1.3 *Boundary layer in membrane distillation crystallisation*

Table 1.2: *Summary of advantages and disadvantages of the different membrane distillation configurations.*

Membrane configuration	Advantages	Disadvantages	References
Direct contact membrane distillation (DCMD)	• Straightforward operation and design • High mass transfer	• Lowest energy efficiency • High concentration and temperature polarisation	[13]
Osmotic membrane distillation (OMD)	• High mass transfer • Low energy consumption • Reduced erosion problem	• High concentration polarisation • Membrane wetting • Reverse flux due to concentration polarisation	[58,59]
Sweep gas membrane distillation (SGMD)	• High evaporation efficiency • Low thermal loss	• Not commercially competitive	[60,61]
Air gap membrane distillation (AGMD)	• Low conductive heat loss • Low temperature polarization effect	• Low mass transfer • Large footprint	[13,62–64]
Vacuum membrane distillation (VMD)	• High permeate flux compared • Low operating temperature • Possibility to integrate with renewable energy sources	• Low thermal efficiency • High potential for membrane fouling and performance degradation	[64,65]

1.3 Nucleation and crystal growth control in MDC: including scaling

To date, the rapid decline in membrane flux has been used to indicate the induction time that defines the upper limit of the MSZW [65]. This assumes that once heterogeneous nucleation occurs on the membrane surface, a crystal begins to grow, leading to the blockage of membrane pores and simultaneously causing an irreversible decline in flux. However, this assumption is not accurate since the flux decline and induction time are fundamentally distinct, as there is a lag time between the initial appearance of crystals on either the membrane surface or in the bulk (induction time) and the subsequent irreversible decline in flux [45,54]. Therefore, accurate determination of induction time is crucial in understanding the role of MSZW in controlling the nucleation process. This can relate the induction time to supersaturation, where the predominant nucleation mechanism can be described according to the CNT, which has been rarely reported in the membrane crystallisation literature [50,54].

According to Sangwal [18], the MSZW is linearly related to the supersaturation rate [18]. While MSZW governs the onset of nucleation, it also determines the dependency of nucleation on a heterogeneous host, which is critical to understand the mechanism of scaling. To date, the rate of supersaturation is usually controlled by modifying membrane flux through adjusting the feed temperature or temperature differences (ΔT) [50,65]. Several MDC studies have shown that high feed temperatures narrow the MSZW while also enhancing membrane scaling [50,65,66]. This can be attributed to the higher molecular energy at elevated temperatures, which increases the likelihood of molecular collisions and therefore the effective attachment between crystallisation components [19]. This induces high nucleation at the upper region of MSZW, where the supersaturation is high and homogeneous nucleation is most likely to occur. However, the increased temperature differences typically results in wider MSZW due to higher supersaturation rate associated to higher permeate flux [19]. This informs on higher scaling rate due to higher supersaturation within the boundary layer [51]. Therefore, regardless of metastable size (narrow or wide), the exact mechanism causing scaling, whether adhesive growth (due to heterogeneous nucleation) or crystal deposition (due to homogeneous

nucleation), will not be understood without appropriate induction time measurement techniques. These two mechanisms are distinct but can appear similar in their effects on scaling. According to the CNT, membrane scaling can be minimised by operating at the elevated supersaturation at which nucleation is initiated (higher nucleation rate within the upper region of MSZW), where the process is less dependent on the membrane host to lower the interfacial free energy for nucleation [10]. This contrasts with previous MDC studies, which can be explained by the simultaneous modification of permeate flux by ΔT and the boundary layer characteristics (membrane film concentration and temperature). As a result, the kinetics of nucleation and crystal growth are rather complicated to control due to the simultaneous modification of multiple factors in bulk and membrane boundary layer, which makes recognising the MSZW more challenging while also complicating the associated scaling mechanism. Jiang et al. [19] conducted a rare study that correlated the maximum boundary of the metastable zone width (ΔC_{max}) to supersaturation at which nucleation is initiated by controlling the feed temperature and temperature difference (ΔT) [19]. In their study the nucleation kinetics were not linked to the primary nucleation mechanism (scaling mechanism), or to the following growth phase. According to CNT, operating in the upper region of MSZW is beneficial for promoting homogeneous nucleation. While this condition could minimise scaling by adhesive growth, it will favour smaller crystal sizes with broad size distributions [10,21]. On the other hand, operating in the lower region of the MSZW, where the critical free energy barrier for nucleation approaches its maximum, the membrane is more likely to adjust its interfacial energy to initiate heterogeneous nucleation [13,67]. Despite the increased risk of membrane scaling through adhesive growth in this region, the moderate supersaturation combined over a longer induction time allows for the formation of high-quality crystals with uniform sizes and shapes, leading to a narrower crystal size distribution [10,53]. Therefore, it is crucial to regulate the supersaturation rate to foster a balance between the nucleation kinetics that restrict scaling and the crystal growth conditions that promote desirable product characteristics.

Controlling the final crystal properties, including the morphology, purity, crystal size, and size distribution, is critical to meet the specific requirements of downstream applications [41,68]. Most MDC studies strive to achieve the narrowest CSD with the lowest possible coefficient of variation by modifying different crystallisation parameters such as flow rate, operating time, temperature, or membrane composition [50]. However, such methods are not directly relating the kinetics of crystal growth that are generally associated with the region within the metastable zone where growth was initiated, to the rate of supersaturation applied. Edwie et al. [21] provided one of the very few studies to relate the rate of supersaturation to the final crystal size distribution for NaCl during cooling crystallisation [21]. In their study, crystals formed under a neutral cooling rate exhibited a larger average size when compared to those formed under rapid cooling. This difference was attributed to the enhanced diffusion and growth processes prevailing over nucleation during slower cooling [21,50]. However, it is important to complement this analysis by determining the induction time and the supersaturation at induction to identify the MSZW region and nucleation mechanism under which these crystals are formed.

Supersaturation is well-known to drive the nucleation and crystal growth mechanisms [13,17]. However, the control of supersaturation profile following the onset of primary nucleation induction is not yet investigated in existing MDC literature. Once the initial primary nucleation commenced, the generated concentration of the crystalline solution can yield a large number of small crystals within a relatively short period which increases the potential for scaling through a deposition mechanism (homogeneous mechanism) [54,69]. At this stage, supersaturation is consumed by the initial nucleation event and the supersaturation profile usually drops to a lower position within the MSZW where secondary nucleation and/or growth mechanisms are most likely to occur [30,70]. However, if the rate of supersaturation could not compensate for the progressive nucleation rate, crystallisation will occur outside the metastable zone boundary [30,71]. Hence, strategies for controlling supersaturation (SSC) have been devised to manage the supersaturation profile by manipulating the rate of supersaturation to maintain the supersaturation profile within the desired region

of the MSZW. This approach has a significant impact on enhancing the crystallisation kinetics and subsequent size distribution, quality, and morphology. This is a facet unique to MDC from conventional evaporative crystallisers, where poor control over the generation rate of supersaturation is commonly associated to heat and mass transfer limitations.

1.4 Aim and objectives

This thesis aims to establish strategies to control the mechanisms of nucleation and growth within membrane crystallisation, through development of a kinetic framework founded on the principles of classical nucleation theory that enable the decoupling of primary nucleation phenomena (heterogeneous and homogeneous) and inform on the mechanism of crystal growth. This can be achieved by direct detection of induction time, which underpins a differentiated approach compared to existing MDC literature in which accurate characterization of the two discrete saturation regions (bulk and membrane film) informs the crystallisation process. To address this aim, individual objectives have been developed:

(i) Regulate the supersaturation rate to investigate different regions within the metastable zone without modifying the interfacial boundary layer characteristics, as a method to selectively control the primary nucleation mechanisms that govern both the extent of scaling and bulk crystallisation.

(ii) Characterise strategies that set supersaturation rate through creation of a kinetic framework grounded in classical nucleation theory to provide a deterministic approach to forecasting nucleation and crystal growth in MDC.

(iii) Demonstrate supersaturation control strategies that can promote sustained and controllable kinetic trajectories following nucleation induction to enable advanced controlled crystal growth phase.

1.5 Thesis structure

This thesis is divided into six chapters; Chapter 1 discusses the crystallisation principles and applications, including both classical industrial crystallisers and membrane distillation crystallisation. Chapters 2, 3, and 4 are formatted as journal

papers for submission to peer review, and correspond to the intent of the developed thesis objectives (Figure 1.4). Chapter 2, "*Modifying supersaturation rate with membrane area to volume ratio: scaling reduction and improved crystal growth control in membrane distillation crystallisation*", explores the mechanisms of crystallisation and scaling across different regions within the metastable zone to enhance strategies for reducing scaling and promoting bulk crystal growth. Chapter 3, "*Methods to modify supersaturation rate in membrane distillation crystallisation: control of nucleation and crystal growth kinetics (including scaling)*", provides a kinetic framework from multiple supersaturation parameters that independently control nucleation and crystal growth where a broad range of kinetic trajectories can be delivered for the effective mitigation of scaling and better crystal growth. Chapter 4, "*Facile supersaturation control strategies for membrane distillation crystallisation*", evidence that a consistent supersaturation gradient following nucleation can be sustained to foster subsequent nucleation events and crystal growth within specific regions of the metastable zone for improved crystallisation trajectory and final crystals properties. Chapter 5 provides an overall discussion of the thesis to synthesise outcomes into their practical significance, while Chapter 6 includes conclusions and further work.

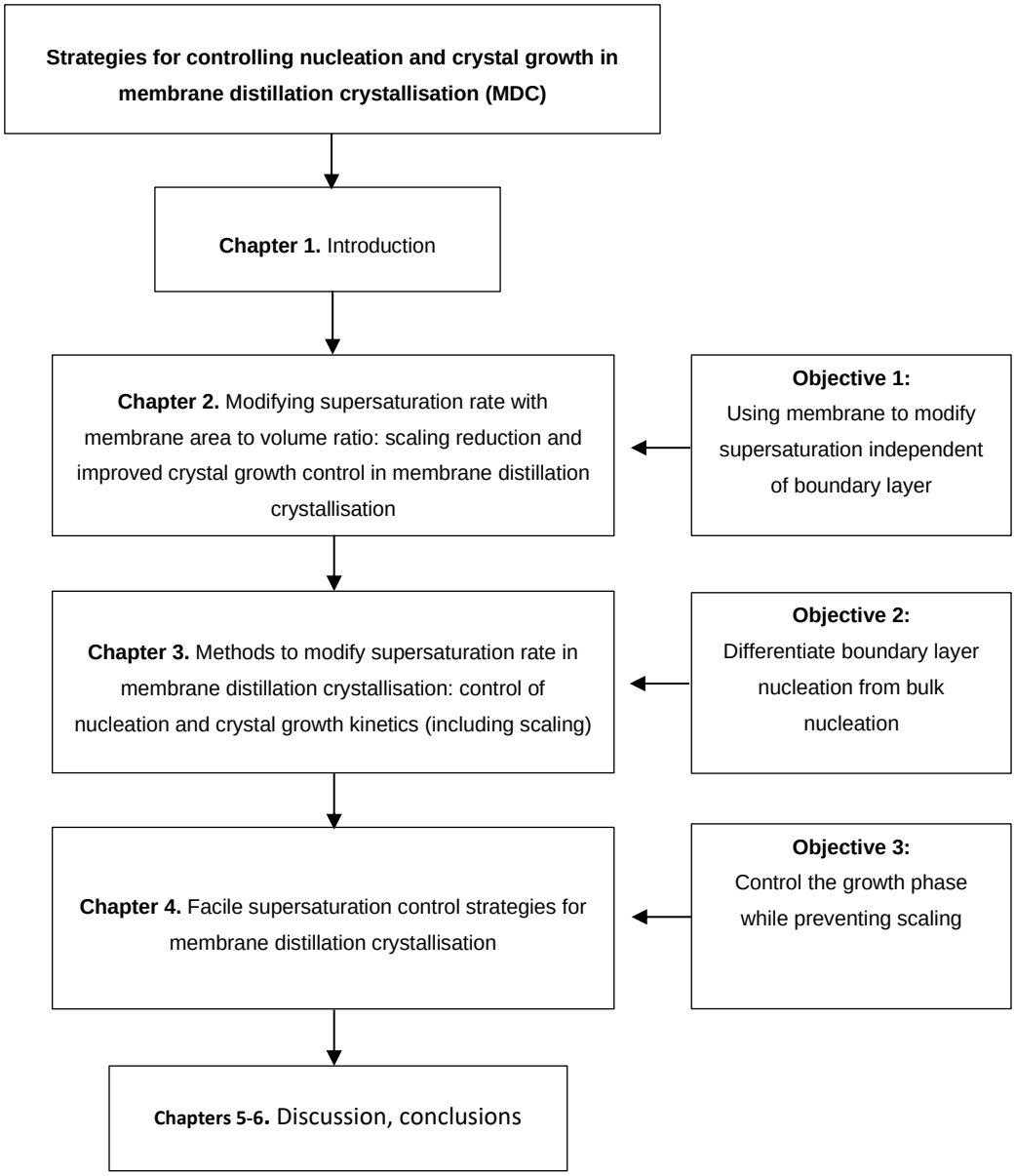

Figure 1.4 *Thesis structure*

1.6 References

[1] F. Zou, W. Zhuang, J. Wu, J. Zhou, P.P. Yang and Q. Liu, Y. Chen, H. Ying, Determination of metastable zone widths and the primary nucleation and growth mechanisms for the crystallization of disodium guanosine 5′-monophosphate from a water-ethanol system, Ind. Eng. Chem. Res. 54 (2015) 137–145.

[2] M. Lenka and D. Sarkar, Determination of metastable zone width, induction period and primary nucleation kinetics for cooling crystallization of L-asparaginenohydrate, J. Cryst. Growth. 408 (2014) 85–90.

[3] Z.K. Nagy and E. Aamir, Systematic design of supersaturation controlled crystallization processes for shaping the crystal size distribution using an analytical estimator, Chem. Eng. Sci. 84 (2012) 656–670.

[4] I. Ostergaard, B. Szilagyi, H.L. De Diego, H. Qu and Z.K. Nagy, Polymorphic Control and Scale-Up Strategy for Antisolvent Crystallization Using Direct Nucleation Control, Cryst. Growth Des. 20 (2020) 2683–2697.

[5] S.G. Agrawal and A.H.J. Paterson, Secondary Nucleation: Mechanisms and Models, Chem. Eng. Commun. 202 (2015) 698–706.

[6] F. Liendo, M. Arduino, F.A. Deorsola and S. Bensaid, Nucleation and growth kinetics of CaCO 3 crystals in the presence of foreign monovalent ions, J. Cryst. Growth. 578 (2022) 126406.

[7] J.W. Mullin, Crystal growth, in: J.W. Mullin (Ed.), Cryst. (Fourth Ed., Fourth Edi, Butterworth-Heinemann, Oxford, (2001) 216–288.

[8] L. Nemdili, O. Koutchoukali, F. Mameri, I. Gouaou, M.S. Koutchoukali and J. Ulrich, Crystallization study of potassium sulfate-water system, metastable zone width and induction time measurements using ultrasonic, turbidity and 3D-ORM techniques, J. Cryst. Growth. 500 (2018) 44–51.

[9] A.S. Myerson, D. Erdemir and A.Y. Lee, Handbook of Industrial Crystallization, Third Edit, Cambridge University Press, (2019) 15–39 .

[10] G. Di Profio, E. Curcio and E. Drioli, Supersaturation control and heterogeneous nucleation in membrane crystallizers: Facts and perspectives, Ind. Eng. Chem. Res. 49 (2010) 11878–11889.

[11] L. Zhou, Z. Wang, M. Zhang, M. Guo, S. Xu and Q. Yin, Determination of

metastable zone and induction time of analgin for cooling crystallization, Chinese J. Chem. Eng. 25 (2017) 313–318.

[12] H. Lu, J. Wang, T. Wang, N. Wang, Y. Bao and H. Hao, Crystallization techniques in wastewater treatment: An overview of applications, Chemosphere. 173 (2017) 474–484.

[13] Y. Choi, G. Naidu, L.D. Nghiem, S. Lee and S. Vigneswaran, Membrane distillation crystallization for brine mining and zero liquid discharge: Opportunities, challenges, and recent progress, Environ. Sci. Water Res. Technol. 5 (2019) 1202–1221.

[14] D. Duffy, M. Barrett and B. Glennon, Novel, calibration-free strategies for supersaturation control in antisolvent crystallization processes, Cryst. Growth Des. 13 (2013) 3321–3332.

[15] M. Torkian, M. Manteghian and M. Safari, Caffeine metastable zone width and induction time in anti-solvent crystallization, J. Cryst. Growth. 594 (2022) 126790.

[16] S. Karthika, T.K. Radhakrishnan and P. Kalaichelvi, Measurement of nucleation rate of ibuprofen in ionic liquid using induction time method, J. Cryst. Growth. 521 (2019) 55–59.

[17] G. Di Profio, S. Tucci, E. Curcio and E. Drioli, Controlling polymorphism with membrane-based crystallizers: Application to form i and II of paracetamol, Chem. Mater. 19 (2007) 2386–2388.

[18] K. Sangwal, On the interpretation of metastable zone width in anti-solvent crystallization, Cryst. Res. Technol. 45 (2010) 909–919.

[19] X. Jiang, X. Ruan, W. Xiao, D. Lu and G. He, A novel membrane distillation response technology for nucleation detection, metastable zone width measurement and analysis, Chem. Eng. Sci. 134 (2015) 671–680.

[20] R.A. Bueno, D. Version, Crystallization of Active Pharmaceutical Ingredients in the Presence of Heterosurfaces, (2022).

[21] F. Edwie and T.S. Chung, Development of simultaneous membrane distillation-crystallization (SMDC) technology for treatment of saturated brine, Chem. Eng. Sci. 98 (2013) 160–172.

[22] E. Curcio, E. Fontananova, G. Di Profio and E. Drioli, Influence of the

structural properties of poly(vinylidene fluoride) membranes on the heterogeneous nucleation rate of protein crystals, J. Phys. Chem. B. 110 (2006) 12438–12445.

[23] X. Ni and A. Liao, Effects of cooling rate and solution concentration on solution crystallization of L-glutamic acid in an oscillatory baffled crystallizer, Cryst. Growth Des. 8 (2008) 2875–2881.

[24] G. Zeng, H. Li, S. Huang, X. Wang and J. Chen, Determination of metastable zone width and the primary nucleation kinetics of sodium sulfate, Theor. Found. Chem. Eng. 49 (2015) 869–876.

[25] N. Kubota, A unified interpretation of metastable zone widths and induction times measured for seeded solutions, J. Cryst. Growth. 312 (2010) 548–554.

[26] M.L. Briuglia, J. Sefcik and J.H.T. Horst, Measuring Secondary Nucleation through Single Crystal Seeding, Cryst. Growth Des. 19 (2019) 421–429.

[27] M. Yousuf and P.J. Frawley, Quantitative Link between Secondary Nucleation and Mixing Hydrodynamics in Batch Cooling Crystallization: A New Approach in Process Development, Org. Process Res. Dev. 23 (2019) 2009–2019.

[28] L. Bosetti, B. Ahn and M. Mazzotti, Secondary Nucleation by Interparticle Energies. I. Thermodynamics, Cryst. Growth Des. 22 (2022) 87–97.

[29] R.Y. Qian and G.D. Botsaris, A new mechanism for nuclei formation in suspension crystallizers: The role of interparticle forces, Chem. Eng. Sci. 52 (1997) 3429–3440.

[30] Y. Gao, T. Zhang, Y. Ma, F. Xue, Z. Gao, B. Hou and J. Gong, Application of pat-based feedback control approaches in pharmaceutical crystallization, Crystals. 11 (2021) 1–27.

[31] G.M. Westhoff, H.J.M. Kramer, P.J. Jansens and J. Grievink, Design of a Multi-Functional Crystallizer for Research Purposes, Chem. Eng. Res. Des. 82 (2004) 865–880.

[32] M. Schmalenberg, L. Mensing, S. Lindemann, T. Krell and N. Kockmann, Miniaturized draft tube baffle crystallizer for continuous cooling crystallization, Chem. Eng. Res. Des. 178 (2022) 232–250.

[33] E. Kougoulos, A.G. Jones and M.W. Wood-Kaczmar, Process modelling tools for continuous and batch organic crystallization processes including application to scale-up, Org. Process Res. Dev. 10 (2006) 739–750.

[34] J. Darand, A. Jafarian and S. Tizbin, A hybrid compartmental-CFD model to investigate forced circulation crystallizer performance, Desalination. 533 (2022) 115743.

[35] S. Tizbin, A. Jafarian and J. Darand, Numerical investigation of hydrodynamics and crystal growth in a forced circulation crystallizer, Desalination. 496 (2020) 114739.

[36] T.-H. Ha, N.N.N. Mahasti, M.-C. Lu and Y.-H. Huang, Application of low-solubility dolomite as seed material for phosphorus recovery from synthetic wastewater using fluidized-bed crystallization (FBC) technology, Purif. Technol. 303 (2022) 122192.

[37] T. Ha, N.N.N. Mahasti, C. Lin, M. Lu and Y. Huang, Journal of Water Process Engineering Enhanced struvite (MgNH 4 PO 4 · 6H 2 O) granulation and separation from synthetic wastewater using fluidized-bed crystallization (FBC) technology, J. Water Process Eng. 53 (2023) 103855.

[38] S.K. Jha, S. Karthikaa and T.K. Radhakrishnan, Modelling and control of crystallization process, Resour. Technol. 3 (2017) 94–100.

[39] J. Ulrich and P. Frohberg, Problems, potentials and future of industrial crystallization, Front. Chem. Sci. Eng. 7 (2013) 1–8.

[40] S. Meng, Y. Ye, J. Mansouri and V. Chen, Crystallization behavior of salts during membrane distillation with hydrophobic and superhydrophobic capillary membranes, J. Memb. Sci. (2015) 165–176.

[41] A. Jones, S. Rigopoulos and R. Zauner, Crystallization and precipitation engineering, Comput. Chem. Eng. 29 (2005) 1159–1166.

[42] S.K. Bermingham, P.J.T. Verheijen and H.J.M. Kramer, Optimal design of solution crystallization processes with rigorous models, Chem. Eng. Res. Des. 81 (2003) 893–903.

[43] H.J.M. Kramer, S.K. Bermingham and G.M. Van Rosmalen, Design of industrial crystallisers for a given product quality, J. Cryst. Growth. 198–

199 (1999) 729–737.

[44] A. Ali, C.A. Quist-Jensen, F. Macedonio and E. Drioli, Application of membrane crystallization for minerals' recovery from produced water, Membranes (Basel). 5 (2015) 772–792.

[45] I. Ruiz Salmón and P. Luis, Membrane crystallization via membrane distillation, Chem. Eng. Process. Process Intensif. 123 (2018) 258–271.

[46] R. Creusen, J. van Medevoort, M. Roelands, A. van Renesse van Duivenbode, J.H. Hanemaaijer and R. van Leerdam, Integrated membrane distillation-crystallization: Process design and cost estimations for seawater treatment and fluxes of single salt solutions, Desalination. 323 (2013) 8–16.

[47] A. Caridi, G. Di Profio, R. Caliandro, A. Guagliardi, E. Curcio and E. Drioli, Selecting the desired solid form by membrane crystallizers: Crystals or cocrystals, Cryst. Growth Des. 12 (2012) 4349–4356.

[48] E. Chabanon, D. Mangin and C. Charcosset, Membranes and crystallization processes: State of the art and prospects, J. Memb. Sci. 509 (2016) 57–67.

[49] A.G. Asimakopoulou and A.J. Karabelas, A study of mass transfer in hollow-fiber membrane contactors-The effect of fiber packing fraction, J. Memb. Sci. 282 (2006) 430–441.

[50] M.C. Sparenberg, S. Chergaoui, V. Sang Sefidi and P. Luis, Crystallization control via membrane distillation-crystallization: A review, Desalination. 519 (2022) 115315.

[51] M.T. Chan, A.G. Fane, J.T. Matheickal and R. Sheikholeslami, Membrane distillation crystallization of concentrated salts - Flux and crystal formation, J. Memb. Sci. 257 (2005) 144–155.

[52] F. Edwie and T.S. Chung, Development of hollow fiber membranes for water and salt recovery from highly concentrated brine via direct contact membrane distillation and crystallization, J. Memb. Sci. (2012).

[53] G. Chen, Y. Lu, X. Yang, R. Wang and A.G. Fane, Quantitative study on crystallization-induced scaling in high-concentration direct-contact membrane distillation, Ind. Eng. Chem. Res. 53 (2014) 15656–15666.

[54] T. Horseman, Y. Yin, K.S. Christie, Z. Wang, T. Tong and S. Lin, Wetting, Scaling, and Fouling in Membrane Distillation: State-of-the-Art Insights on Fundamental Mechanisms and Mitigation Strategies, ACS ES&T Eng. 1 (2021) 117–140.

[55] Y. Yun, R. Ma, W. Zhang, A.G. Fane and J. Li, Direct contact membrane distillation mechanism for high concentration NaCl solutions, Desalination. 188 (2006) 251–262.

[56] M. Gryta, Fouling in direct contact membrane distillation process, J. Memb. Sci. 325 (2008) 383–394.

[57] G. Naidu and S. Jeong, S. Vigneswaran, Influence of feed/permeate velocity on scaling development in a direct contact membrane distillation, Sep. Purif. Technol. 125 (2014) 291–300.

[58] I. Ruiz Salmón, R. Janssens and P. Luis, Mass and heat transfer study in osmotic membrane distillation-crystallization for CO2valorization as sodium carbonate, Sep. Purif. Technol. 176 (2017) 173–183.

[59] M.G. Alvarez, V.S. Sefidi, M. Beguin, A. Collet, R.B. Soria and P. Luis, Osmotic Membrane Distillation Crystallization of NaHCO3, Energies. 15 (2022) 2682.

[60] S.E. Moore, S.D. Mirchandani, V. Karanikola, T.M. Nenoff, R.G. Arnold and A. Eduardo Sáez, Process modeling for economic optimization of a solar driven sweeping gas membrane distillation desalination system, Desalination. 437 (2018) 108–120.

[61] I.A. Said, T. Chomiak, J. Floyd and Q. Li, Sweeping gas membrane distillation (SGMD) for wastewater treatment, concentration, and desalination: A comprehensive review, Chem. Eng. Process. - Process Intensif. 153 (2020) 107960.

[62] N. Thomas, J. Swaminathan, G. Zaragoza, R.K. Abu Al-Rub, J.H. Lienhard V and H.A. Arafat, Comparative assessment of the effects of 3D printed feed spacers on process performance in MD systems, Desalination. 503 (2021) 114940.

[63] Z. Zhang, A.A. Atia, J.A. Andrés-Mañas, G. Zaragoza and V. Fthenakis, Comparative techno-economic assessment of osmotically-assisted

reverse osmosis and batch-operated vacuum-air-gap membrane distillation for high-salinity water desalination, Desalination. 532 (2022) 115737.

[64] M.A.E.R. Abu-Zeid, Y. Zhang, H. Dong, L. Zhang, H.L. Chen and L. Hou, A comprehensive review of vacuum membrane distillation technique, Desalination. 356 (2015) 1–14.

[65] X. Jiang, L. Tuo, D. Lu, B. Hou, W. Chen and G. He, Progress in membrane distillation crystallization: Process models, crystallization control and innovative applications, Front. Chem. Sci. Eng. 11 (2017) 647–662.

[66] A. Bauer, M. Wagner, H. Horn and F. Saravia, Operation conditions affecting scale formation in membrane distillation - An in situ scale study based on optical coherence tomography, J. Memb. Sci. 623 (2021).

[67] X. Jiang, Y. Shao, L. Sheng, P. Li and G. He, Membrane Crystallization for Process Intensification and Control: A Review, Engineering. 7 (2021) 50–62.

[68] E. Drioli, G. Di Profio and E. Curcio, Progress in membrane crystallization, Curr. Opin. Chem. Eng. 1 (2012) 178–182.

[69] G. Chen, Y. Lu, W.B. Krantz, R. Wang and A.G. Fane, Optimization of operating conditions for a continuous membrane distillation crystallization process with zero salty water discharge, J. Memb. Sci. 450 (2014) 1–11.

[70] H. Takiyama, Supersaturation operation for quality control of crystalline particles in solution crystallization, Adv. Powder Technol. 23 (2012) 273–278.

[71] X. Jiang, Y. Niu, S. Du and G. He, Membrane crystallization: Engineering the crystallization via microscale interfacial technology, Chem. Eng. Res. Des. 178 (2022) 454–465.

[72] P. Sharan, T.J.Toon, H. Thakkar, R. P. Currier, R. Singh and A.T. Findikoglu, Optimal design of multi-stage vacuum membrane distillation and integration with supercritical water desalination for improved zero liquid discharge desalination, J. Clean. Prod. 361 (2022) 132189.

[73] Y. Shin and J. Sohn, “Mechanisms for scale formation in simultaneous membrane distillation crystallization: Effect of flow rate,” J. Ind. Eng. Chem. 35 (2016) 318–324.

[74] D.M. Warsinger, E.W. Tow, J. Swaminathan and J.H.L. V, Theoretical framework for predicting inorganic fouling in membrane distillation and experimental validation with calcium sulfate, J. Memb. Sci. 528 (2017) 381–390.

2 Modifying supersaturation rate with membrane area to volume ratio: scaling reduction and improved crystal growth control in membrane distillation crystallisation

Modifying supersaturation rate with membrane area to volume ratio: scaling reduction and improved crystal growth control in membrane distillation crystallisation

A. Ouda, Y. Bajón Fernández, E. McAdam

Cranfield Water Science Institute, Cranfield University, UK

Corresponding author: e.mcadam@cranfield.ac.uk

Abstract

This study provides detailed characterisation of nucleation kinetics, induction time and supersaturation to understand scaling and crystal growth in membrane distillation crystallisation. Membrane area was used to moderate supersaturation rate, as a method to transition across the metastable zone without modifying boundary layer condition. Increasing membrane area sustained the same water vapour flux but increased supersaturation rate within the crystallising solution (sodium chloride). This reduced induction time and increased the supersaturation level at induction. Membrane scaling was minimised by increasing supersaturation rate despite an increase in nucleation rate. This conforms with classical nucleation theory (CNT) while contradicting membrane distillation crystallisation literature, where elevated supersaturation is often linked to advanced scaling. The study evidenced the transition from heterogeneous to homogeneous nucleation once greater supersaturation at induction was achieved. The probability for scaling within the low supersaturation domain was confirmed through diagnostic investigation of the scaling deposit formed, and the growth mechanism within the scaling layer related to the relevant supersaturation region. Crystal size and morphology were also related to the metastable region, where membrane-to-volume ratio can facilitate higher nucleation rates complemented by greater crystal growth. This study provides critical insight for the development of scaling mitigation strategies and creates a basis for the sustainable design of thermal membrane crystallisation systems.

Keywords: *scaling mitigation; zero liquid discharge; brine; direct contact; hollow fibre; NaCl*

2.1 Introduction

Membrane distillation crystallisation (MDC) is a promising technology for resource recovery and the production of high value crystalline products, which can be applied to hypersaline fluids thus affording a potential solution for zero liquid discharge [1,2]. A critical limit to conventional crystallisers is the advent of preferential mixing patterns, which invoke complex local and global mixing phenomenon [3]. This results in poor regulation of supersaturation, which is a critical factor in controlling nucleation and crystal growth [4,5]. The hydrophobic microporous membrane in MDC introduces fixed interfacial area, to deliver fine control over heat and mass transfer mechanisms that yield a uniform evaporation rate, resulting in consistent regulation of supersaturation [6]. This can ensure a final crystal product comprising a fixed size, and narrow size distribution which is of significant value to many prospective end-uses [7–9].

Membrane properties (e.g. polar/non-polar components) have also been acknowledged for their role in adjusting the effective surface free energy (ΔG_s), as this lowers the energy barrier for nucleation through improving solute-membrane interaction [7,10]. Consequently, the hydrophobic membrane can promote heterogeneous nucleation (HEN) through reducing the activation energy (ΔG) to shorten induction time [7]. While this presents a unique advantage to MDC, it also poses a challenge due to the risk of membrane scaling, which reduces control over supersaturation due to the reduction in flux, and could eventually lead to process failure [11–13]. The explicit contribution of the membrane to scaling is not clear but may relate to the solute-membrane interaction extending solute hold-up, or improvement in molecular orientation [7]. It has also been proposed that material morphology can effect scaling as cavity structure [14], roughness and pore structure [13] could lead to solute entrapment, introducing local regions of supersaturation. This may be exacerbated by concentration and temperature polarisation which can alter the concentration, solubility and fluid physics within the primarily laminar boundary layer [15]. Several authors have suggested that with sufficient shear stress, the probability for membrane scaling can be limited by enabling the back transport of crystals from the membrane to the bulk [7,16]. However, this implies that the applied shear stress is sufficient to overcome forces initiated by the solute-membrane interaction, and that the formation of scale and crystal phase (that is recoverable from

the bulk solution) are phenomenologically interdependent which has yet to be clearly demonstrated.

One of the critical challenges in improving understanding of membrane scaling and membrane crystallisation is the accurate determination of induction time, as this can relate supersaturation to the kinetics of nucleation and crystal growth [17]. Sangwal (2010) describes how the maximum supersaturation that can be achieved at induction ($\Delta C_{max,fm}$) is dependent upon the supersaturation rate. This supersaturation limit is termed the metastable zone width (MSZW) (Figure 2.1) [18,19].

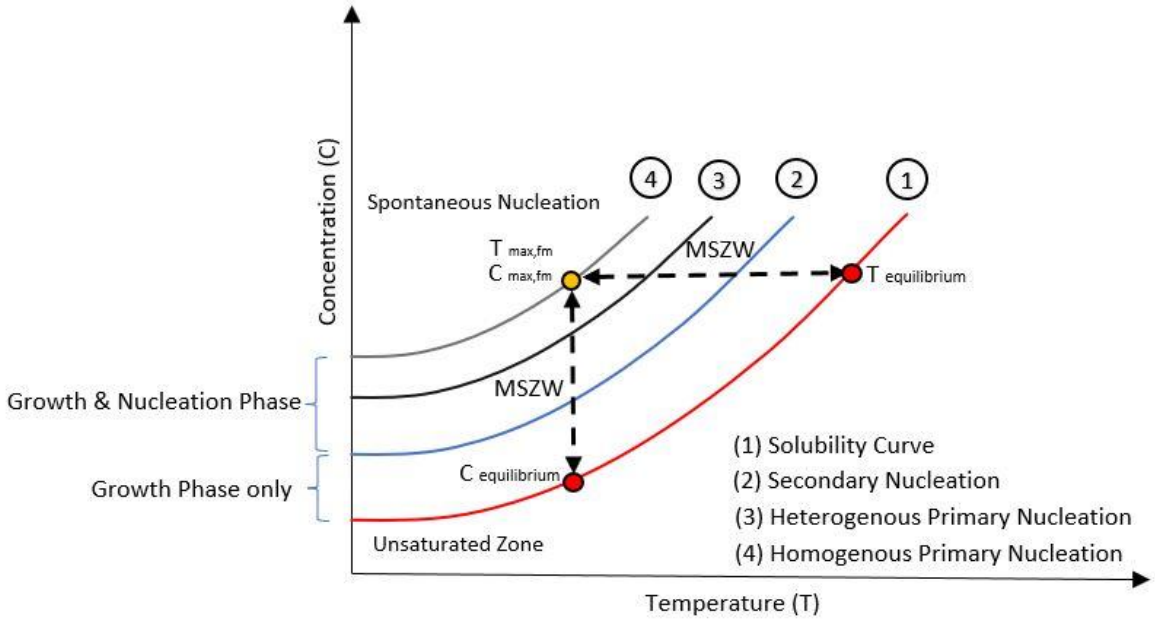

Figure 2.1 *MSZW as function of temperature and concentration.*

Crystallisation at the outer region of the metastable zone is best avoided, as this can introduce high nucleation rates, generating a fine crystal product that is difficult to separate and is of limited value for downstream application [7,20]. In MCr, the supersaturation rate is modified by the membrane flux. Jiang et al. [8] showed how supersaturation rate could be adjusted by changing the feed temperature and the temperature difference between feed and permeate. High feed temperature and temperature difference reduce the critical free energy barrier for nucleation and should favour homogeneous nucleation [13,19]. According to classical nucleation theory, if scaling is to be minimised, supersaturation conditions approaching the solubility limit should also be avoided as it is within this lower region of the metastable zone that the

critical free energy barrier for nucleation approaches a maximum (leading to long induction times). Consequently, it is within this region that the membrane is most likely to adjust interfacial energy sufficiently to initiate heterogeneous nucleation (or scaling) [17,21,22]. Therefore, to achieve a crystalline product specification based on size, size distribution and purity, while avoiding scaling, supersaturation should be regulated to a setpoint somewhere between the solubility limit and the outer limit of the metastable zone, which requires modulation of the supersaturation rate.

While homogeneous primary nucleation should be favoured by elevated supersaturation due to the reduction in critical free energy for nucleation (which reduces dependency on the membrane to lower the interfacial free energy requirement), various authors have shown that high feed temperatures enhanced membrane scaling (heterogeneous primary nucleation mechanism) [15,23]. This contradiction may arise from the adoption of high water vapour fluxes which increase interfacial concentration within the boundary layer through simultaneously modifying flux, solute concentration and temperature polarisation. Consequently, there is a higher probability for nucleation to preferentially occur within the interfacial region, that may proceed through an adhesive growth mechanism (often described as heterogeneous nucleation) or through the deposition of crystals that have undergone nucleation in the bulk solution (homogeneous nucleation) [13,24]. To date, the supersaturation rate in MDC, which determines where within the metastable zone that nucleation will commence, has almost exclusively been studied through changes to feed temperature and temperature difference which modify membrane flux [15,23,25]. According to Nývlt [26], the supersaturation rate is independent of membrane flux and is instead dependent on the supersaturation rate of the crystallising solution [8,26,27]. The rate of supersaturation (R) can therefore be modified without changes to feed temperature or temperature difference by an increase in membrane surface area. This permits transition across the MSZW, without modifying conditions within the boundary layer to yield a broader set of kinetic trajectories for nucleation and crystal growth, that may also reduce the probability for scaling when approaching the upper region of the metastable zone where homogeneous primary nucleation is more likely to occur [7].

In this study, we therefore propose to modify supersaturation rate using membrane area to enable the regulation of supersaturation across the MSZW. Through adjusting

supersaturation independent of temperature or temperature difference, we will examine the potential to decouple surface scaling from bulk nucleation. This will be complemented by the use of in-line dual optic fibre turbidimetry, for the accurate determination of induction time, which can be used to describe the nucleation kinetics within MDC. As this technique provides direct detection of the first crystals formed in the system, it is also possible to differentiate between the effects of adhesive scaling from those of deposition. Consequently, the mechanisms of scaling and crystallisation can be explored, and the modulation of crystallisation examined across the metastable zone to better inform on strategies to diminish scaling and favour homogeneous (or bulk) nucleation to advance control over crystal growth. Specific objectives are to: (i) characterise the MSZW through adjusting supersaturation rate by membrane area; (ii) relate supersaturation and induction time to MDC using classical nucleation theory; (iii) inform on the relative importance of heterogeneous and homogeneous nucleation during the transition across the metastable zone; and (iv) describe how regulating supersaturation rate within the metastable zone can modify properties of the crystal product.

2.2 Materials and methods

2.2.1 Laboratory set-up for membrane distillation crystallisation experiments

Commercial polypropylene hollow fibres (Accural PP 300/1200, from 3M Company, Germany) were potted into end plates using epoxy (Araldite). The membrane comprised a pore size of 0.45µm, wall thickness of 300µm and porosity of 73% (Table 2.1). Distribution of the fibres was controlled by spatial arrangement of predrilled holes in the end plates, which ensured a consistent separation distance between fibres for each module studied. Once the hollow fibres were sealed into the end plates, the membrane was mounted into an acrylic membrane module with a 15 mm internal diameter and 150 mm effective length. Membrane modules comprised of 1, 3, 7, 19, 25, and 37 hollow fibres.

Table 2.1 *Membrane and module specification.*

Property	Units	Value	Fibre no.					
			1	3	7	19	25	37
Internal diameter	$(\mathrm{di}, \mathrm{m})$	0.0012						
Outer diameter	$(\mathrm{do}, \mathrm{m})$	0.0018						
Wall thickness	(m)	0.0003						
d_i/d_o	-	0.67						
Pore size	$(\mu\mathrm{m})$	0.45						
Porosity	(%)	73±2						
Contact angle[a]	(°)	131						
Fibre length	(m)	0.15						
Shell inner diameter	(m)	0.015						
Packing density	(%)		1.5	4.4	10.2	27.7	36.4	53.9
Membrane area	(cm^2)		8.5	25.5	59.4	161.2	212.1	313.9

[a] Measured using water [29]

Membrane distillation was operated in direct contact mode. The feed was recirculated in the shell-side, and the cold solution recirculated in the lumen-side of the hollow fibre membrane (Figure 2.2). Feed concentration was fixed at 23.9 wt.% sodium chloride (NaCl) for each condition studied. This concentration is sufficiently below the supersaturation threshold to ensure the experiments reach steady-state prior to achieving a supersaturation of 1, as this ensures the precise discrimination of induction time. The feed solution was heated to 55±1°C using a heater and heat exchange assembly (Tornado TM IS6, HUBER Ministat230; Radleys, Saffron Walden, UK). Deionised water was used within the cold-side, and was cooled with a chiller (LT ECOCOOL 150, Grant Instruments, Shepreth, UK). The feed and permeate were recycled by a peristaltic pump (Masterflex L/S Digital Pump System, Cole Parmer, St. Neots, UK) to fix velocity at 0.06 m s^{-1}. Increasing fibre number reduced shell-side priming volume, and so the flow rate was adjusted to maintain a velocity of 0.06 m s^{-1}. By maintaining a comparable liquid velocity (and adjusting the heat input), a

comparable temperature difference (ΔT) of 20±2°C was set for each module tested. The only exception was the 1 hollow-fibre module, which necessitated a feed velocity of ~0.6 m s^{-1} to maintain the same ΔT. While a constant liquid velocity was maintained for each module, the Reynold's number declined with an increase in hollow fibre number due to the reduction in cross sectional area. However, laminar flow conditions were consistently established within each membrane module tested (*Re* 134 to 1370, for 37 and 1 HF respectively). Temperature and conductivity were measured in-line (El1034 Temperature Prop, LabJack Corporation, Lakewood, USA). An in-line turbidity sensor was used to detect the onset of nucleation. The dual optic fibre construction delivers high resolution for low turbidity measurements through detection of backscatter and is used extensively in industry for the determination of induction (InPro8200/S/Epoxy/120, Mettler Toledo, Manchester, UK). Experiments were conducted in triplicate, and the average reported.

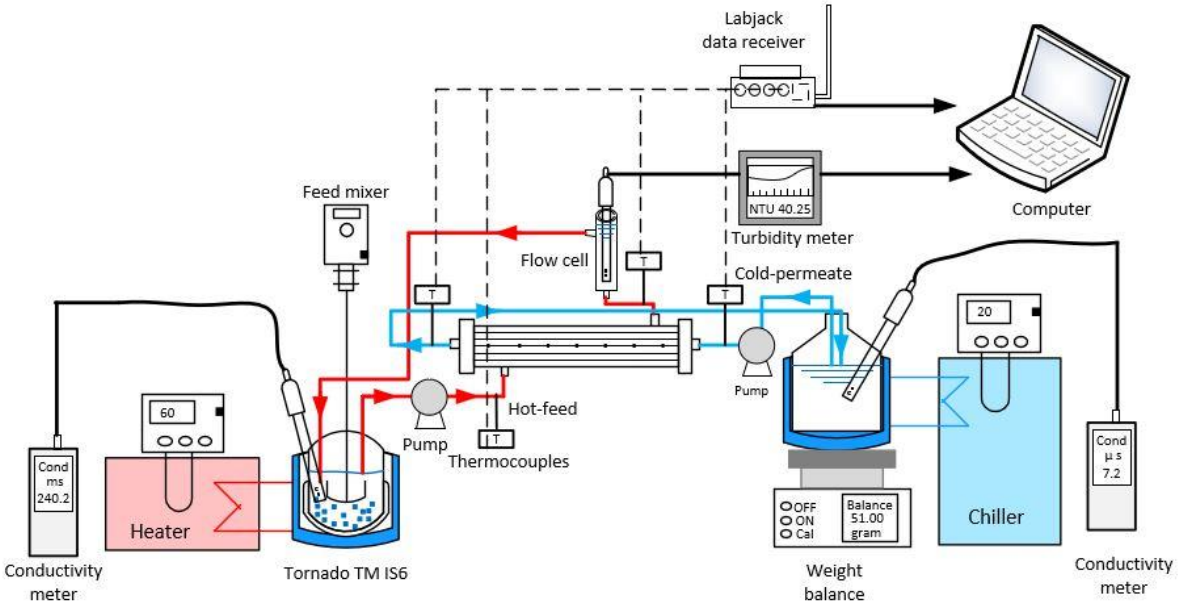

Figure 2.2 *Schematic diagram of the Membrane Distillation Crystallisation setup.*

2.2.2 Characteristics of produced crystals and membrane surface scaling

Crystals collected from the bulk were filtered through a 0.45 µm nylon filter (Whatman, Dorset, UK) and dried over a desiccant for 48 hours (temperature ~23°C) before weighing and sizing. Optical microscopy was used to collect images (Lumenera Infinity 3-3 Camera with 5/0.12 160/- lens) which were analysed for the determination of

crystal size using proprietary software (Image ProPremir 9.2). Crystal size distributions were determined in triplicate for each sample, with each distribution constructed from a minimum of 1300 crystals per batch as this exceeded the threshold at which the standard error of the distribution achieved a minimum. The coefficient of variation (CV) was calculated according to the following equation [29]:

$$CV = \frac{L_{84\%} - L_{16\%}}{2\,L_{50\%}} \quad \textbf{(2-1)}$$

where L (μm) is the crystal length of the cumulative percent function at indicated percentage. A high precision balance (range 0.02 to 62g, error ±0.0001g, Fisherbrand™, Loughborough, UK) was used to weigh each of the scaled membranes after operation, and the crystal mass normalised by membrane surface area (g m^{-2}). Scanning electron microscopy (SEM) was used to explore surface scaling characteristics using an acceleration voltage of 20 kV (TESCAN VEGA3, Cambridge, UK).

2.2.3 Mass and heat transfer characterisation in membrane distillation

Permeate flux N (kg m^{-1} h^{-1}) was calculated experimentally as [30]:

$$N = \frac{m}{A \times \Delta T} \quad \textbf{(2-2)}$$

where m is the mass of permeate (kg), A is the effective membrane area (m^2), and ∆T is the time interval (h). Heat transfer comprises of the latent heat Q_v (W m^{-2}) demand for water vapour transport, and heat conduction through the membrane Q_c (W m^{-2}) [30]:

$$Q = Q_c + Q_v = \left(\frac{k_m}{\delta_m}\right)\left(T_{fm} - T_{pm}\right) + NH_{V,T} \quad \textbf{(2-3)}$$

where δ_m (m) is the membrane thickness, and k_m (W m^{-1} K^{-1}) is the membrane thermal conductivity [31]:

$$k_m = k_p(1-\varepsilon) + k_g\varepsilon \quad \textbf{(2-4)}$$

where k_p (W m^{-1} K^{-1}) is the polymer thermal conductivity and k_g (W m^{-1} K^{-1}) is the air thermal conductivity. $H_{V,T}$ (KJ kg^{-1}) is the vapour latent heat [14,32]:

$$H_{V,T} = 1.7535\,\mathrm{T} + 2024.3 \quad \textbf{(2-5)}$$

where $\mathrm{T} = \frac{T_{fm}+T_{pm}}{2}$, is the average temperature at the membrane surface. The feed and permeate temperature adjacent to membrane surface, T_{fm} and T_{pm} (K), can be calculated by iteration [25] from the heat transfer relationship [30]:

$$T_{fm} = T_f - \left(T_f - T_p\right)\left[\frac{1/h_f \times d_i/d_o}{1/h_f \times d_i/d_o + 1/(h_m + h_v) + 1/h_p}\right] \quad \textbf{(2-6)}$$

$$T_{pm} = T_p - \left(T_f - T_p\right)\left[\frac{1/h_p}{1/h_f \times d_i/d_o + 1/(h_m + h_v) + 1/h_p}\right] \quad \textbf{(2-7)}$$

where d_i/d_o (unitless) is the ratio of inner/outer diameter, T_f and T_p (K) are the bulk temperature in feed and permeate, $h_m = k_m/\delta_m$ (W m^{-2} K^{-1}) is the heat transfer coefficient of the membrane, and h_v (W m^{-2} K^{-1}) is the heat transfer coefficient involved with vapour flow, assuming constant membrane temperature:

$$h_v = \frac{NH_{v,(T_{fm}+T_{pm})/2}}{(T_{fm} - T_{pm})} \quad \textbf{(2-8)}$$

where h_f and h_p (W m^{-2} K^{-1}) are the heat transfer coefficients associated with the liquid film of feed and permeate sides and can be calculated from the following equation:

$$h_{f,p} = Nu \times \frac{k_{f,p}}{d_{h_{f,p}}} \quad \textbf{(2-9)}$$

where $k_{f,p}$ (W m^{-1} K^{-1}) is the thermal conductivity of feed/permeate, $d_{h,f,p}$ (m) is the hydraulic diameter of feed/permeate flow channel, Nu is Nusselt's number, Re is Reynold's number and Pr is Prandtl's number (Appendix A).Thus, the temperature difference between the bulk solution and membrane surface can be described by the temperature polarisation coefficient:

$$TPC = \frac{T_{fm} - T_{pm}}{T_f - T_p} \quad \textbf{(2-10)}$$

The interfacial concentration C_{fm} (g $_{NaCl}$ g^{-1} $_{solution}$) close to the membrane surface is distinct from the feed bulk concentration C_{fb} (g $_{NaCl}$ g^{-1} $_{solution}$) and can be described by the concentration polarisation [33]:

$$CPC = \frac{c_{fm}}{c_{fb}} = exp\left(\frac{N}{\rho \times k_s}\right) \quad \textbf{(2-11)}$$

where N (kg m^{-1} h^{-1}) is the permeate flux, ρ (kg m^{-3}) density of the solution and k_s (m s^{-1}) is the solute mass transfer coefficient which can be estimated based on Appendix; [34].

2.2.4 Nucleation kinetics characterisation

The nucleation rate J (No. m^{-3} s^{-1}) is expressed according to Arrhenius's approach as follows, where ΔG* is the critical nucleation barrier at a given supersaturation [35]:

$$\mathrm{J} = A \exp\left(-\frac{\Delta \mathrm{G}*}{K\,T}\right) = A \exp\left(-\frac{16\pi v_{\circ}^{2}\gamma^{3}}{3(k_B T)^{3} ln^{2} s}\right) \quad \textbf{(2-12)}$$

$$\Delta \mathrm{G}* = \frac{16\pi v_{\circ}^{2}\gamma^{3}}{3(k_B T)^{2} ln^{2} s} \quad \textbf{(2-13)}$$

where ΔG^* (kJ mol^{-1})is the critical nucleation barrier at a given supersaturation, k_B (1.38 x 10^{-23} J K^{-1}) is the Boltzmann constant [36], $v_o = M/\rho_{cry}N_a$ (m^3) is the molecular volume, M (kg mol^{-1}) is the molar weight, ρ_{cry} is crystal density, N_a is Avogadro's number (6.022 x 10^{23} molecules mol^{-1}), T is the nucleation temperature (K), S=C/C* (unitless) supersaturation degree, γ is the interfacial energy (mJ m^{-2}). Nucleation rate and induction time have an inverse relationship according to classical nucleation theory [20].

$$t_{ind} \propto \frac{1}{J} \quad \textbf{(2-14)}$$

which can be related to the extent of supersaturation:

$$\ln t_{ind} = \ln A + \left(\frac{16\pi v_{\circ}^{2}\gamma^{3}}{3(k_B T)^{2} ln^{2} s}\right) = \ln A + \left(\frac{B}{ln^{2} s}\right) \quad \textbf{(2-15)}$$

where A (m^{-3} s^{-1}) is the pre-exponential parameter (intercept), B is the thermodynamic parameter for nucleation (gradient) [38]. The linear relationship between $\ln(t_{ind})$ and $1/(\ln^2 S)$, enabling determination of nucleation mechanism (homogenous or heterogenous) from the degree of linear slopes.

The MSZW was calculated by adoption the approach proposed by Nývlt [26], where the maximum MSZW at membrane surface $\Delta C_{max.fm}$ (mg g^{-1} solution) is assumed to be proportional to the concentrating rate within MCr (R'= dc/dt) (g 100g $solution^{-1}$ h^{-1}) [8,38,39] as follows:

$$\Delta \mathrm{C} = \left(\frac{\mathrm{dC}}{\mathrm{dT}}\right)_T R' \quad \textbf{(2-16)}$$

$$R' = \left(\frac{\mathrm{dCo}}{\mathrm{dt}}\right)_t = \frac{F_p\, C_0}{m_0 - \int_0^t F_P d\tau} \quad \textbf{(2-17)}$$

where F_p (kg h^{-1}) is the permeate flow rate. Following the approach of Nývlt (1968), the relation between the nucleation rate J (No. m^{-3} s^{-1}) and the maximum supersaturation $\Delta C_{max.fm}$ (g_{NaCl} g^{-1} solution) adjacent to membrane surface can be expressed by the empirical power-law equation:

$$\mathrm{J} = \mathrm{k}(\Delta \mathrm{C}_{\mathrm{max,fm}})^{\mathrm{n}} \quad \textbf{(2-18)}$$

where k (No. m^{-3-n} s^{-1+n}) is the nucleation rate constant, n (unitless) is the nucleation order, $\Delta C_{max,fm}$ is the maximum supersaturation (c_{fm}-c*), c_{fm} (g_{NaCl} g^{-1} solution) is the feed

membrane surface concentration and c* (g_{NaCl} g^{-1} $_{solution}$) is the saturation concentration. Combining equations (17) and (18), the nucleation rate (J) provided by continuous solvent removal is:

$$J = k(\Delta C_{max,fm})^n = \left(\frac{dc_0}{dt}\right)_t = \frac{F_p C_0}{m_0 - \int_0^t F_P d\tau} \quad \textbf{(2-19)}$$

Once supersaturation reaches the MSZW limit ($\Delta C_{max,fm}$), the logarithm form is described as:

$$\ln(\Delta C_{max,fm}) = \frac{1}{n}\ln\left(\frac{C_0}{k}\right) + \frac{1}{n}\ln\left(\frac{F_p}{m_0 - \int_0^t F_P d\tau}\right) \quad \textbf{(2-20)}$$

From linearly fitting $\ln(\Delta C_{max,fm})$ and ln(R'), the nucleation rate constant (k) and nucleation order (n) can be calculated.

2.3 Result and discussion

2.3.1 Impact of increasing membrane area on nucleation at fixed flux

To examine the effect of increasing membrane area on induction (the onset of nucleation), permeation flux was measured as this is generally considered to provide the driving force for nucleation (Figure 2.3) [9]. A constant temperature difference (ΔT) of 20±2°C was maintained by fixing feed velocity for each membrane module. Consequently, comparable membrane flux of around 3.5 kg m^{-2} h^{-1} was achieved for each membrane, except for the 37 HF module which recorded a slightly lower flux of 2.8 kg m^{-2} h^{-1}. This slight reduction in flux may have been induced by the higher packing density (Table 2.1) which has been shown to impose preferential flow patterns that can reduce the perceived local superficial velocity [40]. Importantly, while comparable fluxes were achieved for each membrane, the extent of supersaturation that was achieved before flux decline, was dependent upon the membrane surface area (Figure 2.3b).

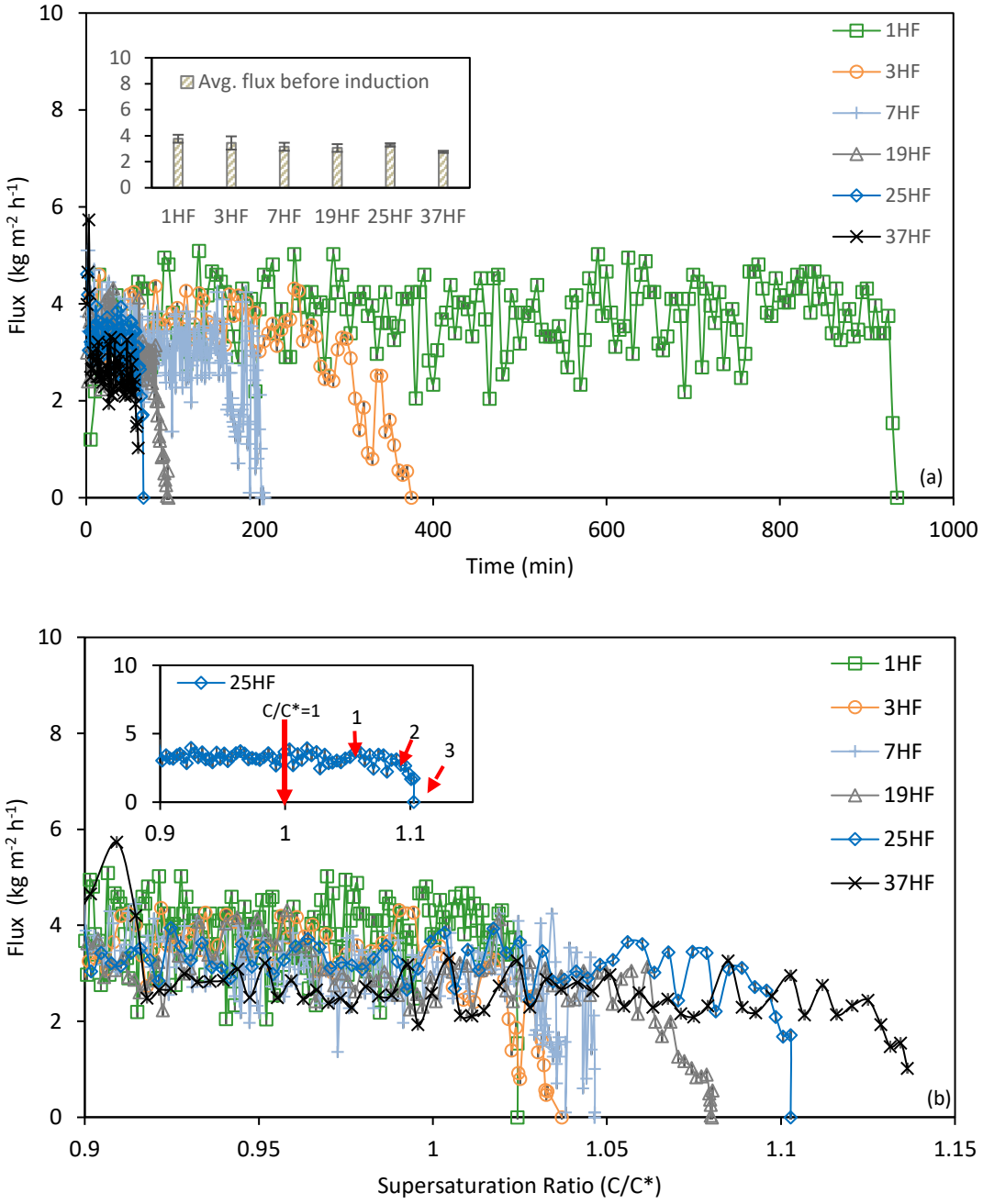

Figure 2.3 *Permeation flux during MCr operation time for different membrane modules: (a) over time; and (b) evidencing flux decline against the progressively supersaturated fluid. Boundary conditions: Tbulk , 55±1°C; ΔTmembrane, 20±2°C; initial feed NaCl concentration, 23.9 wt.%. Standard error of permeation flux was calculated based on differences in triplicate measurements for each membrane modules; 1 HF, 3.8±0.3; 3HF, 3.4±0.5; 7HF, 3.2±0.3; 19HF, 3.1±0.3; 25HF, 3.3±0.1; 37HF, 2.8±0.1.*

To illustrate, a significant flux decline was observed at 895, 57 and 47 minutes for 1, 25 and 37 HF membrane modules respectively. Each flux profile comprised of three consecutive stages (Figure 2.3b, inset): (i) a period of steady-state filtration, with a slow progressive decline in flux initiated by the increase in solute concentration which reduced water activity [41,42]; (ii) an inflection point, which marks a disruption in water vapour transport; and (iii) a rapid loss in water vapour flux [25,30]. This inflection point is often associated to the initiation of nucleation, while the subsequent reduction in vapour pressure is attributed to the mass and heat transfer resistance provided by the crystal phase which can develop at the membrane surface through adhesive growth or via deposition following nucleation and crystal growth in the bulk solution [9,17,25].

Turbidimetric profiles confirmed the onset of bulk nucleation (Figure 2.4). The time required to produce a crystal phase decreased from 930 min for 1 fibre, to 60 min for the 37 HF membrane. Bulk nucleation was consistently observed after the rapid flux decline was observed, while the time between the flux decline and bulk nucleation shortened as membrane area was increased. The time between the saturation state (c/c*, 1) and the first detected nuclei is defined as the induction time, which indicates the onset of primary nucleation [22,37,43] (Figure 2.4b). The induction time is therefore a measure of the kinetic metastability of solution. With an increase in membrane area, induction time decreased, but the supersaturation level achieved at induction increased. For instance, with 1 HF module, induction time was 143 min, corresponding to bulk supersaturation (c/c*) of 1.02, whereas an induction time of 24 minutes, and c/c* of 1.12 was recorded for the 37 HF module. This inverse relationship between induction time and supersaturation is in accordance with the literature [20,22], when the crystallising solution is exposed to an increase in solvent removal rate. In this study, the increase in solvent removal rate is enabled through the increase in membrane area (despite constant flux, temperature and ΔT), and it is through these higher solvent removal rates that elevated supersaturation levels can be reached within the crystallising solution. This is evidenced by constructing the corresponding MSZW, which describes the difference between the solubility limit and the maximum supersaturation limit at which nucleation occurs [44] (Figure. 2.5).

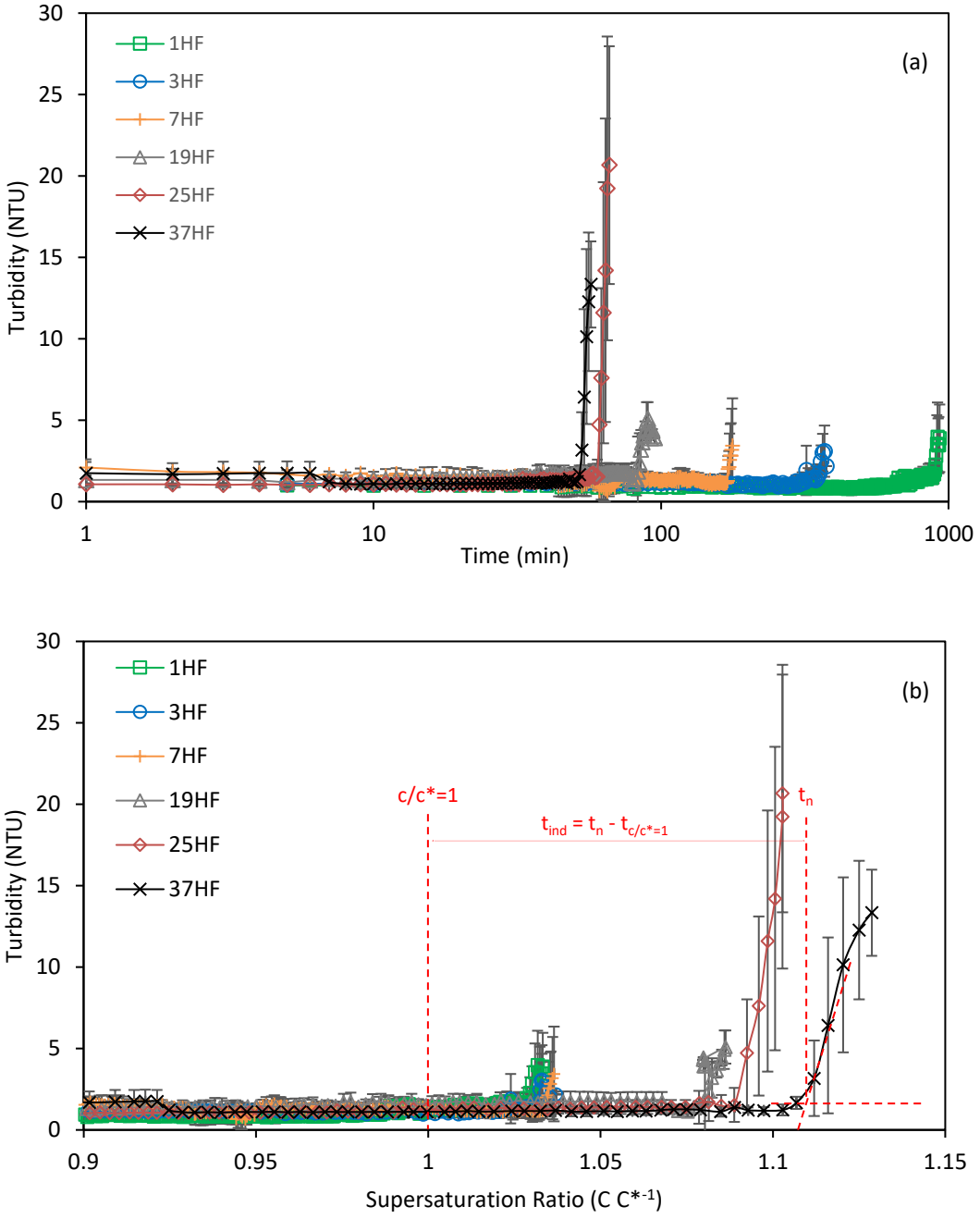

Figure 2.4 *Turbidity profile during MCr operation for membranes comprised of increasing surface area: (a) based on operating time; (b) based on bulk supersaturation. Boundary conditions: Tbulk, 55±1°C; ΔTmembrane, 20±2°C; initial feed NaCl concentration, 23.9 wt.%.*

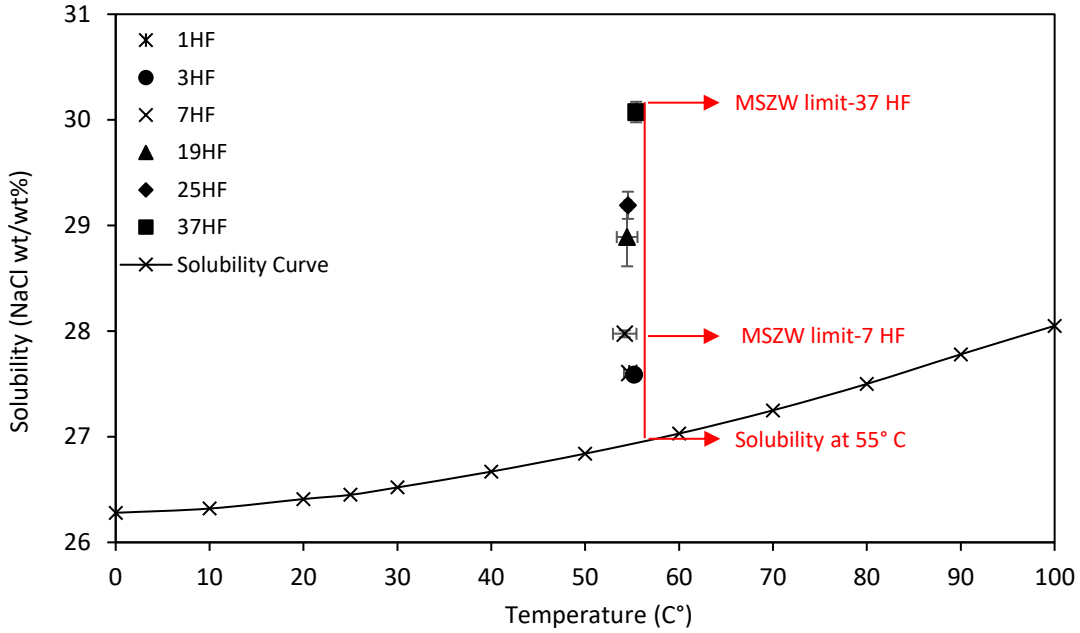

Figure 2.5 *A broad metastable region is created by increasing membrane area at fixed flux. Boundary conditions: Tbulk , 55±1°C; ΔTmembrane, 20±2°C; initial feed NaCl concentration, 23.9 wt.%.*

Increasing membrane area from 1 to 37 HF resulted in an increase in MSZW from 27.6 to 30.1% wt./wt.. According to Nývlt [26] higher supersaturation rates reduce the critical free energy barrier for nucleation due to the higher driving force provided by the elevated supersaturation gradient [8,39,45]. Consequently, membrane area can be adjusted to mediate the size of the MSZW, which will likely inform the kinetics of nucleation and crystal growth, in addition to the specific primary nucleation mechanism which determines the probability for scaling phenomena that remain an acknowledged limitation for membrane distillation and crystallisation [8,46].

2.3.2 Shifting induction time by using membrane area to increase concentration rate

Since mass and heat transfer can collectively modify supersaturation locally, concentration and temperature polarisation were characterised to confirm that increasing membrane area did not significantly adjust the boundary layer conditions which can otherwise increase the maximum supersaturation near the membrane interface at induction ($\Delta C_{max,fm}$) (Figure 2.6).

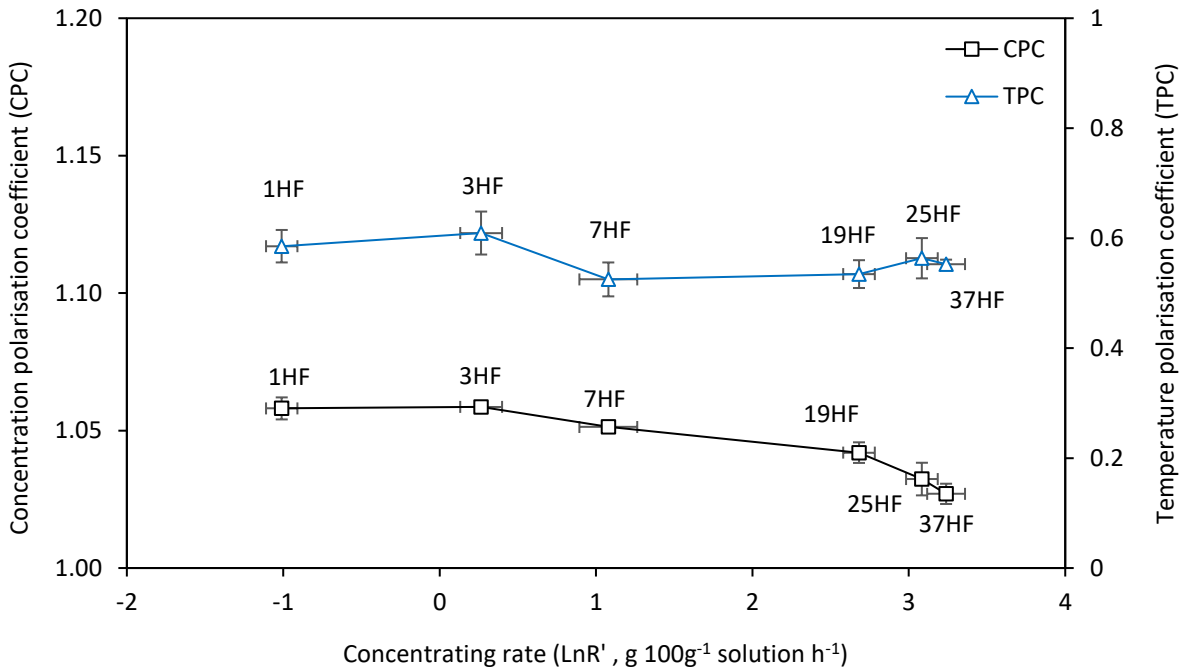

Figure 2.6 *The CPC and TPC of supersaturation at induction over different concentration rate (LnR'). bulk (°C) = (55±1), ΔT membrane (°C) = (20±2), Velocity of feed and permeate = 0.06 m s^{-1}, initial feed concentration NaCl (wt. %) = 23.9.*

The temperature polarisation coefficient (TPC) was reasonably consistent when increasing membrane area. Higher surface area will increase conductive heat transfer losses, while the greater convective losses can be expected from the increase in net water vapour transport [42,47,48]. However, as an equivalent fluid velocity was sustained for each module, the losses are in proportion to surface area and an equivalent TPC profile was developed, which was confirmed by the consisent ΔT of 20±2°C achieved for each module. Since the solubility-temperature dependency of NaCl is relatively flat [25], the solubility constant for NaCl within the boundary layer is not markedly affected by the increase in membrane area. A slight reduction in concentration polarisation coefficient (CPC) from 1.06 to 1.03 was observed when the supersaturation rate was increased from -1.01 g $100g^{-1}$ h^{-1} for 1 HF to 3.24 g $100g^{-1}$ h^{-1} for 37 HF. Since similar hydrodynamics were consistently employed, this slight modification of CPC may relate to the extent of supersaturation achieved within the bulk solution with an increase in supersaturation rate, which will also reduce the relative vapour pressure at induction.

According to Sangwal [38], the maximum supersaturation at induction is proportional to the supersaturation rate and is linearly dependent on where within the metastable zone that nucleation occurred. This was confirmed by constructing the correlation between supersaturation rate (LnR') and the corresponding metastable zone width ($\Delta C_{max,fm}$) (Figure 2.7a). The lowest $\Delta C_{max,fm}$ of 2.62 $mg_{solute}\ g_{solution}^{-1}$ was recorded for 1HF corresponding to LnR' -1.01 g $100g^{-1}\ h^{-1}$, whereas a $\Delta C_{max,fm}$ of 3.73 mg g^{-1} was recorded for the 37HF module as LnR' increased to 3.24g $100g^{-1}\ h^{-1}$. The supersaturation rate is a direct analogy to nucleation rate [38]. Acordingly, the nucleation kinetics were ascertained from line fitting to provide a nucleation order n=0.23 (-) and nucleation constant k=2.91 No. $m^{-3-n}\ s^{-1+n}$. Nucleation order and constant are physical parameters that describe nucleation rate, relating the MSZW dependency to the concentrating rate in which its value defines the growth of stable nuclei to visible entities [27,49]. Widening of the MSZW by the supersaturation rate is consistent with the literature [19]. An increase in supersaturation rate reduces the time required to achieve induction (Figure 2.7b). This is because the elevated supersaturation lowers the energy barrier for nucleation by providing a greater driving force for solute transformation to a solid-phase [50]. Induction time is therefore inversely related to nucleation rate through classical nucleation theory, where higher nucleation rates are achieved at the shortest induction time [51].

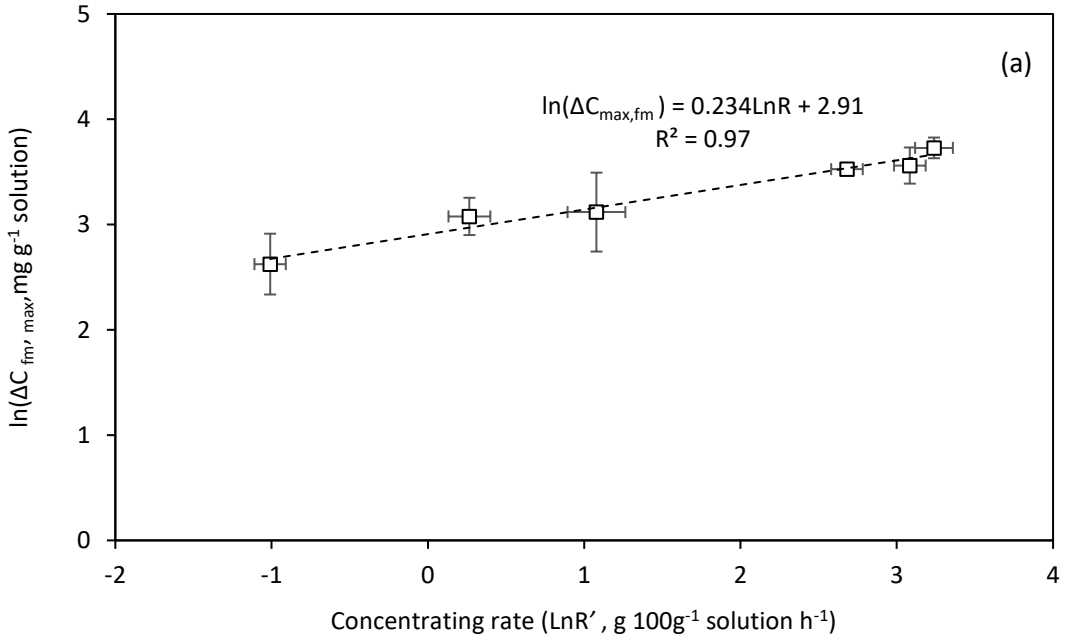

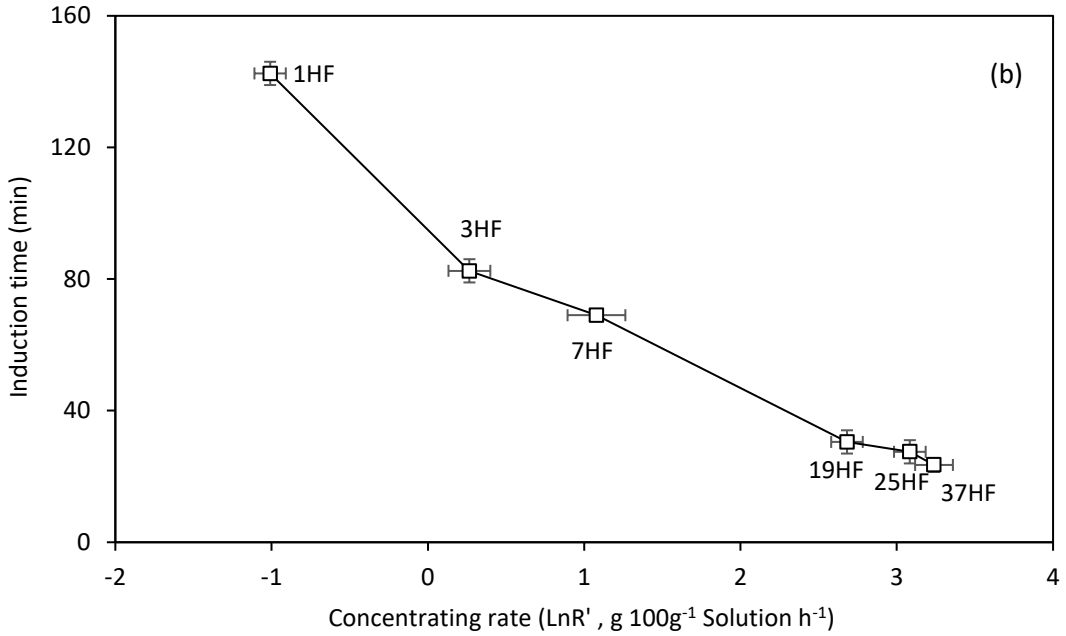

Figure 2.7 *(a) The dependence of ∆cfm, max on concentrating rate (ln R') according to equation (20) for different membrane modules, (b) The dependence of induction time on concentrating rate (LnR') for different membrane modules, bulk (°C) = (55 ±1), ∆T membrane (°C) = (20 ±2), velocity of feed and permeate = 0.06 m s^{-1}, initial feed concentration NaCl (wt. %) = 23.9.*

By increasing membrane area from 1 to 37HF, induction time reduced by 119 minutes, indicating a significant increase in nucleation rate from 8.9 x 10^{-7} to 2.2 x 10^{-5} No. m^{-3} s^{-1} (based on CNT) without obviously modifing polarisation within the boundary layer. The Gibbs free energy barrier is substantially reduced by the increase in $\Delta C_{max,fm}$ at induction. In such conditions, primary nucleation is less dependent on modification of the interfacial energy, and therefore the probability for nucleation to proceed through a homogeneous mechanism is increased [9,22,52]. This is contradictory to suggestions within the existing MCr literature, which hypothesise that it is the supersaturated conditions within the boundary layer complemented by reduction in interfacial energy introduced by the membrane that overcome the free energy barrier for nucleation [13,25]. In this study, we propose that the high supersaturation driving force imposed by the increase in supersaturation rate subsequently imposes kinetically controlled crystallisation with nucleation being more dependent on development of the closest metastable form and less dependent on the heterogeneous

substrate [19]. This is supported by comparison of supersaturation within the bulk and interfacial boundary layer adjacent to the membrane at induction (Figure 2.8). As the supersaturation rate is modified by membrane area rather than boundary layer characteristics (which would not be the case for temperature or ΔT), the difference in supersaturation between the bulk solution and interfacial region becomes negligible as supersaturation rate is increased. Consequently, it can be inferred that the probability for nucleation occurring within the bulk solution rather than at the membrane surface is comparable or greater within the upper region of the metastable zone.

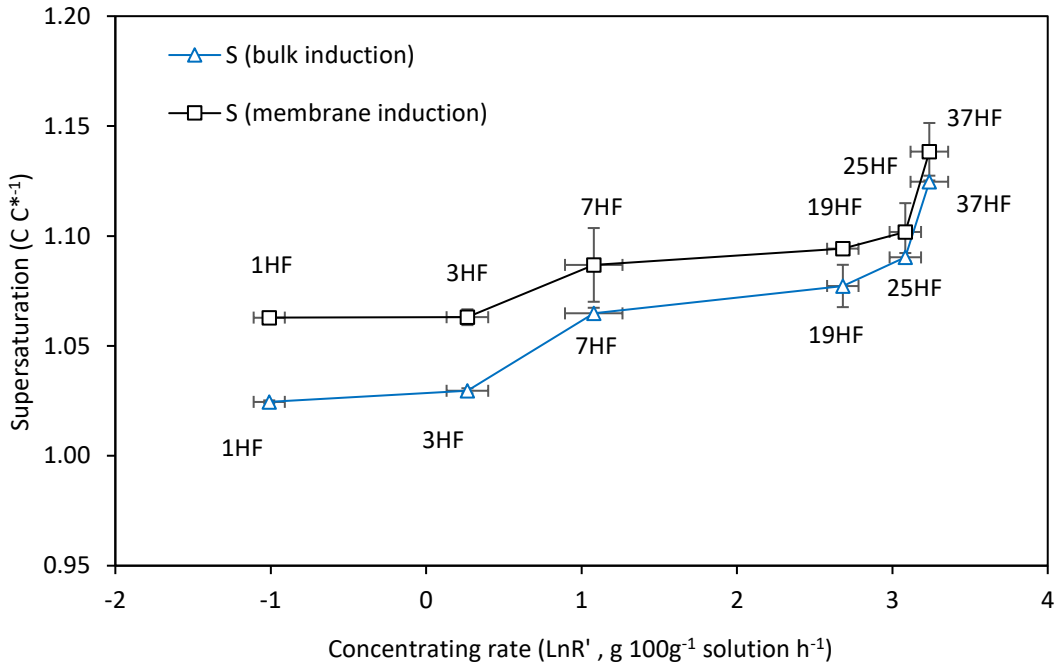

Figure 2.8 *Supersaturation degree of bulk and membrane over different concentration rate (LnR'), bulk (°C) = (55 ±1), ΔT membrane (°C) = (20 ±2), velocity of feed and permeate = 0.06 m s^{-1}, initial feed concentration NaCl (wt. %) = 23.9.*

2.3.3 Supersaturation rate defines the primary nucleation mechanism

To distinguish which primary nucleation mechanism was dominant when supersaturation rate was controlled by membrane area, rather than by local mass and heat transfer mechanisms (as with feed temperature and ΔT), diagnostic examination of scaling was conducted on each HF module following induction (Figure 2.9). An increase in the supersaturation rate reduced crystal mass deposition. Membrane

scaling is thought to proceed via two distinct mechanisms: (i) adhesive growth, following nucleation within the vicinity of the membrane; and/or (ii) the deposition of crystals that have undergone primary homogeneous nucleation in the bulk solution [17,23,53]. Microscopic examination of each membrane surface illustrated distinct growth characteristics (Figure 2.10).

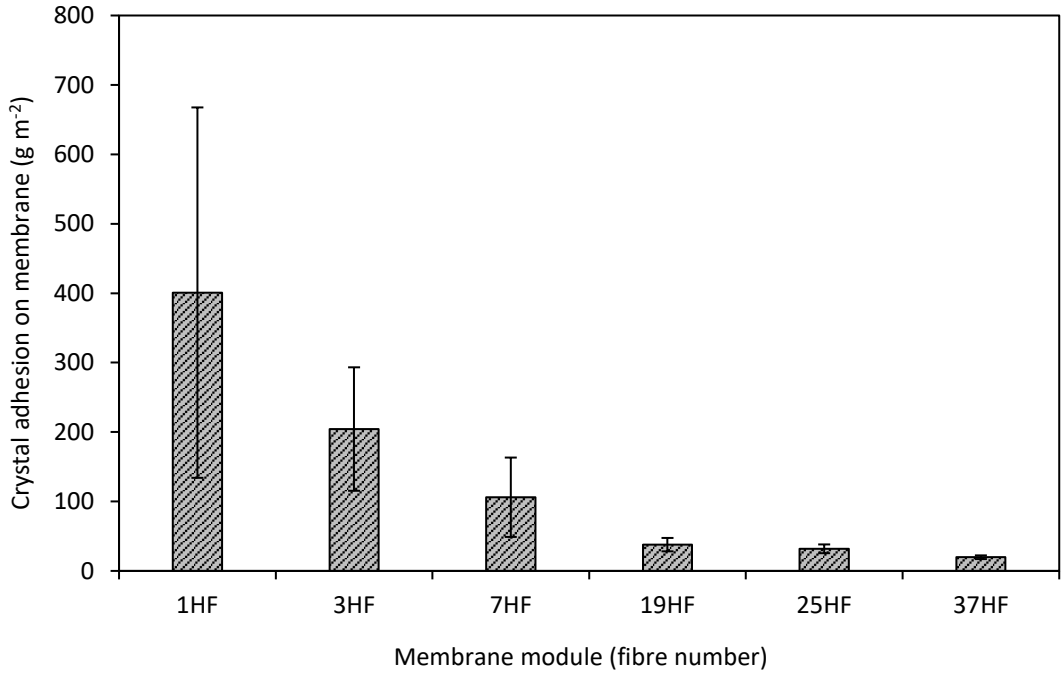

Figure 2.9 *Membrane crystal adhesion for modules of different surface area, which indicates the reduction in surface nucleation with an increase in concentration rate.*

Deposition on the hollow-fibre membranes that fostered low supersaturation rates (below 7HF), exhibited significant surface coverage, while the cubic morphology synonymous with NaCl was difficult to clearly observe. For hollow-fibre membranes that promoted higher supersaturation rates (>19HF), less deposition was noted and was confined to discrete areas, that were fewer in number as membrane surface area increased. Crystalline morphology appeared distinct from that observed at low supersaturation rates, with cubic orientation more evident but with evidence of interconnected dendritic outgrowths. This is characteristic of highly supersaturated conditions which migrate from diffusion limited to surface-integration limited crystal growth, where surface area is rapidly formed by secondary nucleation mechanisms [54].

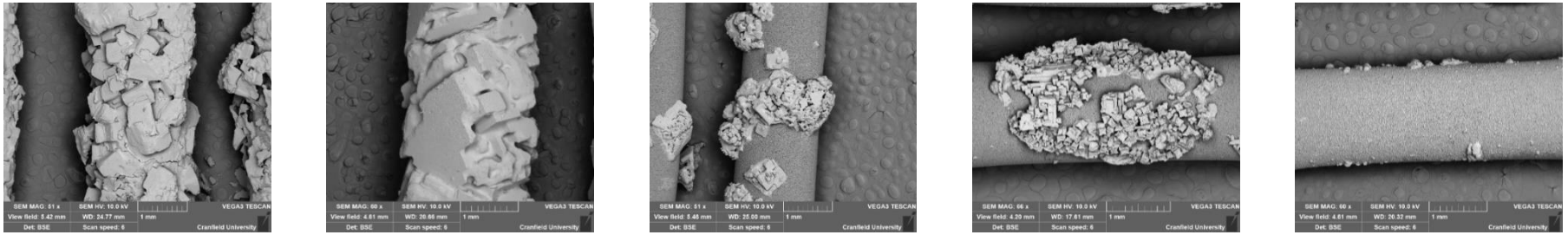

1HF 7HF 19HF 25HF 37HF

Figure 2.10 *Scanning electron microscope (SEM) images highlighting reduced surface adhesion (scaling) as concentration rate increases through an increase in membrane area. Scale bar: 1mm.*

The kinetic transition across the metastable zone was subsequently characterised to relate the specific primary nucleation mechanism to the extent and character of the deposition observed. While induction time and the supersaturation level at induction are recognised as critical crystallisation parameters that underpin scale formation, such data is rarely reported in the membrane literature [17]. In-line turbidimetry enabled direct measurement of induction time and evidenced two discrete regions of supersaturation with very different gradients (Figure 2.11).

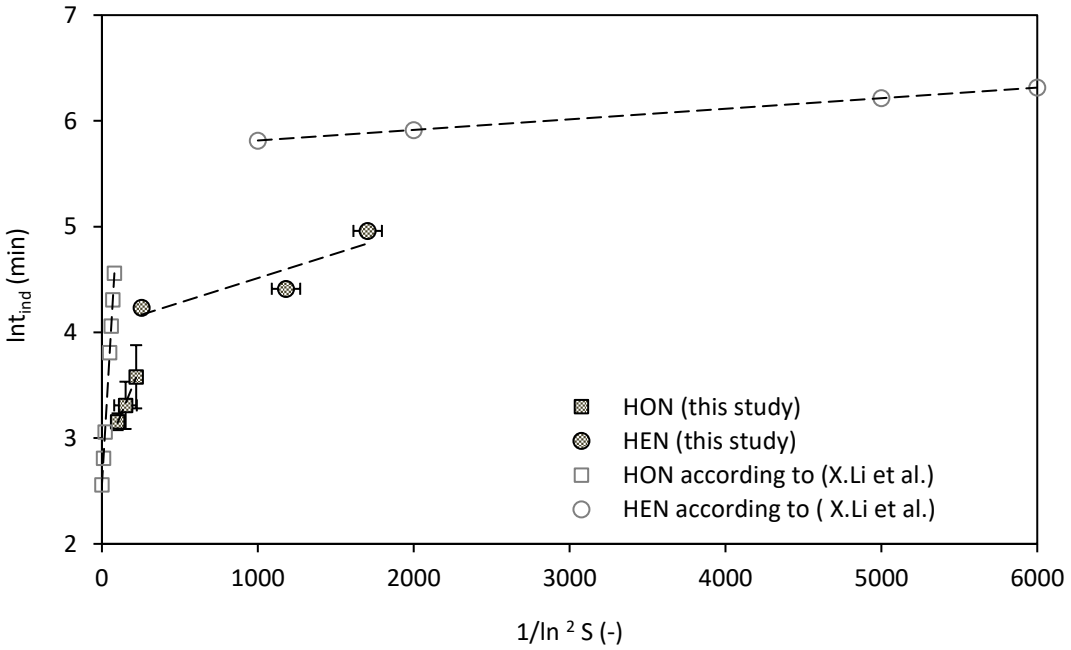

Figure 2.11 *ln (t_{ind}) versus 1/ln^{2}S for different membrane modules show different nucleation mechanism. The change in slope indicates different nucleation mechanism as reported in* [53]*.*

Induction time is a kinetic parameter that is characterised by two distinct supersaturation regions within the metastable zone, where the shallow gradient formed at low supersaturation is indicative of heterogeneous primary nucleation while the steeper curve formed at higher supersaturation represents a homogeneous primary nucleation mechanism [19,22]. The gradient of the curves represents the interfacial energy required to create a thermodynamically stable nucleus within those discrete regions of supersaturation [51]. In this study, the region of heterogeneous primary nucleation corresponded to modules with 1 to 7 HF where low supersaturation rates were observed, and substantive scaling was detected (Figure 2.10). The gradient

of the curve representing the homogeneous primary nucleation mechanism, was seven times higher, indicating the energy barrier for nucleation to be considerably lower when higher supersaturation rates were employed (>19 HF) and corresponded to supersaturation levels measured at induction (C/C*) of 1.075-1.117 (Table 2.2). This transition between nucleation mechanisms when moving across the metastable zone is comparable to previous literature observations (Figure 2.11, Table 2.2) [19,22,55]. The limited supersaturation observed for 1 to 7 HF restricts the driving force for nucleation, which increases the dependency on heterogeneous sites to modify the interfacial free energy sufficient to overcome the critical free energy barrier for nucleation [17,22,56]. For highly soluble compounds such as NaCl, nucleation tends to be more critically dependent on a heterogeneous catalyst due to the low supersaturation achieved [13].

Table 2.2 *Results analysis of nucleation parameters based on correlation of ln (t_{ind}) versus 1/ln^{2}S.*

T/K	Nucleation	Intercept (K)	Slope (m)	R^2	Supersaturation Range (c c*$^{-1}$)	Recovered mineral	Molecular weight (g mol^{-1})	Solubility	Ref.
328.15	Homogeneous	2.78	0.0036	0.99	1.075-1.117	NaCl	58.44	370 (g L^{-1})	This Study
	Heterogeneous	4.05	0.0005	0.81	1.025-1.065				
323.15	Homogeneous	6.47	0.0918	0.99	1.27-1.40	Analgin	333.34	0.027 (mol mol^{-1})	[20]
	Heterogeneous	7.88	0.0071	0.94	1.10-1.23				
283.15	Homogeneous	2.56	0.025	1	1.60-1.81	KCl	74.55	312 (g L^{-1})	[52]
	Heterogeneous	5.71	0.0001	1	1.49-1.51				

Low supersaturation tends to favour crystal growth which may explain the substantive scaling observed [57–59]. This hypothesis is supported by the limited crystal yield observed for supersaturation rates characterised as primarily undergoing a heterogeneous primary nucleation mechanism (Figure 2.12). As the supersaturation rate was increased, the crystal phase produced in the bulk solution improved, and was complemented by a reduced scaling rate (Figure 2.13), which is analogous to the description of a homogeneous primary nucleation mechanism [17,19]. Several mechanisms have been proposed to explain how the membrane promotes heterogeneous nucleation that include solute entrapment, enhanced molecular orientation and a reduction in interfacial energy [7]. In this study, microscopic examination evidenced significant scaling within the pores that dissipated with an increase in supersaturation rate. While this observation may be specific to conditions where supersaturation rate is moderated without substantive changes to the boundary layer, this preliminary data may infer that solute entrapment within the pores constitutes a significant role in initiating scaling.

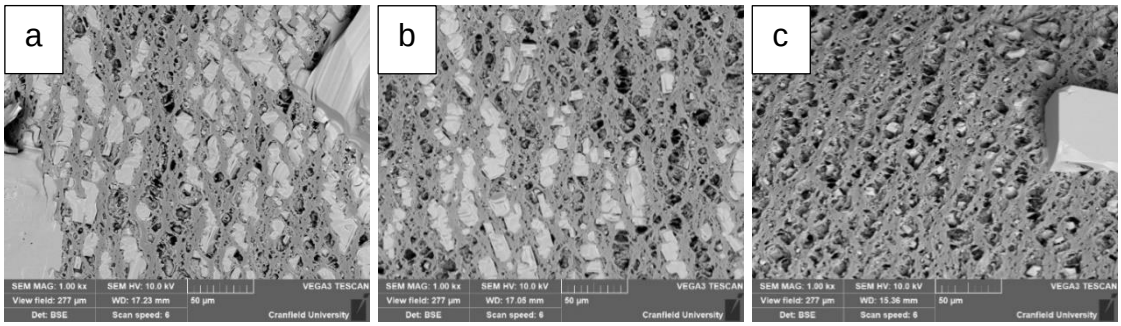

Figure 2.12 *Scanning electron microscope (SEM) images of membrane pores from membranes used in different sized modules, illustrating how the increase in concentration rate with membrane area reduces nucleation within the pore structure. Scale bar, 50μm. (a) 7HF; (b) 19HF; (C) 25HF.*

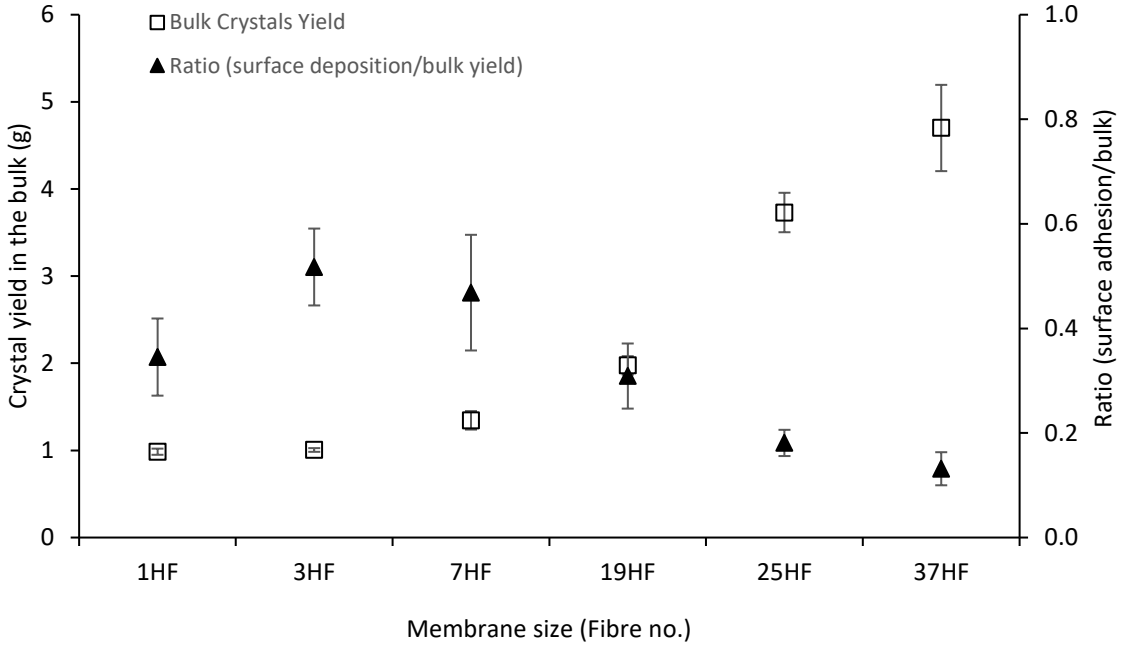

Figure 2.13 *Crystal yield produced in the bulk solution when using membranes modules of different size to increase concentration rate.*

2.3.4 How supersaturation rate determines crystal growth characteristics

The crystal phase recovered from the bulk solution was examined to understand how crystal size, size distribution and morphology may be influenced by the supersaturation rate. The crystal growth kinetics broadly correlated to where within the metastable zone that growth was initiated, with the crystal size distribution observed to shift right as supersaturation rate was increased (Figure 2.14). To illustrate, mean crystal size ($L_{4,3}$) was 195µm at the highest supersaturation rate (37 HF), and reduced to 107µm at the lowest supersaturation rate (Table 2.3). This is not consistent with classical crystallisation where fewer, larger crystals are generally favoured at low supersaturation rates [45]. This may explained by the competition between nucleation and crystal growth in highly supersaturated solutions (particularly relevant for high solubility aqueous salts) characterised by short induction times which tend to favour Ostwald ripening, where the produced nuclei have little time to grow into a thermodynamically stable phase, which results in dissolution and the redeposition onto stable crystals resulting in substantive growth [60]. Higher

supersaturation generally constrains crystal growth, as the high nucleation rates inhibit ion availability for growth [61]. While a similar response may be expected for MD operation when ΔT is adjusted, as this will raise the supersaturation profile only within the boundary layer, this is not the case when increasing supersaturation with membrane area, as the supersaturation profiles within the bulk and boundary layer both increase. Consequently, despite the higher supersaturation profile instigating higher nucleation rates when membrane area is increased, there is likely to be sufficient ion within the bulk condition following nucleation to enhance growth.

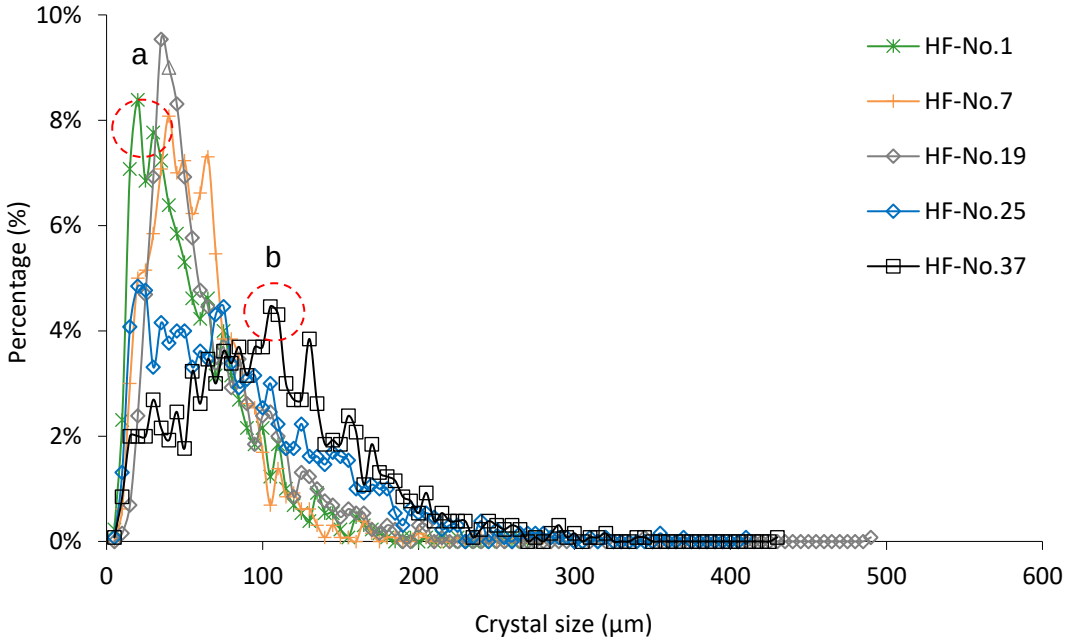

Figure 2.14 *Crystals Size Distribution (CSD) based on volume fraction (%).*

The coefficient of variation (CV) represents the distribution of produced crystal sizes which can be important for product end use [29]. In general, the CV was lower for the higher supersaturation rates examined. For each supersaturation rate studied, the crystal phase produced in the bulk solution was of cubic habit which conforms with expected growth patterns [31]. However, modifying the supersaturation rate with membrane area initiated morphological distinctions in the end crystal product (Figure 2.15).

Table 2.3 *CSD parameters of recovered crystals from different membrane sizes*

Membrane module	Volume-based mean crystal size ($L_{4,3}$, µm)	Coefficient of variation (CV, %)	Volume-based crystal's percentile (µm)		
			L_{10}	L_{50}	L_{90}
37 HF	195±1	0.49±0.07	31±8	98±19	178±13
19 HF	184±10	0.56±0.08	27±7	51±4	115±9
7 HF	112±17	0.63±0.12	12±7	30±15	75±5
1 HF	107±23	0.60±0.04	12±2	29±11	66±24

The cubic face formed at high supersaturation rates (e.g. 37 HF) was characterised by a 'rough growth' pattern, whereas under low supersaturation rates (e.g. 1 HF) the growth followed a spiral growth mechanism [62]. This can be explained based on the kinetics-based model that describes the absorption and subsequent diffusion of molecules on the crystal surface until incorporated into the crystal lattice [62]. At a higher supersaturation level, the growth unit is incorporated into the crystal lattice with either two or three bonding sides, invoking rough growth pattern [62,63]. While at lower supersaturation the growth unit is incorporated into the crystal lattice at a flat surface with one bonding side, providing a faster growth in the centre compared to edges [62,63]. Consequently, crystal morphology depends on the supersaturation environment that determines the crystal growth mechanism.

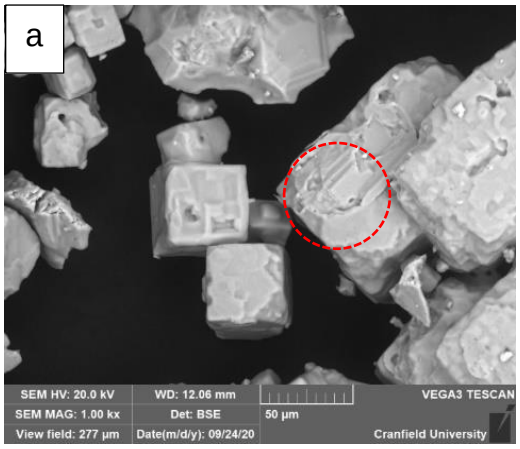

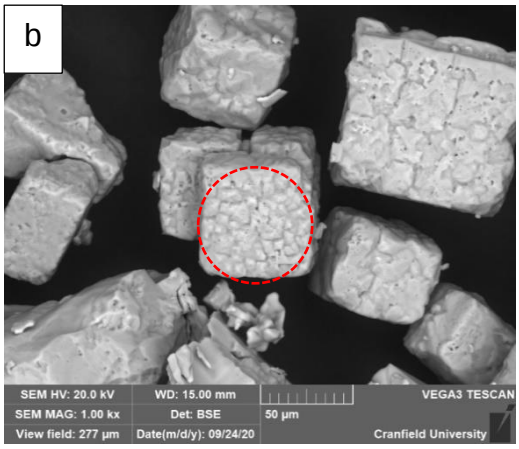

Figure 2.15 *Scanning electron microscope (SEM) images of: (a) crystals produced from 1HF experiment (scale bar, 50μm), (b) crystals produced from 37 HF experiment, evidencing distinct growth patterns upon increasing concentration rate.*

2.4 Conclusions

In this study, the metastable zone has been quantitatively described in membrane distillation crystallisation by using in-line turbidimetry to provide a framework with which to define explicit scaling and crystal growth mechanisms which to date have been rarely described. Supersaturation rate was modified by membrane area rather than through adjustment of water vapour flux. This approach enabled the detailed characterisation of scaling mechanisms that could be explained through classical nucleation theory and may be more difficult to delineate when modifying boundary layer hydrodynamics, feed temperature or temperature difference due to the simultaneous modification of supersaturation rate, temperature polarisation and concentration polarisation. An increase in supersaturation rate reduced induction time and increased supersaturation at induction. This increased nucleation rate and was complemented by a reduction in scaling. While this conforms with classical nucleation theory, it contradicts recommendations in the literature, which generally advocate for operation within a region of low supersaturation. This was explained by the modification of the supersaturation rate independent of boundary layer characteristics which resulted in a comparable supersaturated state within the bulk and boundary layer once supersaturation rate was increased and is a critical foundation for the development of scaling mitigation strategies. Two discrete regions for primary nucleation were described to discriminate between heterogeneous and homogeneous nucleation mechanisms and their physical relevance confirmed through characterisation of the scale deposit formed within each domain. Crystal growth could be described within the scale deposit and bulk crystal phase and related to the local supersaturation, which also informed on crystal size. While further work is required to confirm, the physical characteristics of the crystal phase within the bulk solution appear distinct from those within the scale deposit,

which would indicate that the mechanisms of scale formation and of bulk crystal formation may be phenomenologically distinct.

Membrane distillation is a contemporary solution for evaporative crystallisation where poor regulation of nucleation is common as mixing is generally in a discrete domain of the mass transfer zone, while the decoupling of heat and mass transfer have also made crystal growth difficult to control. This study evidences that with control of heat and mass transfer over a well-defined surface area, nucleation rate and crystal growth can be regulated and in a scalable platform technology. High solubility salts are most likely to initiate adhesive growth due to their greater dependency on heterogeneous primary nucleation. However, membrane area-to-volume ratio has been demonstrated to mitigate scaling by sodium chloride, which evidences membrane distillation as a valid option for zero liquid discharge of desalination brines. The increase in crystal size with nucleation rate is a seemingly unique facet of this configuration and is likely a function of the two discrete regions of supersaturation that are initiated. Importantly, this provides an enhanced capability for crystal growth control in evaporative crystallisers, which are ordinarily limited to regulation by simple temperature setpoint. Although an increase in hollow-fibre membrane area also increased packing density to a commercially relevant fractional volume, less scaling (by adhesion or deposition) was observed at higher membrane areas. We therefore propose that it may be possible to translate similar operation to a wider set of membrane configurations (e.g. spiral wound) characterised by narrow channels without incurring substantive risk based on this work, provided kinetic modification of the supersaturation is facilitated to preference a homogeneous primary nucleation pathway.

2.5 Acknowledgements

This research was financially supported by European Research Council Starting Grant, ‘Sustainable chemical alternatives for reuse in the circular economy’ (StG, SCARCE, 714080). The data underlying this paper can be accessed through the following DOI: 10.17862/cranfield.rd.22775144

2.6 Appendix A

Nusselt number, Reynold number and Prandtl number were calculated using the following equations:

$$Nu = 1.86(Re\,\mathrm{Pr}\,{}^{d_h}/_{L})^{0.33} \quad \textbf{(A 2-1)}$$

$$Re = \frac{d_h V \rho}{\mu} \quad \textbf{(A 2-2)}$$

$$Pr = \frac{C_p \mu}{k} \quad \textbf{(A 2-3)}$$

where v, ρ, μ and c_p are the velocity (m s^{-1}), density (kg m^{-3}), viscosity (Pa s^{-1}) and specific heat of feed/permeate (J kg^{-1} K^{-1}) respectively and L (m) is the hollow fibre length. The solute mass transfer coefficient k_s (m s^{-1}) is estimated using the following equations:

$$\frac{Sh_f}{Sc_f^{0.33}} = \frac{Nu_f}{Pr_f^{0.33}} \quad \textbf{(A 2-4)}$$

where Sherwood (Sh) and Schmidt (Sc):

$$Sh_f = \frac{k_s D_h}{D_s} \quad \textbf{(A 2-5)}$$

$$Sc_f = \frac{\mu_f}{P_f D_s} \quad \textbf{(A 2-6)}$$

The growth rate can be calculated according to classical nucleation theory as follows:

$$G = K_G\ (\text{c-c*})^{\text{g}} \quad \textbf{(A 2-7)}$$

$$\log(G) = \log(K_G) + g\log(c - c*) \quad \textbf{(A 2-8)}$$

where K_G is the kinetic rate constant, (c-c*) is the growth driving force, c (g $_{NaCl}$ g^{-1} $_{solution}$) is the feed bulk concentration and c* (g $_{NaCl}$ g^{-1} $_{solution}$) is the solubility. Linearisation of the relationship between log(G) and log(c-c*), yields (g) as the gradient of the curve and $\log(K_G)$ as intercept.

2.7 References

[1] M.C. Sparenberg, I. Ruiz Salmón and P. Luis, Economic evaluation of salt recovery from wastewater via membrane distillation-crystallization, Purif. Technol. 235 (2020) 116075.

[2] Q. Chen, M. Burhan, M.W. Shahzad, D. Ybyraiymkul, F.H. Akhtar, Y. Li and K.C. Ng, A zero liquid discharge system integrating multi-effect distillation and evaporative crystallization for desalination brine treatment, Desalination. 502 (2021) 114928.

[3] A. Jones, S. Rigopoulos and R. Zauner, Crystallization and precipitation engineering, Comput. Chem. Eng. 29 (2005) 1159–1166.

[4] J. Ulrich and P. Frohberg, Problems, potentials and future of industrial crystallization, Front. Chem. Sci. Eng. 7 (2013) 1–8.

[5] A. V. Mohod and P.R. Gogate, Improved crystallization of ammonium sulphate using ultrasound assisted approach with comparison with the conventional approach, Ultrason. Sonochem. 41 (2018) 310–318.

[6] E. Chabanon, D. Mangin and C. Charcosset, Membranes and crystallization processes: State of the art and prospects, J. Memb. Sci. 509 (2016) 57–67.

[7] G. Di Profio, E. Curcio and E. Drioli, Supersaturation control and heterogeneous nucleation in membrane crystallizers: Facts and perspectives, Ind. Eng. Chem. Res. 49 (2010) 11878–11889.

[8] X. Jiang, X. Ruan, W. Xiao, D. Lu and G. He, A novel membrane distillation response technology for nucleation detection, metastable zone width measurement and analysis, Chem. Eng. Sci. 134 (2015) 671–680.

[9] X. Jiang, L. Tuo, D. Lu, B. Hou, W. Chen and G. He, Progress in membrane distillation crystallization: Process models, crystallization control and innovative applications, Front. Chem. Sci. Eng. 11 (2017) 647–662.

[10] I. Ruiz Salmón and P. Luis, Membrane crystallization via membrane distillation, Chem. Eng. Process. Process Intensif. 123 (2018) 258–271.

[11] H. Elcik, L. Fortunato, A. Alpatova, S. Soukane, J. Orfi, E. Ali, H. AlAnsary, T.O. Leiknes and N. Ghaffour, Multi-effect distillation brine treatment by membrane distillation: Effect of antiscalant and antifoaming agents on membrane performance and scaling control, Desalination. 493 (2020) 114653.

[12] M. Gryta, Fouling in direct contact membrane distillation process, J. Memb. Sci. 325 (2008) 383–394.

[13] Y. Choi, G. Naidu, L.D. Nghiem, S. Lee and S. Vigneswaran, Membrane distillation crystallization for brine mining and zero liquid discharge: Opportunities, challenges, and recent progress, Environ. Sci. Water Res. Technol. 5 (2019) 1202–1221.

[14] A. Ali, C.A. Quist-Jensen, F. Macedonio and E. Drioli, Application of membrane crystallization for minerals' recovery from produced water, Membranes. 5 (2015) 772–792.

[15] F. Edwie and T.S. Chung, Development of simultaneous membrane distillation-crystallization (SMDC) technology for treatment of saturated brine, Chem. Eng. Sci. 98 (2013) 160–172.

[16] G. Naidu, S. Jeong and S. Vigneswaran, Influence of feed/permeate velocity on scaling development in a direct contact membrane distillation, Purif. Technol. 125 (2014) 291–300.

[17] T. Horseman, Y. Yin, K.S. Christie, Z. Wang, T. Tong and S. Lin, Wetting, Scaling, and Fouling in Membrane Distillation: State-of-the-Art Insights on Fundamental Mechanisms and Mitigation Strategies, ACS ES&T Eng. 1 (2021) 117–140.

[18] C. Bian, H. Chen, X. Song and J. Yu, Metastable zone width and the primary nucleation kinetics for cooling crystallization of NaNO3 from NaCl-NaNO3-H2O system, J. Cryst. Growth. 518 (2019) 5–13.

[19] G. Di Profio, S. Tucci, E. Curcio and E. Drioli, Controlling polymorphism with membrane-based crystallizers: Application to form i and II of paracetamol, Chem. Mater. 19 (2007) 2386–2388.

[20] L. Zhou, Z. Wang, M. Zhang, M. Guo, S. Xu and Q. Yin, Determination of metastable zone and induction time of analgin for cooling crystallization, Chinese J. Chem. Eng. 25 (2017) 313–318.

[21] T. Tong, A.F. Wallace, S. Zhao and Z. Wang, Mineral scaling in membrane desalination: Mechanisms, mitigation strategies, and feasibility of scaling-resistant membranes, J. Memb. Sci. 579 (2019) 52–69.

[22] M. Lenka and D. Sarkar, Determination of metastable zone width, induction period and primary nucleation kinetics for cooling crystallization of L-asparaginenohydrate, J. Cryst. Growth. 408 (2014) 85–90.

[23] J. Kim, J. Kim and S. Hong, Recovery of water and minerals from shale gas produced water by membrane distillation crystallization, Water Res. 129 (2018) 447–459.

[24] L.D. Tijing, Y.C. Woo, J.S. Choi, S. Lee, S.H. Kim and H.K. Shon, Fouling and its control in membrane distillation-A review, J. Memb. Sci. 475 (2015) 215–244.

[25] M.T. Chan, A.G. Fane, J.T. Matheickal and R. Sheikholeslami, Membrane distillation crystallization of concentrated salts - Flux and crystal formation, J. Memb. Sci. 257 (2005) 144–155.

[26] K. Sangwal, A novel self-consistent Nývlt-like equation for metastable zone width determined by the polythermal method, Cryst. Res. Technol. 44 (2009) 231–247.

[27] J. Nývlt, Kinetics of nucleation in solutions, J. Cryst. Growth. 3–4 (1968) 377–383.

[28] C.J. Davey, M. Hermassi, E. Allard, M. Amine, N. Sweet, T.S. Gaite, A. McLeod and E.J. McAdam, Integrating crystallisation into transmembrane chemical absorption: Process intensification for ammonia separation from anaerobic digestate, J. Memb. Sci. 611 (2020) 118236.

[29] M.C. Sparenberg, S. Chergaoui, V. Sang Sefidi and P. Luis, Crystallization control via membrane distillation-crystallization: A review, Desalination. 519 (2022) 115315.

[30] X. Yang, R. Wang, L. Shi, A.G. Fane and M. Debowski, Performance improvement of PVDF hollow fiber-based membrane distillation process, J. Memb. Sci. 369 (2011) 437–447.

[31] A. Ali, J.H. Tsai, K.L. Tung, E. Drioli and F. Macedonio, Designing and optimization of continuous direct contact membrane distillation process, Desalination. 426 (2018) 97–107.

[32] J. Phattaranawik, R. Jiraratananon and A.G. Fane, Heat transport and membrane distillation coefficients in direct contact membrane distillation, J. Memb. Sci. 212 (2003) 177–193.

[33] G. Chen, Y. Lu, X. Yang, R. Wang and A.G. Fane, Quantitative study on crystallization-induced scaling in high-concentration direct-contact membrane distillation, Ind. Eng. Chem. Res. 53 (2014) 15656–15666.

[34] M.C. García-Payo, M.A. Izquierdo-Gil and C. Fernández-Pineda, Air gap membrane distillation of aqueous alcohol solutions, J. Memb. Sci. 169 (2000) 61–80.

[35] S. Wang, M. Feng, H. Du, J.J. Weigand, Y. Zhang and X. Wang, Determination of metastable zone width, induction time and primary nucleation kinetics for cooling crystallization of sodium orthovanadate from NaOH solution, J. Cryst. Growth. 545 (2020) 125721.

[36] F. Zou, W. Zhuang, J. Wu, J. Zhou, P.P. Yang, Q. Liu, Y. Chen and H. Ying, Determination of metastable zone widths and the primary nucleation and growth mechanisms for the crystallization of disodium guanosine 5′-monophosphate from a water-ethanol system, Ind. Eng. Chem. Res. 54 (2015) 137–145.

[37] S. Karthika, T.K. Radhakrishnan and P. Kalaichelvi, Measurement of nucleation rate of ibuprofen in ionic liquid using induction time method, J. Cryst. Growth. 521 (2019) 55–59.

[38] K. Sangwal, On the interpretation of metastable zone width in anti-solvent crystallization, Cryst. Res. Technol. 45 (2010) 909–919.

[39] K. Sangwal, E. Mielniczek-Brzóska and S. Barylska, Solubility of ammonium oxalate in water-acetone mixtures and metastable zone width of their solutions, Chem. Eng. Res. Des. 92 (2014) 491–499.

[40] R. Thanedgunbaworn, R. Jiraratananon and M.H. Nguyen, Shell-side mass transfer of hollow fibre modules in osmotic distillation process, J. Memb. Sci. 290 (2007) 105–113.

[41] L. Martínez, Comparison of membrane distillation performance using different feeds, Desalination. 168 (2004) 359–365.

[42] A. Alkhudhiri, N. Darwish and N. Hilal, Membrane distillation: A comprehensive review, Desalination. 287 (2012) 2–18.

[43] J.W. Mullin, Crystal growth, in: J.W. Mullin (Ed.), Cryst. (Fourth Ed., Fourth Edi, Butterworth-Heinemann, Oxford, (2001) 216–288.

[44] G. Zeng, H. Li, S. Huang, X. Wang and J. Chen, Determination of metastable zone width and the primary nucleation kinetics of sodium sulfate, Theor. Found. Chem. Eng. 49 (2015) 869–876.

[45] F. Edwie and T.S. Chung, Development of hollow fiber membranes for water and salt recovery from highly concentrated brine via direct contact membrane distillation and crystallization, J. Memb. Sci. 421-422 (2012) 111-123.

[46] M. Lenka and D. Sarkar, Determination of metastable zone width and nucleation kinetics for combined cooling and antisolvent crystallization of L-asparagine monohydrate in water-isopropanol mixture, J. Cryst. Growth. 501 (2018) 66–73.

[47] H. Kurokawa and T. Sawa, Heat recovery characteristics of membrane distillation, Heat Transf. - Japanese Res. 25 (1996) 135–150.

[48] M. Khayet, Membranes and theoretical modeling of membrane distillation: A review, Adv. Colloid Interface Sci. 164 (2011) 56–88.

[49] W. Omar and J. Ulrich, Determination of nucleation parameters and the solid liquid interfacial energy of the KCl-ethanol-water system, Cryst. Res. Technol. 42 (2007) 432–439.

[50] X. Ni and A. Liao, Effects of cooling rate and solution concentration on solution crystallization of L-glutamic acid in an oscillatory baffled crystallizer, Cryst. Growth Des. 8 (2008) 2875–2881.

[51] S. Datta and D.J.W. Grant, Effect of supersaturation on the crystallization of phenylbutazone polymorphs, Cryst. Res. Technol. 40 (2005) 233–242.

[52] Y. Liu, T. Horseman, Z. Wang, H.A. Arafat, H. Yin, S. Lin and T. He, Negative Pressure Membrane Distillation for Excellent Gypsum Scaling Resistance and Flux Enhancement, Environ. Sci. Technol. 56 (2022) 1405–1412.

[53] J. Desarnaud, H. Derluyn, J. Carmeliet, D. Bonn and N. Shahidzadeh, Hopper Growth of Salt Crystals, J. Phys. Chem. Lett. 9 (2018) 2961–2966.

[54] X. Li, X. Song, G. Liu and J. Yu, Size-dependent nucleation and growth kinetics model for potassium chloride-Application in Qarhan salt lake, J. Cryst. Growth. 311 (2009) 3167–3173.

[55] S. Teychené and B. Biscans, Nucleation kinetics of polymorphs: Induction period and interfacial energy measurements, Cryst. Growth Des. 8 (2008) 1133–1139.

[56] T. Tong, A.F. Wallace, S. Zhao and Z. Wang, Mineral scaling in membrane desalination: Mechanisms, mitigation strategies, and feasibility of scaling-resistant membranes, J. Memb. Sci. 579 (2019) 52–69.

[57] T. Horseman, C. Su, K.S.S. Christie and S. Lin, Highly effective scaling mitigation in membrane distillation using a superhydrophobic membrane with gas purging, Environ. Sci. Technol. Lett. 6 (2019) 423–429.

[58] H. Jin, H. Athreya, S. Wang and K. Nawaz, Experimental study of crystallization fouling by calcium carbonate : Effects of surface structure and material, Desalination. 532 (2022) 115754.

[59] X. Jiang, Y. Niu, S. Du and G. He, Membrane crystallization: Engineering the crystallization via microscale interfacial technology, Chem. Eng. Res. Des. 178 (2022) 454–465.

[60] I. V. Alexandrova, A.A. Ivanov and D. V. Alexandrov, How the intermediate stage of a phase transition process transforms to the concluding stage of Ostwald ripening, J. Cryst. Growth. 532 (2020) 125456.

[61] A.E. Lewis, M.M. Seckler, H. Kramer, G. Van Rosmalen, Industrial crystallization:

Fundamentals and applications, first Edit, Cambridge University Press (2015) 104–126.

[62] A.S. Myerson, D. Erdemir and A.Y. Lee, Handbook of Industrial Crystallization, Third Edit, Cambridge University Press, (2019) 15–39.

[63] M.A. Lovette, A.R. Browning, D.W. Griffin, J.P. Sizemore, R.C. Snyder and M.F. Doherty, Crystal shape engineering, Ind. Eng. Chem. Res. 47 (2008) 9812–9833.

3 Methods to modify supersaturation rate in membrane distillation crystallisation: control of nucleation and crystal growth kinetics (including scaling)

Methods to modify supersaturation rate in membrane distillation crystallisation: control of nucleation and crystal growth kinetics (including scaling)

Ouda, Y. Bajón-Fernández, E. McAdam

Cranfield Water Science Institute, Cranfield University, UK

Corresponding author: e.mcadam@cranfield.ac.uk

Abstract

While water vapour flux is often regarded as the critical parameter in membrane distillation crystallisation (MDC), there are multiple factors that will determine the kinetics of nucleation and crystal growth. A Nývlt-like equation is therefore introduced to characterise the metastable zone that can accommodate the collective description of multiple conditional parameters (membrane area, flux, temperature differences across membrane (ΔT), crystalliser volume, magma density), enabling their independent role in modifying the kinetics of nucleation and crystal growth to be determined. Each parameter can be modified to increase supersaturation rate, which reduced induction time and broadened the metastable zone width (MSZW) at induction. An increase in supersaturation mitigated scaling, to favour bulk nucleation. This is due to the increase in volume free energy provided by the elevated supersaturation that reduces the critical energy requirement for nucleation sufficient to favour a homogeneous primary nucleation mechanism. When increasing supersaturation rate by membrane area, an identical nucleation order was identified, suggestive of a consistency in the energy requirement for the formation and growth of stable nuclei. It is therefore asserted that MDC affords an inherently scalable solution for crystallisation. An increase in temperature difference or magma density narrowed the MSZW. However, for each parameter, either supersaturation rate, supersaturation or induction time could be sustained while the other two factors changed. While higher supersaturation rates generally favour larger crystal sizes (due to Ostwald ripening) with broader size distributions, delivering a high level of supersaturation at a low supersaturation rate, increased particle size and narrowed the size distribution. This study therefore provides a framework for the effective mitigation of scaling, complemented with the discrete control over crystal growth, where the parameters identified can be collectively and synergistically applied to deliver a broad range of kinetic trajectories.

Keywords: *brine management; resource recovery; crystal growth; hollow fibre; direct contact*

3.1 Introduction

Membrane distillation offers well-defined interfacial area over which mass and heat transfer are controlled to achieve good regulation of the evaporation rate [1,2]. This can provide for the homogeneous regulation of supersaturation, which is critical for controlling the kinetics of nucleation and crystal growth in membrane distillation crystallisation (MDC) [3,4]. Mass and heat transfer mechanisms introduce temperature and concentration polarisation phenomenon within the interfacial boundary layer adjacent to the membrane [5]. It is the difference in supersaturation between the boundary layer and the bulk solution which implies that MDC may be able to decouple primary nucleation, which is thought to occur within the boundary layer, from crystal growth which dominates in the bulk solution [6,7]. The membrane is considered advantageous for crystallisation, as the contact angle can lower the energy barrier to instigate primary heterogeneous nucleation which is beneficial to solutes characterised by low supersaturation and long induction times [8]. However, the occurrence of nucleation at the membrane surface can also induce scaling which has a deleterious effect on membrane performance [9,10].

The rate at which supersaturation is achieved, will determine the extent of supersaturation at the point of nucleation [11]. The extent of supersaturation is also called the metastable limit. The area between the solubility curve and the metastable limit curve is described as the metastable zone width (MSZW) [12]. According to Sangwal [13], the MSZW is linearly related to the supersaturation rate. Consequently, a high supersaturation rate will yield a high nucleation rate. At the upper limit of the MSZW, there exists a labile region where supersaturation lowers the free energy barrier sufficiently for spontaneous primary nucleation to proceed. In principle, these conditions do not require a heterogeneous substrate to initiate nucleation (homogeneous nucleation), which could be advantageous to membrane systems as it implies the potential to limit scaling. However, high supersaturation rates can favour smaller crystal sizes with broad size distributions [5,14]. Therefore, there may exist regions within the MSZW that can foster a compromise between the nucleation kinetics which limit scaling, and crystal growth conditions that elicit favourable product characteristics. Close control of the crystal size distribution (CSD) is important as

crystal morphology, size and purity can be important for final application, while fines formation should be avoided to simplify downstream separations [6,14].

In MDC, the water vapour flux can be used to modify the supersaturation rate, therefore determining where within the MSZW that nucleation is initiated. The vapour pressure difference is fixed using the feed temperature or temperature difference across the membrane which controls the membrane flux [5,15–17]. However, an increase in temperature reduces the energy barrier for nucleation, alters the solubility curve of the solution and increases the supersaturation rate (by increasing flux). The revised mass and heat transfer characteristics also modify the extent of concentration polarisation within the interfacial boundary layer subsequently adjusting the kinetics of nucleation and crystal growth. These interdependencies make it difficult to independently characterise the specific implications of using temperature or temperature difference to initiate nucleation and growth in different regions of the MSZW. In principle, for a fixed flux, an increase in membrane area can adjust supersaturation rate while sustaining comparable boundary layer characteristics. According to the theoretical approach of Nývlt [18], the supersaturation rate is also dependent upon initial solute mass (magma density) and volume. The magma density can alter the vapour pressure but will also modify the solute concentration within the interfacial boundary layer, whereas the solution volume can be used to adjust supersaturation rate without implication to the boundary layer. In principle, solution volume can therefore be used to transition across the MSZW, and independently characterise how each of these factors individually inform on the kinetics of nucleation and crystal growth.

While the MSZW is recognised to play a critical role in controlling primary nucleation, characterisation of the MSZW has been rarely reported in the membrane crystallisation literature, requiring the accurate determination of induction time [7,19]. To date, induction time has been primarily inferred from the rapid decline in membrane flux [9,15]. However, it is widely recognised that these two phenomena are mechanistically distinct [9]. Jiang et al. [11] provided one of very few studies to relate the maximum MSZW boundary (ΔC_{max}) to the supersaturation through control of feed temperature and temperature difference (ΔT). In their study, nucleation kinetic parameters were ascertained but they were not correlated to the primary nucleation

mechanism, which determines the probability for scaling, or to crystal growth phenomena, which are also strongly informed by where within the MSZW that nucleation occurs. In this study, we intend to independently characterise each of the critical parameters that determine the supersaturation rate as a basis on which to inform control strategies for MDC that offer a deterministic approach to crystallisation. In-line turbidimetry is applied for the accurate determination of induction time as a method to systematically characterise the MSZW, thereby relating the physical environment to the kinetics of nucleation and crystal growth. Specific objectives are to: (i) characterise methods for modulating supersaturation rate in MDC by transforming data to describe primary nucleation kinetics across the MSZW; (ii) differentiate between regions in which homogeneous and heterogeneous nucleation (scaling) are likely to predominate; (iii) determine regions within the MSZW that foster specific crystal growth characteristics; and (iv) establish a framework that can collectively describe how nucleation and crystal growth can be facilitated through a broad set of kinetic trajectories.

3.2 Materials and methods

3.2.1 MDC experimental setup

Commercial polypropylene hollow fibre membranes (Accural 300/1200, 3M, Wuppertal, Germany) with a porosity of 73±2 %, pore size of 0.45 µm and wall thickness 300 µm, were used in this study (Table 3.1). The hollow fibre membranes were potted and sealed into end plates and mounted into an acrylic membrane housing with an internal diameter and length of 15mm and 150mm respectively. Two membrane modules were constructed with 7 and 37 hollow fibres comprising an effective membrane area of 59.4 cm^2 and 313.9 cm^2 respectively (Table 3.1) and operated in a direct contact membrane distillation configuration (Figure 3.1).

Table 3.1 *Membrane and module specification.*

Property	Units	Value	Fibre no.	
			7	37
Internal Diameter	(di, m)	0.0012		
Outer diameter	(do, m)	0.0018		
Wall Thickness	(m)	0.0003		
d_i/d_o	(-)	0.67		
Pore size	(μm)	0.45		
Porosity	(%)	73±2		
Contact angle[a]	(°)	131		
Fibre Length	(m)	0.15		
Shell inner diameter	(m)	0.015		
Packing density	(%)		10.2	53.9
Membrane area	(cm^2)		59.4	313.9

[a] Measured using water [29]

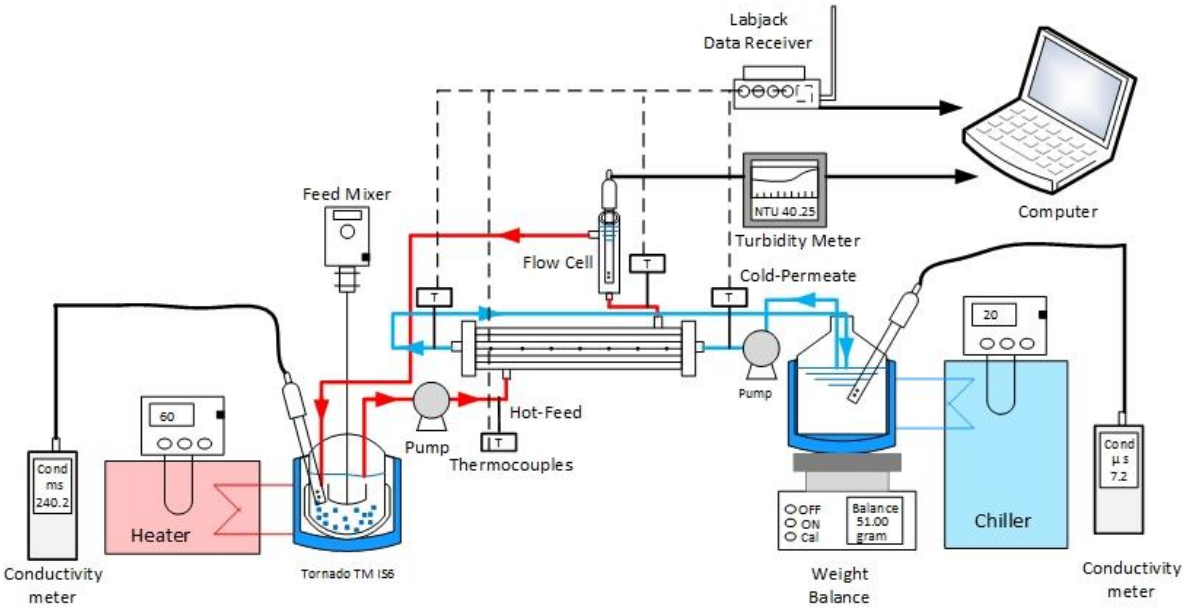

Figure 3.1 *Schematic diagram of the MDC setup.*

The feed solution (sodium chloride, 23.9 wt.% and 25.9 wt.%) was introduced into the shell-side and maintained at a temperature of 55±1°C using a heater and heat exchanger assembly (Tornado TM IS6, HUBER Ministat230; Radleys, Saffron Walden, UK). Deionised water was cooled down using a chiller (LT ECOCOOL 150, Grant Instruments, Shepreth, UK) and introduced counter current into the hollow fibre

lumen side. Feed and permeate temperatures were measured with in-line thermocouples (El1034 Temperature Prop, LabJack Corporation, Lakewood, USA). Feed and permeate velocities were fixed at 0.06 m s^{-1} and laminar flow was reliably maintained (Reynold number < 2000) for each membrane module using a peristaltic pump (Masterflex L/S Digital Pump System, Cole Parmer, St. Neots, UK), where temperature difference across the membrane was maintained at 20±2°C and 10±2°C. The permeate flux was measured experimentally using a balance (±0.5g accuracy, LBX model bench scale, Adam Equipment Co Ltd, Milton Keynes, UK). For each condition, experiments were conducted in triplicate, and the average was recorded.

3.2.2 Characterisation of nucleation, crystallisation and surface scaling

An in-line turbidity sensor was used which employs a backscatter technique to determine induction (InPro8200/S/Epoxy/120, Mettler Toledo, Manchester, UK), which comprises of a dual optic fibre construction to provide greater sensitivity for nucleation detection. The produced crystals were collected by filtering feed solution through a 0.45 µm nylon filter (Whatman, Dorset, UK). The crystals were dried over a desiccant (Genlabs drying cabinets 200L, Zoro, London, UK) for 48 hours (temperature ~23°C) before weighing with a high precision balance (range 0.02 to 62g, error ±0.0001g, Fisherbrand™, Loughborough, UK). Crystal size distributions were performed using optical microscopy (Lumenera Infinity 3-3 Camera with lens, 5/0.12 160/-) and images analysed using Image ProPremier software (v9.2, Media Cybernetics, Rockville, US). CSD was determined for each set of experimental conditions and comprised a minimum of 800 crystals to minimise the standard error of the distribution. The coefficient of variation (CV) was calculated according to the following equation [7]:

$$CV = \frac{L_{84\%} - L_{16\%}}{2\,L_{50\%}} \quad \textbf{(3-1)}$$

The membrane module was collected after the experiment and dried over desiccant for 72 hours, before being weighed. Membrane scaling/deposition was expressed as crystal weight per membrane area (g m^{-2}). All experiments were conducted in triplicate as a minimum, and the average reported.

3.2.3 Data analysis

The Permeate flux (N) (kg m^{-1} h^{-1}) was calculated as follows [18]:

$$N = \frac{m}{A \times \Delta t} \quad \textbf{(3-2)}$$

where m is the permeate mass (kg), A is membrane area (m^2), and Δt represents the time interval (h). The bulk feed solute concentration was estimated based on a permeate flux mass balance, while using direct monitoring of permeate conductivity to confirm the permeate solute concentration. In the membrane boundary layer, the film concentration C_{fm} deviates from that of the bulk feed solution, C_f, due to concentration polarisation (CPC), which was calculated based on the film mode [21]:

$$CPC = \frac{c_{fm}}{c_f} = exp\left(\frac{N}{\rho \times k_s}\right) \quad \textbf{(3-3)}$$

where C_{fm} and C_f (g NaCl. g^{-1} solution) are the membrane film concentration and bulk feed concentration respectively, ρ is solution density (kg m^{-3}) and k_s is the solute mass transfer coefficient (m s^{-1}) which can be evaluated from Chilton-Colburn analogy [22,23]:

$$\frac{Sh_f}{Sc_f^{0.33}} = \frac{Nu_f}{Pr_f^{0.33}} \quad \textbf{(3-4)}$$

where Sh_f is the Sherwood number, Sc is the Schmidt number, Nu_f is the Nusselt number and Pr_f is the Prandtl number of feed solution.

$$Sh_f = \frac{k_s D_h}{D_s} \quad \textbf{(3-5)}$$

$$Sc_f = \frac{\mu_f}{P_f D_s} \quad \textbf{(3-6)}$$

$$Nu_f = 1.86(Re\,\mathrm{Pr}\,{}^{D_h}/_{L})^{0.33} \quad \textbf{(3-7)}$$

$$Re = \frac{d_h V \rho}{\mu} \quad \textbf{(3-8)}$$

$$Pr_f = \frac{C_p \mu}{k_s} \quad \textbf{(3-9)}$$

where Re is Reynold number (-), D_h is hydraulic diameter (m), D_s is solute diffusion coefficient (m^2 s^{-1}), μ is viscosity (Pa s^{-1}), L is the hollow fibre length (m), v is the feed velocity (m s^{-1}). The heat transfer in membrane distillation consists of the latent heat Q_v (W m^{-2}) from the vapour flux, and conductive heat through the membrane Q_c (W m^{-2}) [20]:

$$Q = Q_v + Q_c = \left(\frac{k_m}{\delta_m}\right)\left(T_{fm} - T_{pm}\right) + NH_{V,T} \quad \textbf{(3-10)}$$

$$H_{V,T} = 1.7535\,\mathrm{T} + 2024.3 \quad \textbf{(3-11)}$$

where $H_{V,T}$ is vapour latent heat (kJ kg^{-1}), k_m is membrane thermal conductivity (W m^{-1} K^{-1}) and δ_m is the membrane thickness (m) [24]:

$$k_m = k_p(1-\varepsilon) + k_g\varepsilon \quad \textbf{(3-12)}$$

where k_p (W m^{-1} K^{-1}), and k_g (W m^{-1} K^{-1}) are the polymer thermal conductivity and the air thermal conductivity respectively, while Ɛ is membrane porosity and T is the average temperature at the membrane surface (K) [24,25]:

$$\mathrm{T} = \frac{T_{fm}+T_{pm}}{2} \quad \textbf{(3-13)}$$

T_{fm} and T_{pm} are the feed and permeate temperature at the membrane vicinity [15,20]:

$$T_{fm} = T_f - \left(T_f - T_p\right)\left[\frac{1/h_f \times d_i/d_o}{1/h_f \times d_i/d_o + 1/(h_m+h_v) + 1/h_p}\right] \quad \textbf{(3-14)}$$

$$T_{pm} = T_p - \left(T_f - T_p\right)\left[\frac{1/h_p}{1/h_f \times d_i/d_o + 1/(h_m+h_v) + 1/h_p}\right] \quad \textbf{(3-15)}$$

where T_f and T_p (k) are the bulk temperature in feed and permeate, $d_i/d_\circ$ is inner/outer diameter ratio, $h_m = k_m/\delta_m$ (W m^{-2} K^{-1}) is membrane heat transfer coefficient, and h_v is the vapour heat transfer coefficient (W m^{-2} K^{-1}):

$$h_v = \frac{NH_{v,(T_{fm}+T_{pm})/2}}{(T_{fm}-T_{pm})} \quad \textbf{(3-16)}$$

where h_f (W m^{-2} K^{-1}) is feed heat transfer coefficient and h_p (W m^{-2} K^{-1}) is the permeate heat transfer coefficient:

$$h_{f,p} = Nu \times \frac{k_{f,p}}{d_{h_{f,p}}} \quad \textbf{(3-17)}$$

where k_f (W m^{-1} K^{-1}) is the thermal conductivity of feed and k_p (W m^{-1} K^{-1}) is the thermal conductivity of the permeate, d_{hf} and d_{hp} are the hydraulic diameter of feed and permeate flow channel and Nu is the Nusselt's number. Therefore, the temperature polarisation coefficient was calculated by iteration from the heat transfer relationship:

$$TPC = \frac{T_{fm}-T_{pm}}{T_f-T_p} \quad \textbf{(3-18)}$$

The nucleation mechanism was analysed based on classic nucleation theory where the change in critical free energy ΔG* can be expressed as follows [26]:

$$\Delta \mathrm{G} * = \frac{16\pi v_\circ^2 \gamma^3}{3(k_B T)^2 ln^2 s} \quad \textbf{(3-19)}$$

where ΔG* is the critical nucleation barrier at a given supersaturation, k_B is the Boltzmann constant (1.38 x 10^{-23} J K^{-1}), T is the nucleation temperature (K), S is

supersaturation (C/C*, unitless) and γ is interfacial energy (mJ m^{-2}). The molar volume (v_0, m_3) is:

$$v_0 = \frac{M}{\rho N_a} \quad \textbf{(3-20)}$$

v_o is the molar volume (m^3), ρ_{cry} is crystal density (kg m^{-3}), N_a is Avogadro's number (6.022 x 10^{23} molecules mol^{-1}). According to Arrhenius's approach, the nucleation rate J (No. m^{-3} s^{-1}) is given as follows [27]:

$$\mathrm{J} = A \exp\left(-\frac{\Delta \mathrm{G}*}{K\,T}\right) = A \exp\left(-\frac{16\pi v_{\circ}^2 \gamma^3}{3(k_B T)^3 ln^2 s}\right) \quad \textbf{(3-21)}$$

The nucleation rate is related inversely to induction time which can be related to the extent of supersaturation [28]:

$$t_{ind} \propto \frac{1}{J} \quad \textbf{(3-22)}$$

$$\ln t_{ind} = \ln A + \left(\frac{16\pi v_{\circ}^2 \gamma^3}{3(k_B T)^3 ln^2 s}\right) = \ln A + \left(\frac{B}{ln^2 s}\right) \quad \textbf{(3-23)}$$

where A (m^{-3} s^{-1}) is the pre-exponential kinetic parameter, B is the thermodynamic parameter for nucleation [29]. Linearisation of the relationship between $\ln(t_{ind})$ and $1/(\ln^2 S)$, yields lnA as the intercept and B as the gradient, enabling calculation of critically dependent crystallisation parameters, where the dominant nucleation mechanism (homogenous or heterogenous) can be evidenced from the gradient of the obtained slope.

The MSZW was analysed by adaption of the approach proposed by Nyvlt [18], where the maximum MSZW limit identified at the membrane surface $\Delta C_{max.fm}$ (mg. g^{-1} solution) is assumed to be proportional to the concentrating rate R' (g .100g solution .h^{-1}) [11];

$$\Delta \mathrm{C} = \left(\frac{\mathrm{dC}}{\mathrm{dT}}\right)_T R' \quad \textbf{(3-24)}$$

$$R' = \left(\frac{\mathrm{dCo}}{\mathrm{dt}}\right)_t = \frac{F_p\, C_0}{m_0 - \int_0^t F_P d\tau} \quad \textbf{(3-25)}$$

where F_p is permeate flow rate (kg h^{-1}), m_o is feed solution mass (kg), C_o is the equilibrium concentration (g NaCl. g^{-1} solution). By assuming that the supersaturation rate is equal to nucleation rate at induction, the relationship between nucleation rate (J) and the maximum MSZW limit at the membrane surface $\Delta C_{max.fm}$ was expressed by an empirical power-law relationship [11,12]:

$$\mathrm{J} = \mathrm{k}(\Delta \mathrm{C}_{\mathrm{max,fm}})^{\mathrm{n}} \quad \textbf{(3-26)}$$

where $\Delta C_{max,fm}$, (which is, c_{fm}-c*) is the maximum supersaturation within the membrane boundary layer. Therefore, the maximum supersaturation boundary at the membrane film $\Delta C_{max,fm}$ is proposed to be proportional to the concentrating rate R', where both correspond to the nucleation rate:

$$J = k(\Delta C_{max,fm})^n = \left(\frac{dc_0}{dt}\right)_t = \frac{F_p C_0}{m_0 - \int_0^t F_P d\tau} \quad \textbf{(3-27)}$$

Taking logarithms for both sides of eq. (26), the nucleation constant (k) and nucleation order can be determined from a linear fit between lnR' and ln $\Delta C_{max,fm}$:

$$\ln(\Delta C_{max,fm}) = \frac{1}{n}\ln\left(\frac{C_0}{k}\right) + \frac{1}{n}\ln\left(\frac{F_p}{m_0 - \int_0^t F_P d\tau}\right) \quad \textbf{(3-28)}$$

3.3 Result and discussion

3.3.1 Characterising flux and induction time to transform into supersaturation rate

The individual parameters that collectively determine the supersaturation rate in MDC were independently examined (membrane area, magma density, temperature difference). For each parameter, solution volume was used to transition across the MSZW. An increase in solution volume does not alter mass and heat transfer conditions across the membrane, enabling consistent boundary layer conditions when transitioning across the MSZW. Consequently, the water vapour flux established for each individual parameter was comparable across the solution volumes tested (Figure 3.2). However, there were differences in the fluxes attained for each parameter (Table 3.2). When ΔT was decreased from 20 to 10°C in the 37 HF module, flux reduced from 2.72±0.19 to 1.0±0.11 kg m^{-2} h^{-1}, due to the reduction in vapour pressure difference which is the driving force for permeation [5]. This reduced temperature and concentration polarisation within the boundary layer. The flux attained for the 7 and 37 HF modules (ΔT 20°C, 23.9 wt.%) were similar at 3.20±0.19 and 2.72±0.19 kg m^{-2} h^{-1} respectively. The reduction in flux for the 37 HF module may have arisen from the preferential flow patterns within the larger fibre bundle which are noted to lower superficial velocity [30]. This slightly reduced the CPC and TPC within the film due to the lower mass and heat transfer [31–33]. Increasing magma density from 23.9 to 25.9 wt.% reduced the flux from 2.72±0.19 to 2.31±0.12 kg m^{-2} h^{-1} due to modification of the vapour pressure [34–36]. The reduction in flux compensated for the increased solute concentration leading to an equivalent CPC and TPC.

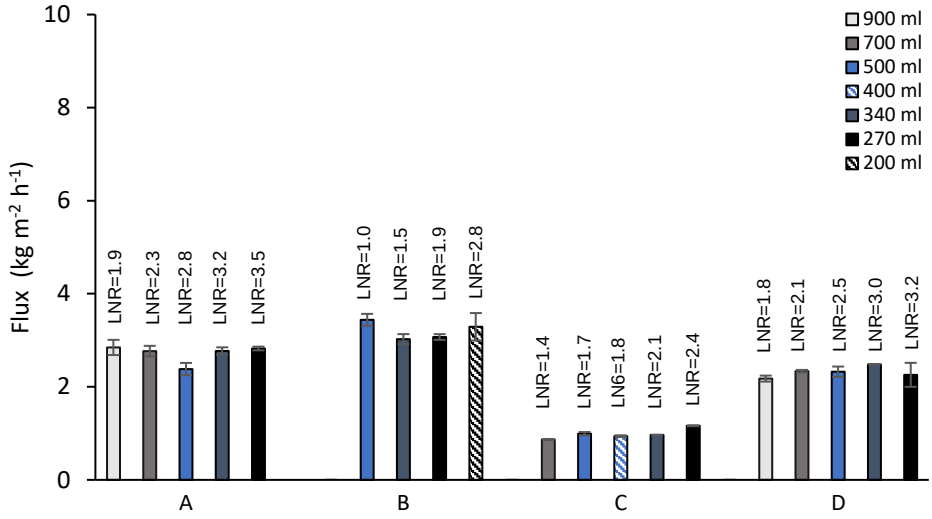

Figure 3.2 *Average permeation flux before induction and supersaturation rate for different primary supersaturation parameters: (A) 37HF, 23.92%wt, ∆T 20±2°C; (B) 7HF, 23.92%wt, ∆T 20±2°C; (C) 37HF, 23.92%wt, ∆T 10±2°C; (D): 37HF, 25.92%wt,∆T= 20°±2C. Boundary conditions: Tbulk,55 ±1°C; feed and permeate velocity, 0.06 m* s^{-1}.

Table 3.2 Average concentration and temperature polarisation before induction for different supersaturation parameters.

Fibre no.	Bulk temperature (°C)	Temperature differences ∆T (°C)	Initial feed concentration (wt. %)	Concentration polarisation (CPC)	Temperature polarisation (TPC)
7HF	55±1	20±2	23.9	1.054±0.01	0.55±0.03
37HF	55±1	20±2	23.9	1.025±0.004	0.59±0.01
37HF	55±1	10±2	23.9	1.010±0.001	0.69±0.01
37HF	55±1	20±2	25.9	1.025±0.01	0.60±0.01

For each parameter, a steady-state period of flux was followed by a rapid decline in flux with every volume tested (Figure 3.3). The steady-state period is defined by a slow and slight decrease in flux due to the reduction in vapour pressure which was in proportion to the progressive increase in feed concentration following permeation [37]. The rapid decline in flux has traditionally been thought to signify the onset of nucleation [19]. An increase in feed volume increased the time before the rapid flux decline began. To illustrate, the time required to the onset of rapid flux decline reduced from 100 minutes at 900ml to 46 minutes at 270ml for the 37 HF membrane module (∆T, 20°C; magma density, 23.9%wt.). Reconstruction of the data based on

supersaturation, revealed that the highest supersaturation was achieved for the smallest volume, which corresponded to the shortest filtration time.

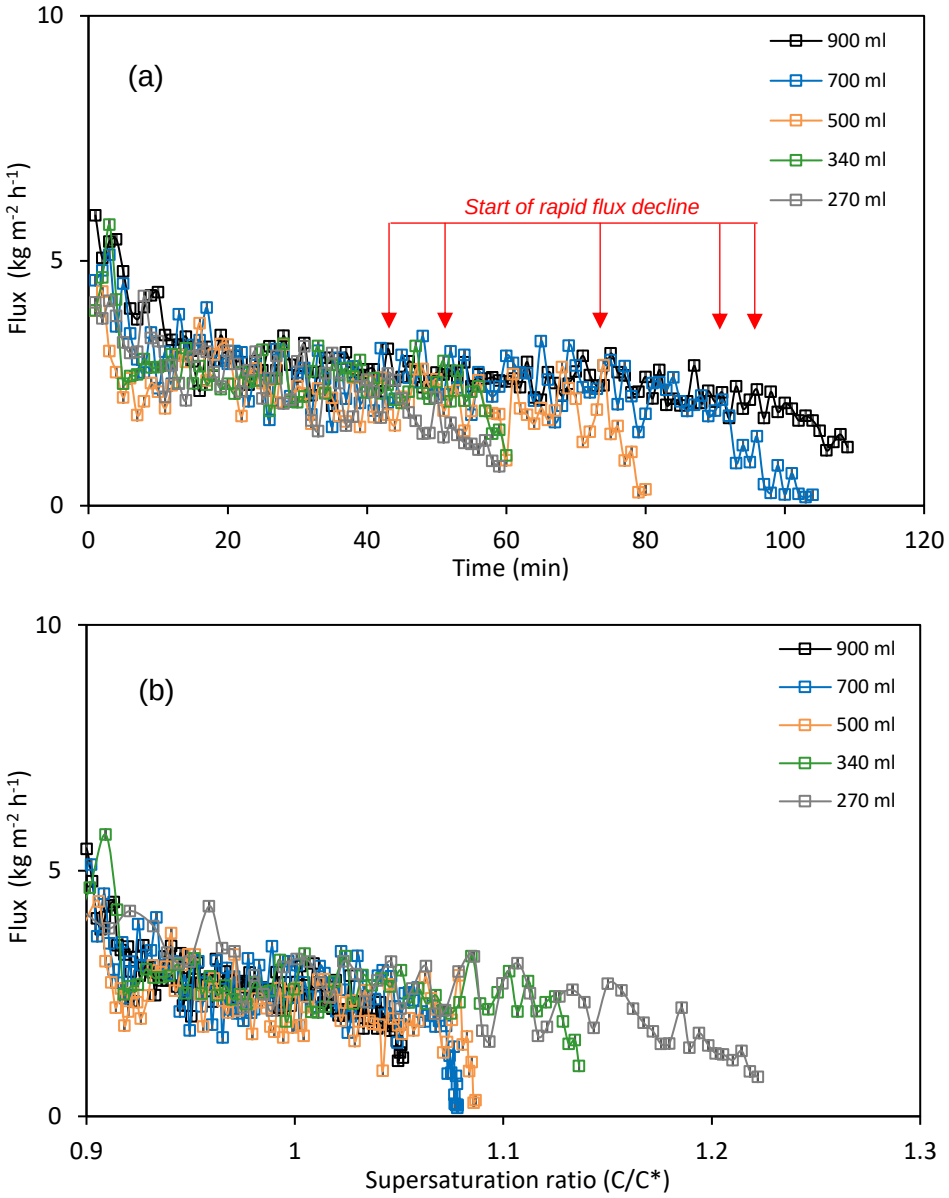

Figure 3.3 *Permeation flux for 37 HF module across the solution volumes tested. Boundary conditions: T_{bulk}, 55±1°C; ΔT membrane, 20±2°C; feed and permeate velocity, 0.06 m s^{-1}; initial feed concentration 23.9wt.% NaCl. Standard error of permeation flux was calculated based on differences in triplicate measurements for each volume; 900 ml, 2.85±0.16; 700 ml, 2.76±0.11; 500 ml, 2.83±0.13; 340 ml, 2.77±0.07; 270 ml, 2.82±0.04.*

Turbidimetry provided a more accurate quantitation of the onset of nucleation (induction) by determining the time at which crystallisation began in the bulk solution (Figure 3.4). The time between the solubility limit (c/c*, 1) and the obvious change in

turbidity is defined as the induction period, and confirmed that primary nucleation occurred in each condition tested [38]. Induction time for the 37HF module decreased from 33 min for 900ml to 22 min for 270 ml, while the supersaturation at induction increased from 1.04 to 1.16 respectively. The supersaturation levels determined through the flux curves were 1.05 and 1.17 respectively, which indicate a short lag between bulk crystallisation and the diminution of flux, which implies that this may primarily relate to the deposition of crystals formed through a homogeneous mechanism [9]. Importantly, the inverse relationship established between induction time and supersaturation is a characteristic response for kinetically controlled crystallisation [38–40]. Comparable analyses were also conducted for changes to membrane area, magma density and ΔT to distinguish the extent to which they influence primary nucleation through modification of supersaturation and induction time (primary data for all parameters within Appendix A).

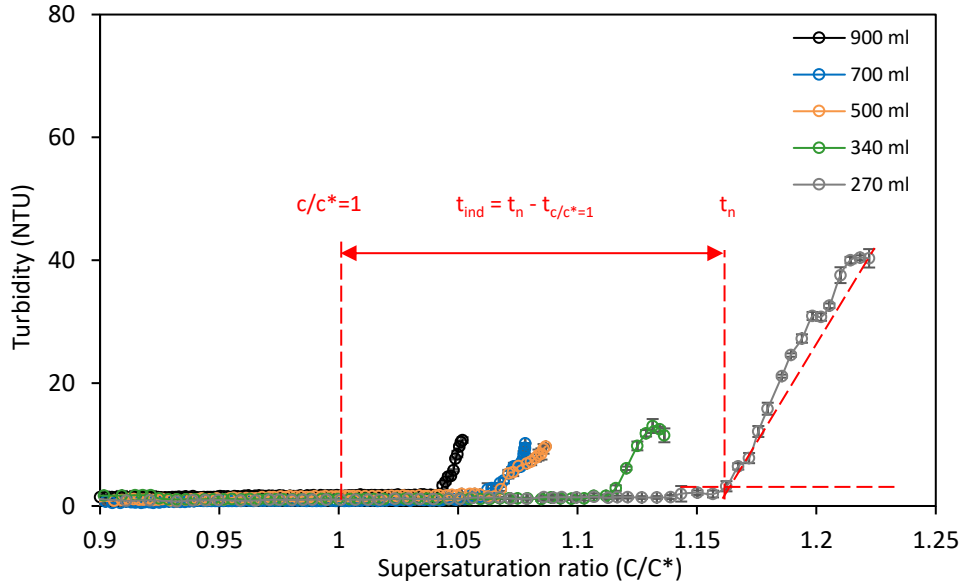

Figure 3.4 *Turbidity profile for the 37 HF module operation. The supersaturation data reported is based on bulk conditions at different supersaturation rates across the solution volumes tested. Boundary conditions: T_{bulk},55±1°C; ΔT membrane, 20±2°C; feed and permeate velocity, 0.06 m s^{-1}; initial feed concentration 23.9wt.% NaCl.*

3.3.2 Supersaturation rate sets the position for nucleation within the metastable zone

The extent of supersaturation achieved within the bulk solution and within the membrane film at induction was determined across the MSZW following an increase in membrane area. For both membrane modules (37 and 7HF modules), the

supersaturation achieved at induction within the boundary layer and bulk solution were demonstrated to increase when higher supersaturation rates (LnR', g $100g^{-1}$ solution h^{-1}) were instigated by a reduction in feed volume (Figure 3.5). This response was observed for each parameter and is consistent with the kinetically derived model of Nývlt (Eq. 26) which proposes higher supersaturation rates can be achieved for smaller crystalliser volumes [41–43]. For each membrane, the film concentration achieved at induction was consistently higher than the bulk concentration due to concentration and temperature polarisation [11,15]. The ratio between bulk and film supersaturation levels achieved at induction were broadly consistent when the concentrating rate was increased, confirming that the boundary layer was not modified when using volume to regulate transition across the MSZW (Figure 3.5a).

However, broader MSZW were achieved at induction when applying a higher area to volume ratio (A/V_o) (Figure 3.5b). For an initial volume of 270 ml, magma densities of 28.9 and 31.3 wt.% were determined for the 7 and 37HF membrane (A/V_o 21.9 and 116.2 m^2 m^{-3}) respectively. The broader MSZW is attributed to the higher concentrating rate achieved with 37HF [11,42], which is consistent with the characterisation approach of Sangwal [13] that assumes a linear correlation between concentrating rate and MSZW [13,44] (Figure 3.5c). This is evidenced through the explicit characterisation of the MSZW. For the 37 HF membrane, the maximum metastable limit ($\Delta C_{max,fm}$) increased from 2.99 mg_{solute} $g_{solution}^{-1}$ to 3.83 mg_{solute} $g_{solution}^{-1}$ when concentrating rate (LnR') increased from 1.93 g $100g^{-1}$ solution h^{-1} to 3.53 g $100g^{-1}$ solution h^{-1}. Widening of the MSZW increases the driving force for nucleation by reducing the critical free energy barrier for nucleation [11,23,44]. Elevated supersaturation develops within a kinetically controlled region (determined by the concentrating rate) of the MSZW that is seeking to establish the nearest metastable form (kinetically controlled), becoming less dependent on a heterogeneous substrate to initiate nucleation as ΔC_{fm} proceeds toward the outer metastable limit [14,45]. Importantly, both membranes exhibited comparable gradients for each slope (Figure 3.5c), which describes the apparent nucleation order (Table 3.3), from which it can be inferred that the mechanism for formation and growth of stable nuclei is analogous regardless of the membrane area used [41]. This implies nucleation to be deterministic

at this scale and provides evidence of the continuity in kinetics that may be achieved in the scale-up of membrane crystallisation systems.

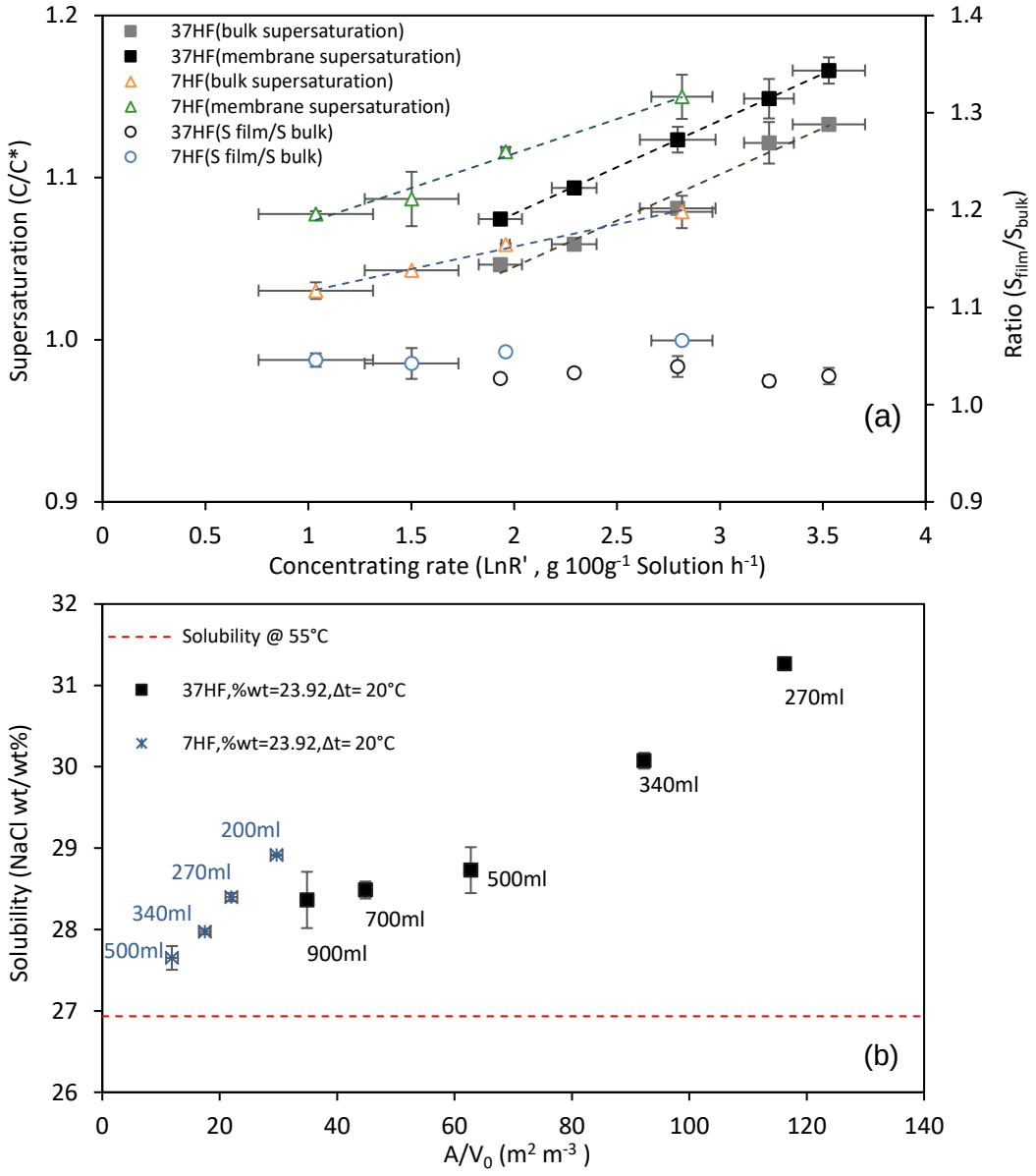

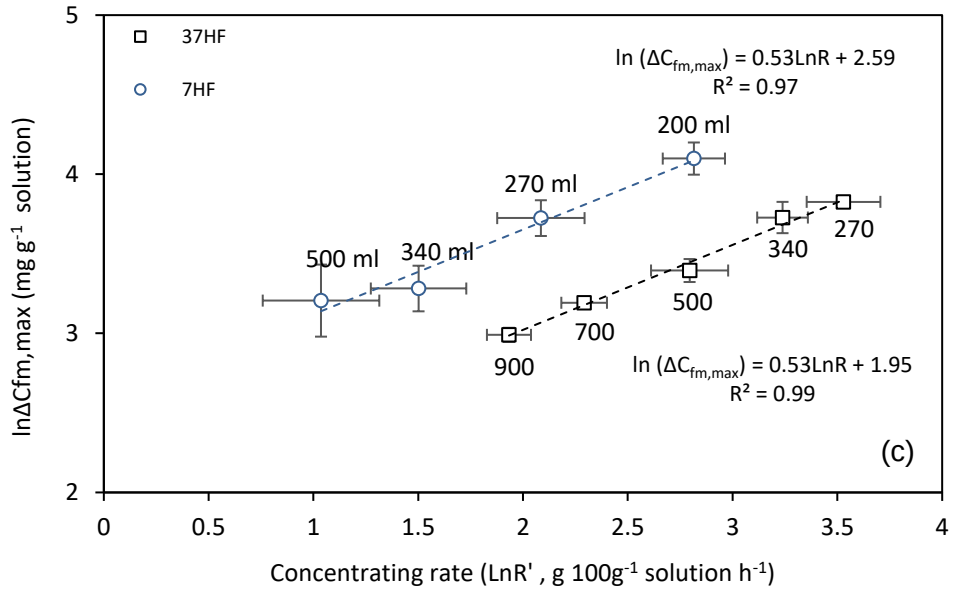

Figure 3.5 *(a) Bulk and membrane film supersaturation at induction based on concentrating rate (LnR') adjusted by membrane area; (b) Metastable region characterised following the increase in area to volume ratio (A/V_o); (c) dependence of $\Delta c_{fm,max}$ in the film on concentrating rate (LnR') according to eq.27. Boundary conditions: T_{bulk},55±1°C; ΔT20±2°C; feed and permeate velocity, 0.06 m s^{-1}; initial feed concentration 23.9 wt.% NaCl.*

The concentrating rate decreased when ΔT was reduced from 20±2 to 10±2°C due to the decline in vapour pressure gradient which lowered the driving force for permeation (N from 2.7 to 0.9 kg m^{-2} h^{-1}) [15] (Figure 3.6). This mitigated temperature and concentration polarisation in the film which adjusted the solubility curve and metastable limit curve [4,19]. Consequently, a maximum metastable limit ($LnC_{fm,max}$) of 3.14 mg g^{-1} was achieved at ΔT 10°C (270ml) compared to 3.83 mg g^{-1} for ΔT 20°C (270ml) due to the reduction in supersaturation rate. The decrease in temperature difference reduced the nucleation order, suggesting that nucleation is favoured at a higher concentrating rate (higher ΔT), where intense intermolecular collisions allow a large proportion of molecules to rapidly overcome the free energy barrier and form a stable critical nucleus [12]. Increasing magma density from 23.9 to 25.9 wt.% narrowed the MSZW due to the decrease in permeation flux imposed by the lower water activity (Figures 3.2 and 3.6) [33]. The reduced flux (Figure 3.2) decreased the concentrating rate and therefore the supersaturation level that was reached within the crystallising solution at induction, providing less driving force to initiate nucleation. While temperature and concentration polarisation were relatively comparable [46], the

reduction in mass transfer imposed by the higher magma density modified nucleation kinetics. Consequently, less broadening of the MSZW was also observed following an increase in concentrating rate, which was complemented by a reduction in the gradient of the slope. This yielded a higher nucleation order at a reduced concentrating rate, which can be attributed to the higher probability for collision between solute molecules once magma density is increased [47,48].

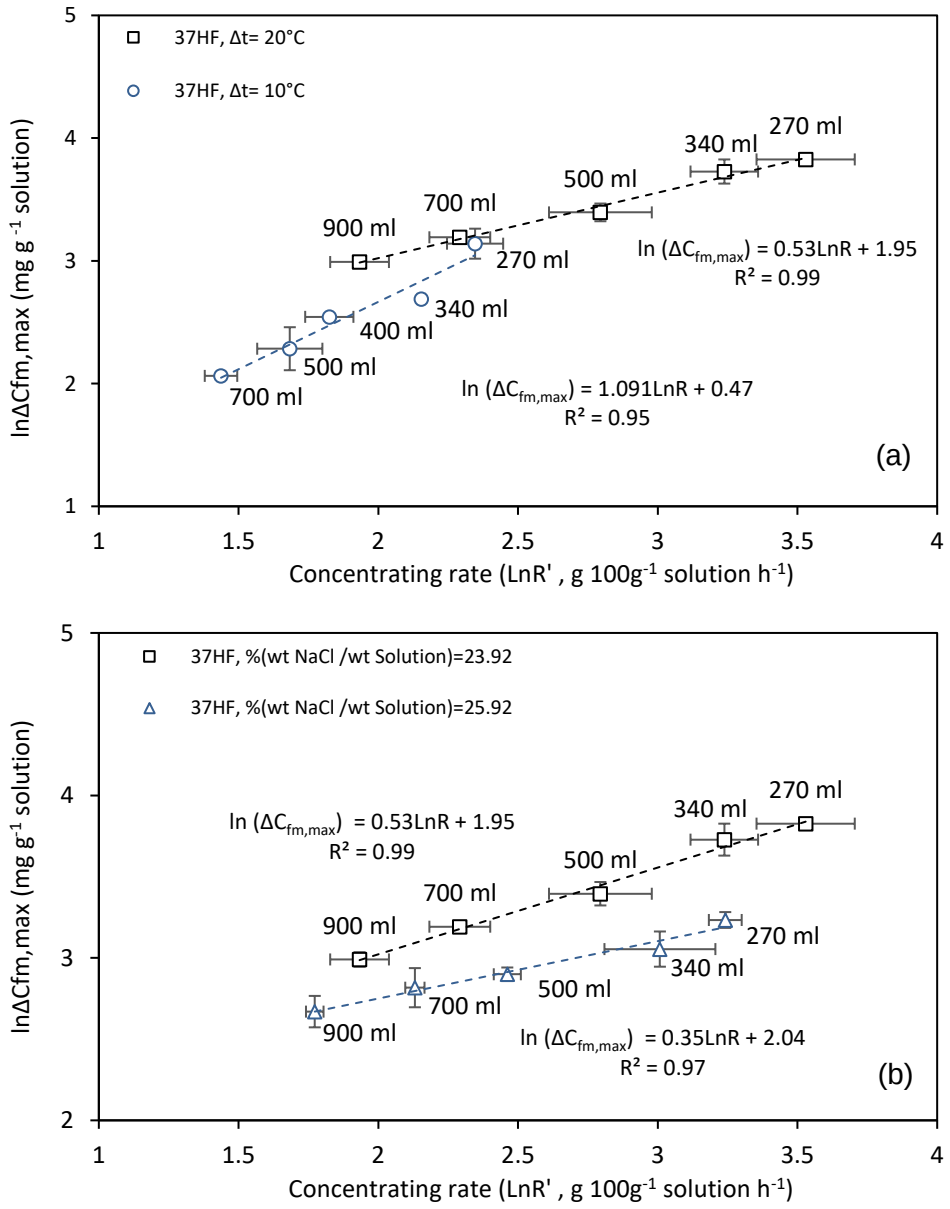

Figure 3.6 *The dependence of $\Delta c_{max,fm}$ in the membrane film on concentrating rate (LnR') for two sets of supersaturation rate parameters: (a) ΔT; and (b) different initial feed concentrations. Boundary conditions: T_{bulk}, 55±1°C; feed and permeate velocity, 0.06 m s^{-1}.*

3.3.3 Supersaturation rate determines extent of membrane scaling in MDC

Characterisation of the correlation between induction time (t_{ind}) and supersaturation (ln^2S) evidences a transition between two slopes comprising distinct gradients, where the steeper slope formed at higher supersaturation is indicative of a homogeneous primary nucleation mechanism, while the shallow slope formed at low supersaturation implies that induction is regulated via a heterogenous primary nucleation mechanism [40,45] (Figure 3.7).

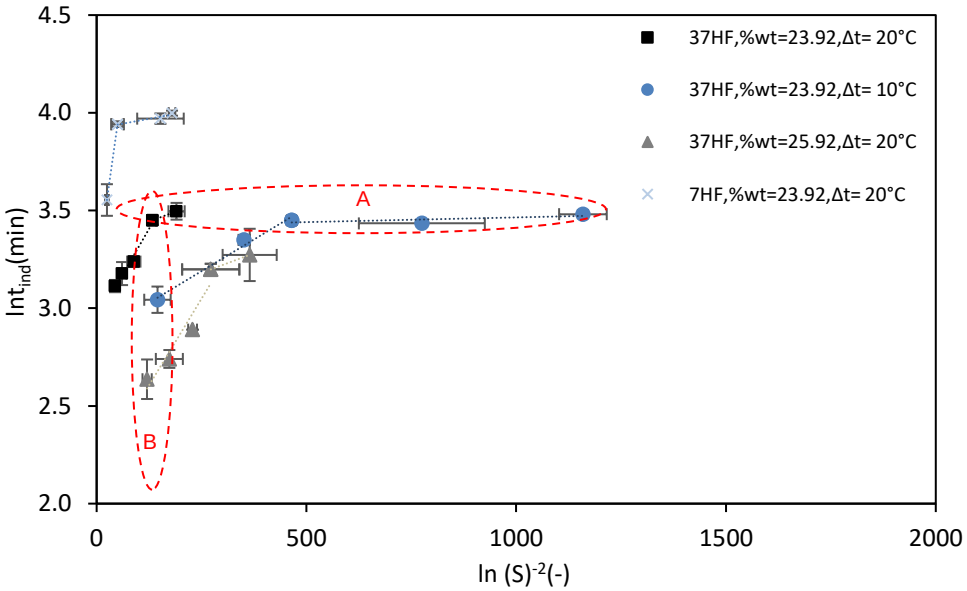

Figure 3.7 *Characterisation of induction time ($ln(_{tind})$) and supersaturation ($1/ln^2S$) at induction for different supersaturation parameters. Two distinct slopes are determined with the shallow slop infers a region dominated by primary heterogenous nucleation, while the steeper slope is characterised by a primary homogeneous nucleation mechanism at higher supersaturation. Boundary conditions: T_{bulk}, 55±1°C; feed and permeate velocity, 0.06 m s^{-1}.*

Table 3.3 *Analysis of nucleation parameters (based on correlation of ln (tind) versus 1/ln2S according to classical nucleation theory.*

Fibre no.	Bulk temperature (°C)	Temperature differences ΔT (°C)	Initial feed concentration (wt. %)	Nucleation Order (n)	Nucleation constant (k)	Initial volume (ml)	Nucleation	Intercept (K)	Slope (m)	S (C/C*)	R^2
37HF	55±1	20±2	23.9	1.88	0.16	270-500	Homogeneous	3.00	0.0027	1.12-1.17	0.98
						700-900	Heterogeneous	3.34	0.0008	1.07-1.09	1.00
37HF	55±1	10±2	23.9	0.91	4.13	270-340	Homogeneous	2.87	0.0013	1.06-1.09	0.99
						400-700	Heterogeneous	3.42	0.0001	1.03-1.05	1.00
37HF	55±1	20±2	25.9	2.83	0.02	270-500	Homogeneous	2.16	0.0035	1.07-1.10	0.91
						700-900	Heterogeneous	2.98	0.0008	1.05-1.06	1.00
7HF	55±1	20±2	23.9	1.87	0.05	200-270	Homogeneous	3.18	0.0153	1.16-1.23	1.00
						340-500	Heterogeneous	3.92	0.0004	1.08-1.09	0.93

For each parameter that was characterised, a transition from heterogeneous to homogeneous primary nucleation was illustrated as supersaturation was increased through an increase in concentrating rate. The gradient of each distinct region of supersaturation can be used to infer the interfacial energy requirement to create a thermodynamically stable nucleus [39] (Table 3.3). While the reduction in ΔT from 20 to 10°C reduced the supersaturation rate, comparable induction times were achieved within the lower region of the MSZW corresponding to where heterogeneous primary nucleation is most likely to proceed (Figure 3.7, region marked A) [1,14,40,49]. This implies that the energy barrier for nucleation was independent of the supersaturation level at induction and may be more dependent upon the role of the membrane in reducing the surface free energy required to pass the critical free energy barrier of nucleation [9,40,50]. This is supported by the corresponding scaling rates, which were comparable within the heterogeneous region of the MSZW, despite differences in concentrating rate (Figure 3.8). However, once transitioned into the homogeneous region of the MSZW, the gradient of the curve for ΔT 20°C was around two times higher than for ΔT 10°C, where the higher supersaturation levels achieved at shorter induction times foster considerably higher nucleation kinetics and mitigated scaling [9,45]. To achieve the same supersaturation at induction ($\ln S^{-2}$, ~173), each parameter required a different induction time dependent on the concentrating rate applied (Figure 3.7, region marked B). For higher concentrating rates, induction was determined within the homogeneous region of the MSZW and the membrane was characterised by negligible scaling, whereas longer induction times were synonymous with the heterogeneous region of the MSZW where substantive scaling occurred (Figure 3.8). This increased dependency on an extrinsic heterogeneous substrate that can modify the critical free energy barrier at low supersaturation levels, requiring extended induction times, is compatible with classical nucleation theory [7,8,45]. Importantly, for each of the parameters outlined that regulate supersaturation, an increase in concentrating rate is evidenced to reduce the absolute scaling rate, despite a higher crystal yield (by mass) being produced within an elevated region of

supersaturation (Figure 3.8b). This provides corroborative data to suggest that the scaling mitigation observed was due to the suppression of scaling formed through an adhesive growth mechanism (heterogeneous nucleation) rather than a reduction in deposition by crystals formed in bulk solution following formation via homogeneous nucleation [2,9,51].

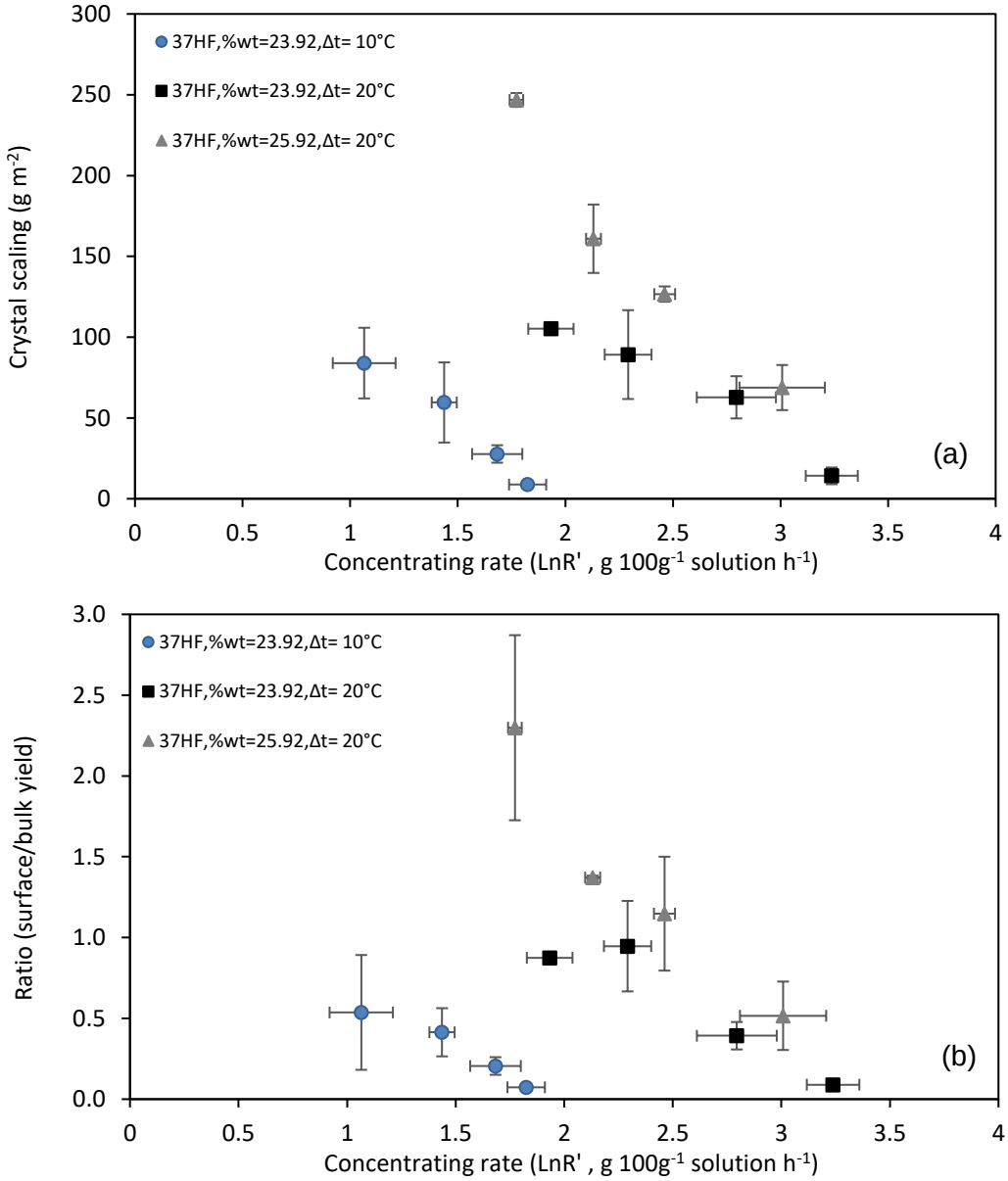

Figure 3.8 *Extent of membrane scaling: (a) 37 HF module using different supersaturation parameters; and (b) comparison of crystal mass recovered from the bulk solution and from the membrane surface when using different supersaturation parameters. Boundary conditions: T_{bulk}, 55±1°C; feed and permeate velocity, 0.06 m s^{-1}.*

3.3.4 Crystal growth is defined by the MSZW and supersaturation rate

The kinetics of crystal growth inform the size and variance of the final product and are dependent upon where within the MSZW primary nucleation occurs [40,52]. Each of the parameters studied enable kinetic adjustment by uniquely modifying supersaturation at induction, the supersaturation rate and induction time to different extents. Crystal size distributions were therefore compared to determine how each parameter independently sets conditions for growth and were benchmarked using a fixed crystalliser volume (270ml), which primarily corresponded to conditions that indicate favouring a homogeneous primary nucleation mechanism (Figure 3.9).

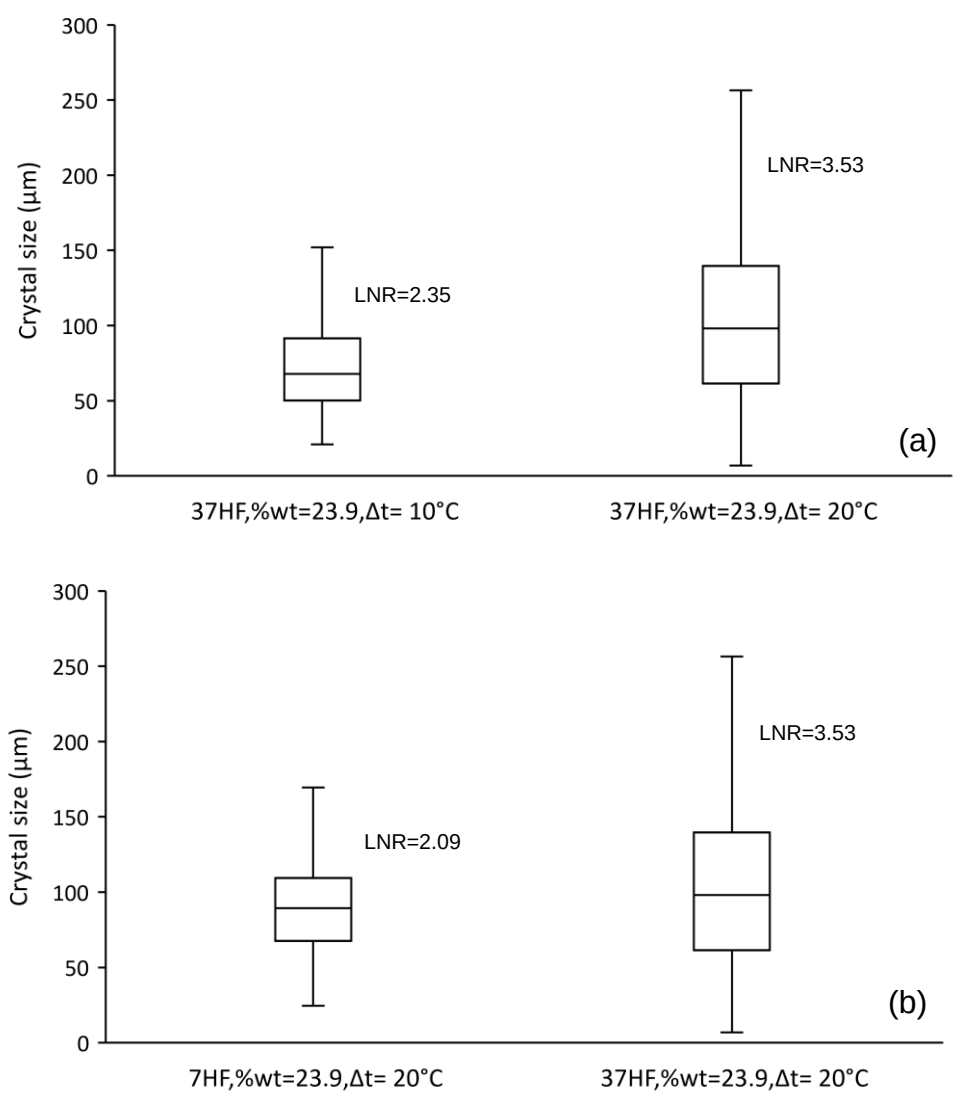

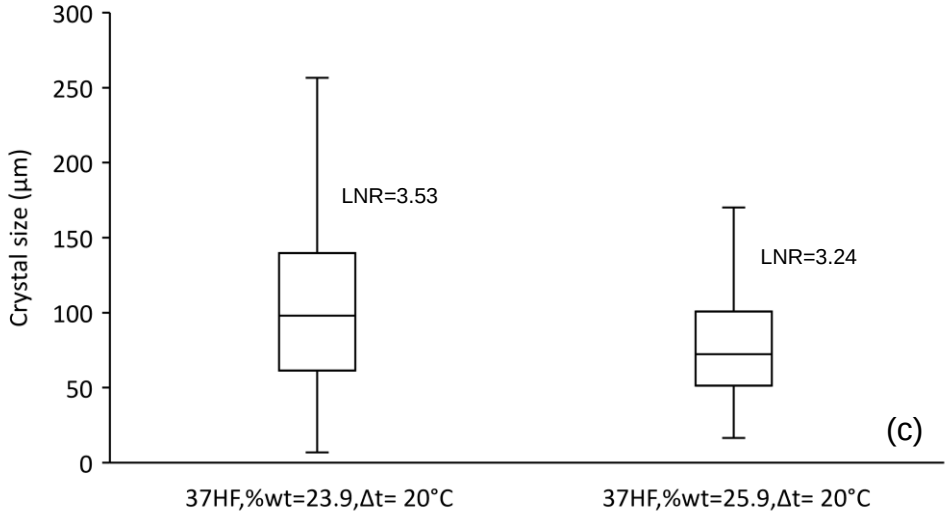

Figure 3.9 *Crystal size distributions presented as box-whisker plots: (a) ∆T; (b) membrane area; and (c); different initial concentrations. Each parameter provides adjustment of one principal component of either supersaturation rate, supersaturation or induction time. Box represents upper and lower quartiles (25th and 75th percentiles), median size is indicted by the line within the box, and the whiskers represent the limited of the size distribution (0th and 100th percentiles). Boundary conditions: T_{bulk}, 55±1°C; feed and permeate velocity, 0.06 m s^{-1}; initial feed solution volume, 270ml.*

An increase in ∆T from 10 to 20°C raised supersaturation rate to achieve a broader MSZW width at induction but at a comparable induction time (Lnt_{ind} 3.04 and 3.11 min). Median crystal size (L_{50}) increased from 69±2 to 98±4 µm and broadened the crystal size distribution (0th and 100th percentiles represented by whiskers). According to classical nucleation theory, an elevated concentrating rate should instigate higher nucleation rates that tend to produce a greater number of smaller crystals [39,45,53]. This contradicts findings in this study and can be explained by Ostwald's ripening which is recognised to occur at elevated supersaturation ($lnC_{fm,max}$ 3.14 and 3.83 mg g^{-1} for ∆T 10 and 20°C respectively), particularly for higher solubility solutes [45]. For such conditions, the system will seek to achieve a minimum Gibbs free energy by reducing surface area through driving dissolution of small crystals to enable the deposition of those growth units onto larger crystals [14,54]. This is comparable to the observations of Chen et al. [21] for MDC following an increase in feed temperatures which raised

supersaturation rate. By increasing membrane area, a higher supersaturation rate was established, which enabled a comparable supersaturation to be achieved at induction ($lnC_{fm,max}$ 3.72 and 3.83 mg g^{-1} for 7 and 37HF respectively) but within a shorter induction time. A more comparable mean crystal size was observed (L_{50} 90±1 and 98±4 µm for 7 and 37HF respectively), while the CSD for 7HF comprised a lower variance. The higher crystal size attained with 7HF compared to that achieved with 37HF at ΔT 10°C may be accounted for by the higher MSZW that was established, suggesting Ostwald's growth mechanisms to also dominate at the lower supersaturation rate imposed by the 7HF membrane. Increasing magma density from 23.9 to 25.9 wt.% fostered nucleation at a shorter induction time and at a lower supersaturation level while adopting a similar supersaturation rate. This decreased L_{50} from 98±4 to 72±6 µm when magma density increased from 23.9 to 25.9 wt.% respectively and narrowed the size distribution. This contrasts with Edwie et al. [5] who demonstrated that a higher supersaturation rate produced a lower median crystal size for NaCl without observation of Ostwald ripening during cooling crystallisation. The disparity may arise from the extent of the supersaturation rate applied, since cooling crystallisation of a solute with a flat solubility-temperature dependency implies a lower driving force may have been established. Importantly, crystal size and variance of the distribution are recognised to underpin crystal quality, and within this study several parameters are identified which independently govern the induction time, supersaturation and supersaturation rate in different ways that could be collectively applied to develop multiple kinetic trajectories for well-controlled crystal growth[21,55,56].

3.4 Conclusion

In this study, an analytical framework has been introduced to describe how multiple parameters collectively determine the supersaturation driving force in membrane distillation crystallisation which establishes the kinetics of nucleation and crystal growth. Many previous studies have sought to empirically relate water vapour flux to the kinetics of crystallisation. However, data gleaned through direct

measurement of induction time, complemented with membrane autopsy to characterise scaling, evidenced that for definitive characterisation, the supersaturation rate must be used as this provides a holistic description of MDC system characteristics that can be related directly to the nucleation kinetics. Crystalliser volume enabled discrimination of how discrete parameters adjusted the MSZW without incurring complex boundary layer modifications. For each parameter, an increased dependency on the membrane to support primary heterogeneous nucleation was observed at low supersaturation levels and extended induction times which is compatible with classical nucleation theory. This is distinct from the wider membrane distillation literature where scaling is often correlated to higher nucleation rates. Use of in-situ techniques for the direct measurement of induction evidenced how scaling was minimised toward the metastable limit where elevated supersaturation and short induction times illustrating a transition toward homogeneously controlled primary nucleation. However, each of the parameters studied were evidenced to determine the specific supersaturation threshold at which the critical Gibbs free energy was sufficient to initiate nucleation (and the specific mechanism). The nucleation kinetic constants obtained when increased membrane area indicate that comparable crystallisation characteristics can be obtained following scale-up, which is a unique facet of membrane distillation. When changing between parameters, either supersaturation rate, supersaturation or induction time could be sustained while the other two factors changed. In general, higher supersaturation rates led to higher crystal sizes with broader size distributions, being related to Ostwald ripening within an elevated region of supersaturation. However, by achieving a high level of supersaturation at a lower supersaturation rate, an equivalent crystal size could be achieved with a narrowed size distribution. The unique characterisation provided within this study introduces a foundation on which to develop synergistic strategies through coupling of these collective parameters to facilitate well-controlled crystal growth in membrane crystallisation systems.

3.5 Acknowledgements

This research was financially supported by European Research Council Starting Grant, ‘Sustainable chemical alternatives for reuse in the circular economy’ (StG, SCARCE, 714080).

3.6 Appendix A

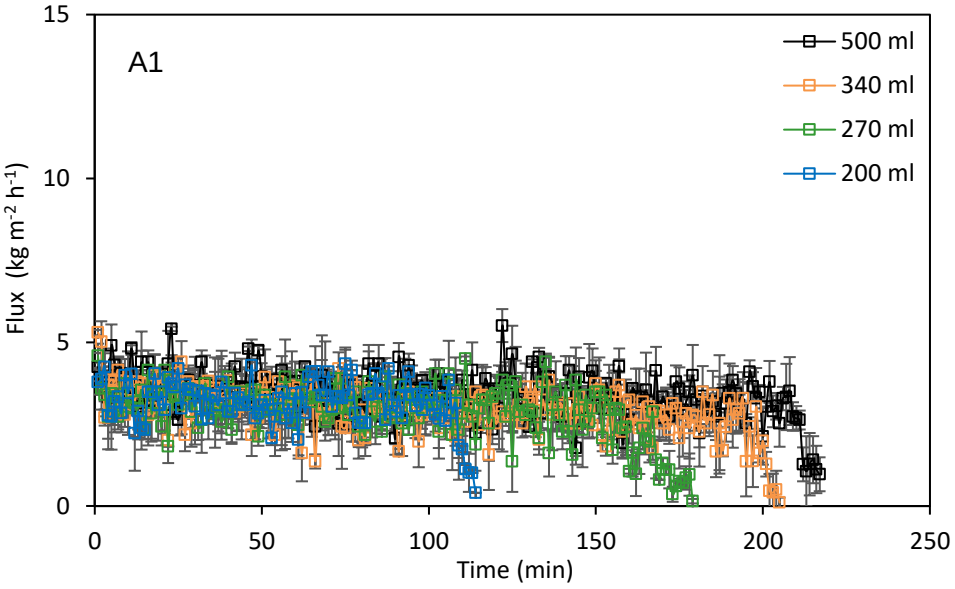

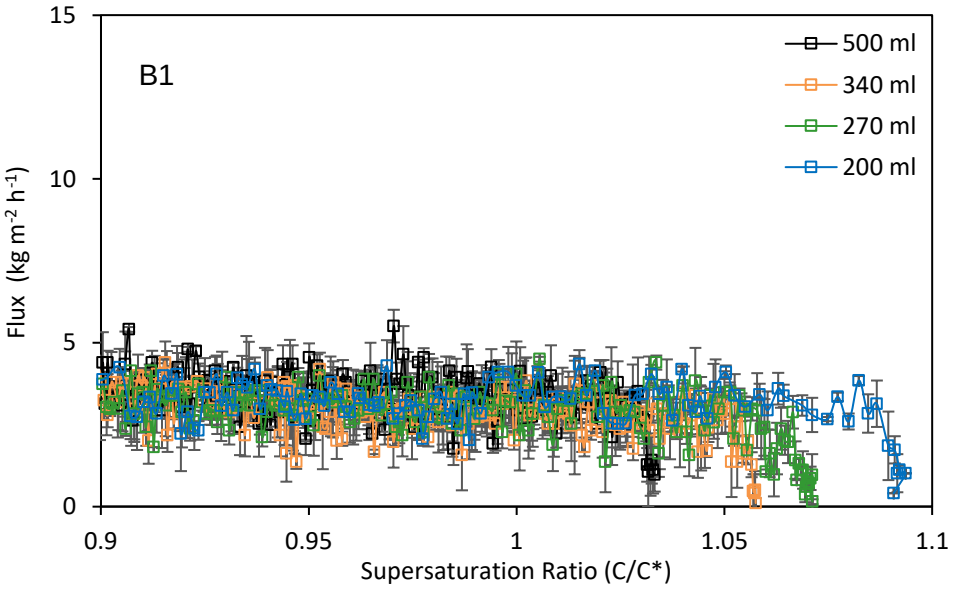

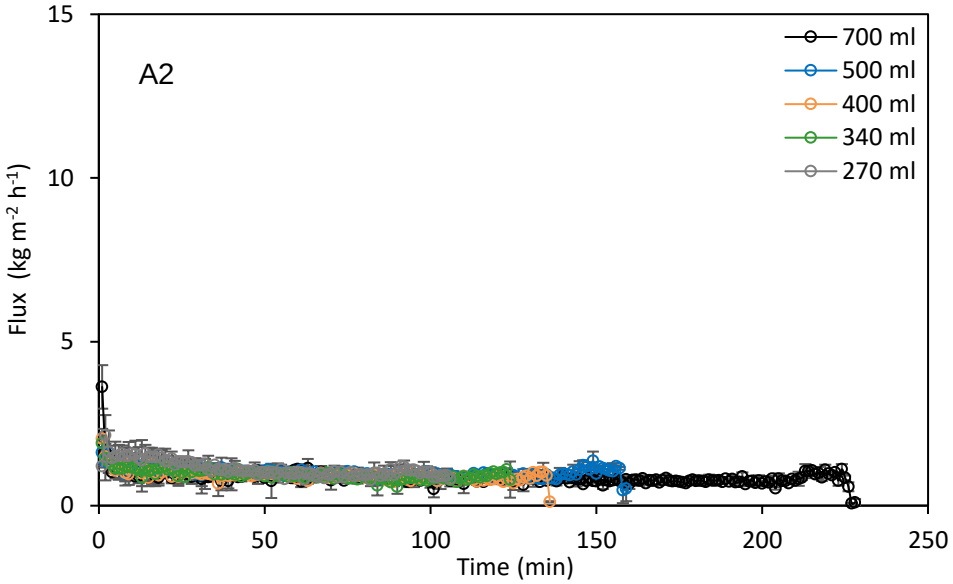
A2
700 ml
500 ml
400 ml
340 ml
270 ml
Flux (kg m-2 h-1)
Time (min)
0
5
10
15
0
50
100
150
200
250

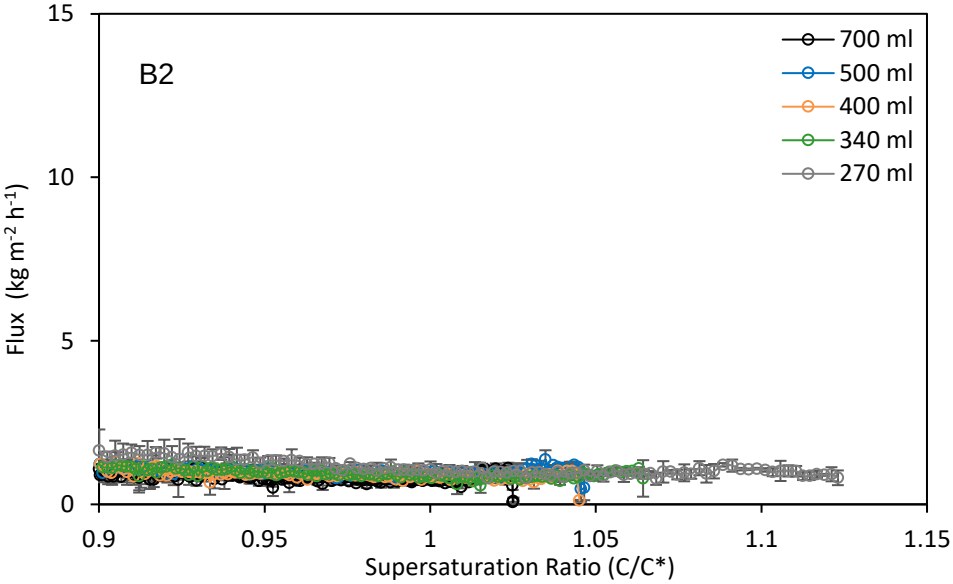
B2
700 ml
500 ml
400 ml
340 ml
270 ml
Flux (kg m-2 h-1)
Supersaturation Ratio (C/C*)
0
5
10
15
0.9
0.95
1
1.05
1.1
1.15

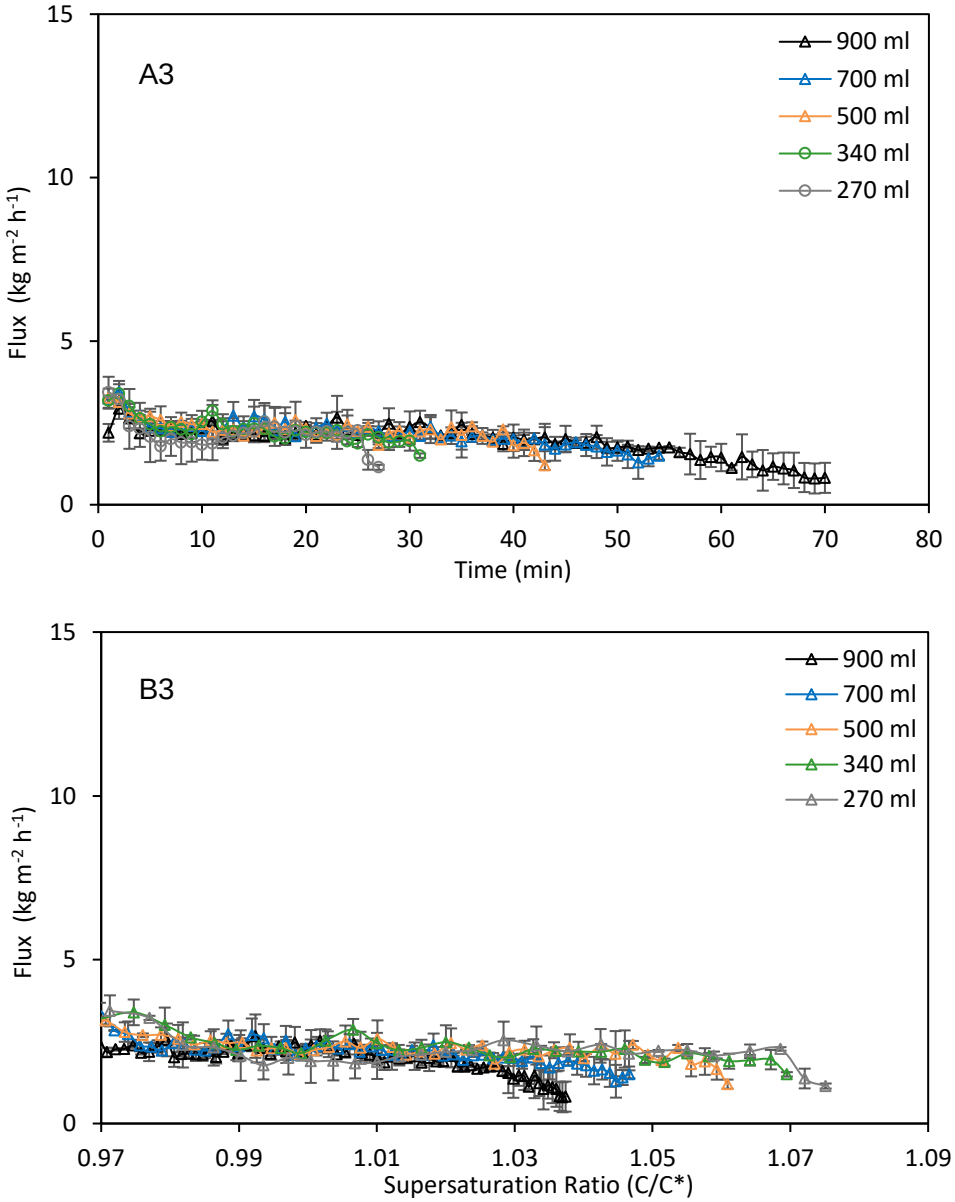

Figure A 3-1 *Permeation flux for different primary control variable: (A1,A2,A3); based on operating time; (B1,B2,B3); based on bulk supersaturation. Boundary conditions: Tbulk, 55±1°C; Velocity of feed and permeate=0.06 m* s^{-1}.

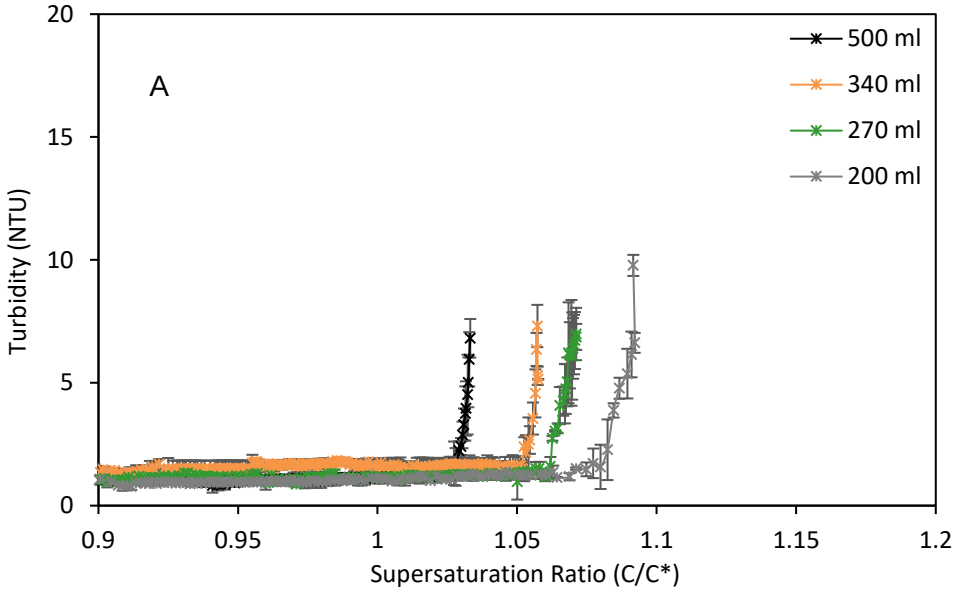
A
500 ml
340 ml
270 ml
200 ml
Turbidity (NTU)
Supersaturation Ratio (C/C*)
0
5
10
15
20
0.9
0.95
1
1.05
1.1
1.15
1.2

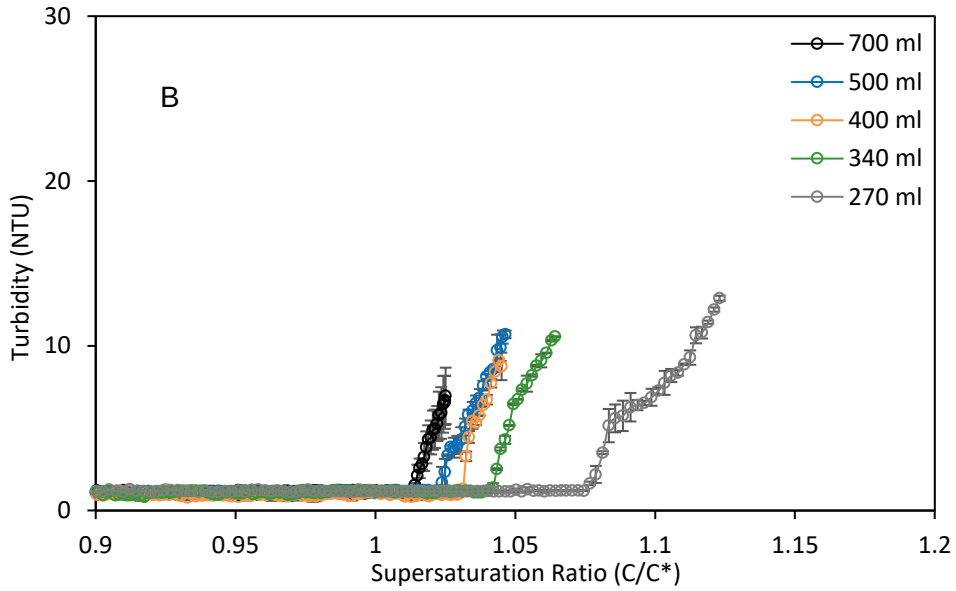
B
700 ml
500 ml
400 ml
340 ml
270 ml
Turbidity (NTU)
Supersaturation Ratio (C/C*)
0
10
20
30
0.9
0.95
1
1.05
1.1
1.15
1.2

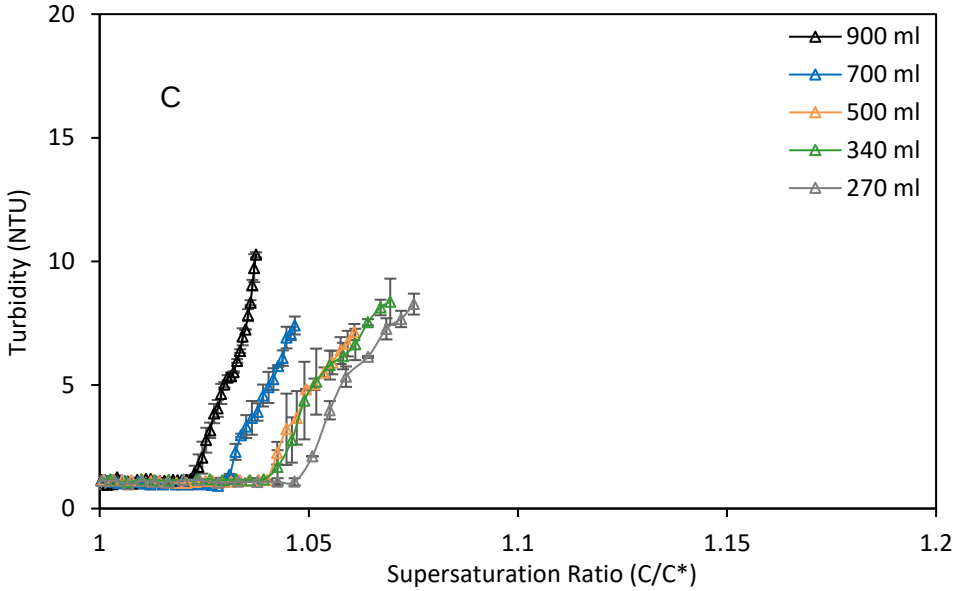

Figure A 3-2 *Turbidity profile during MDC operation based on bulk supersaturation at different primary control variables. (A): 7HF, %wt=23.9, ∆t=20°C; (B): 37HF, %wt=23.9, ∆t=10°C; (C): 37HF, %wt=25.9, ∆t=20°C. Boundary conditions: Tbulk, 55±1°C; Velocity of feed and permeate=0.06 m* s^{-1}.

3.7 References

[1] E. Chabanon, D. Mangin and C. Charcosset, Membranes and crystallization processes: State of the art and prospects, J. Memb. Sci. 509 (2016) 57–67.

[2] J. Liu, Q. Wang, H. Shan, H. Guo and B. Li, Surface hydrophobicity based heat and mass transfer mechanism in membrane distillation, J. Memb. Sci. 580 (2019) 275–288.

[3] A. Caridi, G. Di Profio, R. Caliandro, A. Guagliardi, E. Curcio and E. Drioli, Selecting the desired solid form by membrane crystallizers: Crystals or cocrystals, Cryst. Growth Des. 12 (2012) 4349–4356.

[4] G. Chen, Y. Lu, W.B. Krantz, R. Wang and A.G. Fane, Optimization of operating conditions for a continuous membrane distillation crystallization process with zero salty water discharge, J. Memb. Sci. 450 (2014) 1–11.

[5] F. Edwie and T.S. Chung, Development of simultaneous membrane distillation-crystallization (SMDC) technology for treatment of saturated brine, Chem. Eng. Sci. 98 (2013) 160–172.

[6] E. Drioli, G. Di Profio and E. Curcio, Progress in membrane crystallization, Curr. Opin. Chem. Eng. 1 (2012) 178–182.

[7] M.C. Sparenberg, S. Chergaoui, V. Sang Sefidi and P. Luis, Crystallization control via membrane distillation-crystallization: A review, Desalination. 519 (2022) 115315.

[8] E. Curcio, G. Di Profio and E. Drioli, Probabilistic aspects of polymorph selection by heterogeneous nucleation on microporous hydrophobic membrane surfaces, J. Cryst. Growth. 310 (2008) 5364–5369.

[9] T. Horseman, Y. Yin, K.S. Christie, Z. Wang, T. Tong and S. Lin, Wetting, Scaling, and Fouling in Membrane Distillation: State-of-the-Art Insights on Fundamental Mechanisms and Mitigation Strategies, ACS ES&T Eng. 1 (2021) 117–140.

[10] Y. Choi, G. Naidu, L.D. Nghiem, S. Lee and S. Vigneswaran, Membrane distillation crystallization for brine mining and zero liquid discharge: Opportunities, challenges, and recent progress, Environ. Sci. Water Res.

Technol. 5 (2019) 1202–1221.

[11] X. Jiang, X. Ruan, W. Xiao, D. Lu and G. He, A novel membrane distillation response technology for nucleation detection, metastable zone width measurement and analysis, Chem. Eng. Sci. 134 (2015) 671–680.

[12] G. Zeng, H. Li, S. Huang, X. Wang and J. Chen, Determination of metastable zone width and the primary nucleation kinetics of sodium sulfate, Theor. Found. Chem. Eng. 49 (2015) 869–876.

[13] K. Sangwal, On the interpretation of metastable zone width in anti-solvent crystallization, Cryst. Res. Technol. 45 (2010) 909–919.

[14] G. Di Profio, E. Curcio and E. Drioli, Supersaturation control and heterogeneous nucleation in membrane crystallizers: Facts and perspectives, Ind. Eng. Chem. Res. 49 (2010) 11878–11889.

[15] M.T. Chan, A.G. Fane, J.T. Matheickal and R. Sheikholeslami, Membrane distillation crystallization of concentrated salts - Flux and crystal formation, J. Memb. Sci. 257 (2005) 144–155.

[16] X. Zhang, R. Koirala, A. Date and V. Jegatheesan, Modelling and simulation of flux prediction and salinity variation in direct contact membrane distillation for seawater desalination and brine treatment, Desalination. 540 (2022) 116021.

[17] M. Hardikar, I. Marquez, T. Phakdon, A.E. Sáez and A. Achilli, Scale-up of membrane distillation systems using bench-scale data, Desalination. 530 (2022) 115654.

[18] J. Nývlt, Kinetics of nucleation in solutions, J. Cryst. Growth. 3–4 (1968) 377–383.

[19] X. Jiang, L. Tuo, D. Lu, B. Hou, W. Chen, G. He, Progress in membrane distillation crystallization: Process models, crystallization control and innovative applications, Front. Chem. Sci. Eng. 11 (2017) 647–662.

[20] X. Yang, R. Wang, L. Shi, A.G. Fane and M. Debowski, Performance improvement of PVDF hollow fiber-based membrane distillation process, J. Memb. Sci. 369 (2011) 437–447.

[21] G. Chen, Y. Lu, X. Yang, R. Wang and A.G. Fane, Quantitative study on

crystallization-induced scaling in high-concentration direct-contact membrane distillation, Ind. Eng. Chem. Res. 53 (2014) 15656–15666.

[22] M. Tomaszewska, M. Gryta and A.W. Morawski, Study on the concentration of acids by membrane distillation, J. Memb. Sci. 102 (1995) 113–122.

[23] F. Edwie and T.S. Chung, Development of hollow fiber membranes for water and salt recovery from highly concentrated brine via direct contact membrane distillation and crystallization, J. Memb. Sci. 421–422 (2012) 111–123.

[24] A. Ali, J.H. Tsai, K.L. Tung, E. Drioli and F. Macedonio, Designing and optimization of continuous direct contact membrane distillation process, Desalination. 426 (2018) 97–107.

[25] J. Phattaranawik, R. Jiraratananon and A.G. Fane, Heat transport and membrane distillation coefficients in direct contact membrane distillation, J. Memb. Sci. 212 (2003) 177–193.

[26] S. Karthika, T.K. Radhakrishnan and P. Kalaichelvi, A Review of Classical and Nonclassical Nucleation Theories, Cryst. Growth Des. 16 (2016) 6663–6681.

[27] S. Wang, M. Feng, H. Du, J.J. Weigand, Y. Zhang and X. Wang, Determination of metastable zone width, induction time and primary nucleation kinetics for cooling crystallization of sodium orthovanadate from NaOH solution, J. Cryst. Growth. 545 (2020) 125721.

[28] L. Zhou, Z. Wang, M. Zhang, M. Guo, S. Xu and Q. Yin, Determination of metastable zone and induction time of analgin for cooling crystallization, Chinese J. Chem. Eng. 25 (2017) 313–318.

[29] S. Karthika, T.K. Radhakrishnan and P. Kalaichelvi, Measurement of nucleation rate of ibuprofen in ionic liquid using induction time method, J. Cryst. Growth. 521 (2019) 55–59.

[30] R. Thanedgunbaworn, R. Jiraratananon and M.H. Nguyen, Shell-side mass transfer of hollow fibre modules in osmotic distillation process, J. Memb. Sci. 290 (2007) 105–113.

[31] H. Kurokawa and T. Sawa, Heat recovery characteristics of membrane distillation, Heat Transf. - Japanese Res. 25 (1996) 135–150.

[32] M. Khayet, Membranes and theoretical modeling of membrane distillation: A review, Adv. Colloid Interface Sci. 164 (2011) 56–88.

[33] A. Alkhudhiri, N. Darwish and N. Hilal, Membrane distillation: A comprehensive review, Desalination. 287 (2012) 2–18.

[34] M. Sudoh, K. Takuwa, H. Iizuka and K. Nagamatsuya, Effects of thermal and concentration boundary layers on vapor permeation in membrane distillation of aqueous lithium bromide solution, J. Memb. Sci. 131 (1997) 1–7.

[35] Y. Yun, R. Ma, W. Zhang, A.G. Fane and J. Li, Direct contact membrane distillation mechanism for high concentration NaCl solutions, Desalination. 188 (2006) 251–262.

[36] R.W. Field and J.J. Wu, Permeate Flux in Ultrafiltration Processes—Understandings and Misunderstandings, Membranes (Basel). 12 (2022) 1–18.

[37] L. Martínez, Comparison of membrane distillation performance using different feeds, Desalination. 168 (2004) 359–365.

[38] G. Du, Z. Sun, Y. Xian, H. Jing, H. Chen and D. Yin, The nucleation kinetics of ammonium metavanadate precipitated by ammonium chloride, J. Cryst. Growth. 441 (2016) 117–123.

[38] M. Lenka and D. Sarkar, Determination of metastable zone width, induction period and primary nucleation kinetics for cooling crystallization of L-asparaginenohydrate, J. Cryst. Growth. 408 (2014) 85–90.

[39] S. Datta and D.J.W. Grant, Effect of supersaturation on the crystallization of phenylbutazone polymorphs, Cryst. Res. Technol. 40 (2005) 233–242.

[40] M. Lenka, D. Sarkar, Determination of metastable zone width, induction period and primary nucleation kinetics for cooling crystallization of L-asparaginenohydrate, J. Cryst. Growth. 408 (2014) 85–90.

[41] K. Sangwal, A novel self-consistent Nývlt-like equation for metastable zone width determined by the polythermal method, Cryst. Res. Technol. 44

(2009) 231–247.

[42] E. Mielniczek-Brzóska, Effect of sample volume on the metastable zone width of potassium nitrate aqueous solutions, J. Cryst. Growth. 401 (2014) 271–274.

[43] D. Kashchiev, Note: on the critical supersaturation for nucleation., J. Chem. Phys. 134 (2011) 196102.

[44] K. Sangwal, E. Mielniczek-Brzóska and S. Barylska, Solubility of ammonium oxalate in water-acetone mixtures and metastable zone width of their solutions, Chem. Eng. Res. Des. 92 (2014) 491–499.

[45] G. Di Profio, S. Tucci, E. Curcio and E. Drioli, Controlling polymorphism with membrane-based crystallizers: Application to form i and II of paracetamol, Chem. Mater. 19 (2007) 2386–2388.

[46] K.W. Lawson and D.R. Lloyd, Membrane distillation, J. Memb. Sci. 124 (1997) 1–25.

[47] X. Ni and A. Liao, Effects of cooling rate and solution concentration on solution crystallization of L-glutamic acid in an oscillatory baffled crystallizer, Cryst. Growth Des. 8 (2008) 2875–2881.

[48] A. McPherson and B. Cudney, Optimization of crystallization conditions for biological macromolecules, Acta Crystallogr. Sect. F Struct. Biol. Commun. 70 (2014) 1445–1467.

[49] J. Rolf, T. Cao, X. Huang, C. Boo, Q. Li and M. Elimelech, Inorganic Scaling in Membrane Desalination: Models, Mechanisms, and Characterization Methods, Environ. Sci. Technol. 56 (2022) 7484–7511.

[50] T. Tong, A.F. Wallace, S. Zhao and Z. Wang, Mineral scaling in membrane desalination: Mechanisms, mitigation strategies, and feasibility of scaling-resistant membranes, J. Memb. Sci. 579 (2019) 52–69.

[51] J. Kim, J. Kim and S. Hong, Recovery of water and minerals from shale gas produced water by membrane distillation crystallization, Water Res. 129 (2018) 447–459.

[52] N. Kubota, A new interpretation of metastable zone widths measured for unseeded solutions, J. Cryst. Growth. 310 (2008) 629–634.

[53] J. Hou, S. Wu, R. Li, W. Dong and J. Gong, The induction time, interfacial energy and growth mechanism of maltitol in batch cooling crystallization, Cryst. Res. Technol. 47 (2012) 888–895.

[54] I. V. Alexandrova, A.A. Ivanov and D. V. Alexandrov, How the intermediate stage of a phase transition process transforms to the concluding stage of Ostwald ripening, J. Cryst. Growth. 532 (2020) 125456.

[55] G. Madras and B.J. McCoy, Dynamics of crystal size distributions with size-dependent rates, J. Cryst. Growth. 243 (2002) 204–213.

[56] M. Lenka and D. Sarkar, Determination of metastable zone width and nucleation kinetics for combined cooling and antisolvent crystallization of L-asparagine monohydrate in water-isopropanol mixture, J. Cryst. Growth. 501 (2018) 66–73.

4 Facile supersaturation control strategies for membrane distillation

Facile supersaturation control strategies for membrane distillation crystallisation

Ouda, Y. Bajón-Fernández, E. McAdam

Cranfield Water Science Institute, Cranfield University, UK

Corresponding author: e.mcadam@cranfield.ac.uk

Abstract

After primary nucleation occurs in membrane distillation, the supersaturation profile in the crystallising solvent tends to adjust to a new position in the metastable zone, which makes subsequent nucleation events and crystal growth difficult to control. This study therefore investigated supersaturation control strategies that can foster distinct nucleation and crystal growth kinetics following induction, which is critical to enabling the regulation of crystal size and morphology. The kinetic trajectory was modified by increasing membrane area, which enabled adoption of an equivalent water vapor flux and thermal properties to ensure negligible modifications to the boundary layer. An increase in supersaturation rate shortened induction time and raised supersaturation at induction. This broadened the metastable zone, and reduced scaling due to the increased supersaturation driving force favouring homogeneous primary nucleation. Introducing filtration at the crystalliser, reduced crystal deposition to sustain a consistent supersaturation rate over a longer hold-up time following induction. Population balance confirmed a reduction in nucleation rate with longer hold-up times, due to the consumption of supersaturation for crystal growth, resulting in larger crystal sizes. By modulating supersaturation trajectory, the system was repositioned for crystal growth within specific regions of the metastable zone, which inform the potential for further primary nucleation, and determine the extent of crystal growth. Different morphologies were also observed between crystals grown in the boundary layer and those grown in the bulk solution due to exposure to discrete supersaturation levels. Segregating the growth phase into the bulk solution therefore improved crystal habit, shape and purity. This study demonstrates facile supersaturation control strategies that can underpin sustained and controllable kinetic trajectories within membrane crystallisation, to enable production of a more controlled crystal growth phase, which is an acknowledged limitation within existing industrialised evaporative technologies.

Keywords: *Crystal growth kinetics; direct contact; scaling; packing density; hollow fibre*

4.1 Introduction

Crystallisation is one of the most important separation and purification processes for the manufacture of fine and bulk chemical products [1,2] and is emerging as a critical strategy for resource recovery in the environment sector [3]. The principle drawback to existing crystallisation technologies is that the undefined interfacial area introduces an uneven supersaturation rate (e.g. evaporation rate or cooling rate), which is challenging for the precise control of supersaturation level at induction, resulting in a poorly reproducible final crystal product [4–6]. Crystal properties can be critical to industrial applications, including crystal morphology (habit, shape, crystal size distribution-CSD), purity (well-organized building blocks into the lattice) and crystal structure (polymorphism) [1,7]. Membrane distillation (MD) has been proposed as a disruptive platform technology for crystallisation (MDC) as the fixed interfacial area and well-defined boundary layer ensure consistent control over heat and mass transfer processes, subsequently improving the regulation of supersaturation to advance governance over nucleation and crystal growth mechanisms [2,4,8,9].

Supersaturation is the driving force for the crystallisation process [10,11]. The metastable zone width (MSZW) represents the concentration difference between the solubility limit and the supersaturation level at the onset of nucleation (Figure 1A) [12,13]. The extent of supersaturation when nucleation is induced determines the MSZW boundary limit and informs on which primary nucleation mechanism will predominate [10]. According to Sangwal [14], the metastable zone limit is kinetic in nature and is linearly dependent on the supersaturation rate (or concentrating rate) [8]. During crystallisation, operating below the metastable limit is preferable to avoid spontaneous primary nucleation which produces a high number of crystals that are small in size and may also be of poor quality [4,15]. However, primary nucleation can occur within various regions of the metastable zone dependent upon the supersaturation rate [16]. Toward the lower limit of the metastable zone (approaching the solubility line), considerably lower supersaturation is available as the driving force for nucleation, which increases dependency on a heterogeneous substrate that can modify the interfacial energy sufficiently to lower the Gibbs free energy requirement for nucleation [4,10,17–19]. While this is thought to be a further advantage of the membrane surface in membrane crystallisation, the risk of membrane scaling via an

adhesive growth mechanism (presumed to be *heterogeneous* nucleation) is also introduced [19].

Following an initial primary nucleation event, further uncontrolled primary nucleation can occur due to the improper regulation of the supersaturation trajectory [20], where an overshoot by progressive concentration of the crystalline solution will introduce another new nucleation event [21] (Figure 4.1B). This condition may pose a challenge within membrane distillation, where the elevated concentration within the boundary layer (or film) will lead to production of a large number of small crystals in a short timeframe within the vicinity of the membrane, which increases the potential for scaling through a deposition mechanism (*homogeneous* mechanism) [5,19]. The consumption of saturation caused by the initial nucleation event usually repositions the system for crystal growth within in a less saturated region of the metastable zone, where growth may be sustained provided the supersaturation rate can match the consumption of supersaturation used for growth [22,23]. However, the consumption of supersaturation is either less than, equal to or can exceed the supersaturation rate of the system. Therefore supersaturation control strategies (SSC) have been developed to regulate the supersaturation profile in conventional crystallisers by adjusting the supersaturation rate to promote crystal growth [23]. The concept of SSC is to control the kinetics of crystallisation by maintaining the supersaturation profile within the desired MSZW region, which significantly improves the crystal size distribution, quality and shape (Figure 4.1A) [23,24]. However, the MSZW is a complex region where secondary nucleation cannot be avoided, resulting in the extensive generation of crystal fines [25,26]. The direct nucleation control (DNC) strategy has therefore been proposed which allows the system to cross the metastable boundary and induce primary nucleation, after which the supersaturation level is maintained at a lower saturation threshold (the ‘growth only’ zone) by sustaining particle number at a predetermined value using feedback control to regulate the supersaturation rate, therefore lowering the number of fines and ensuring a larger final crystal product size [27].

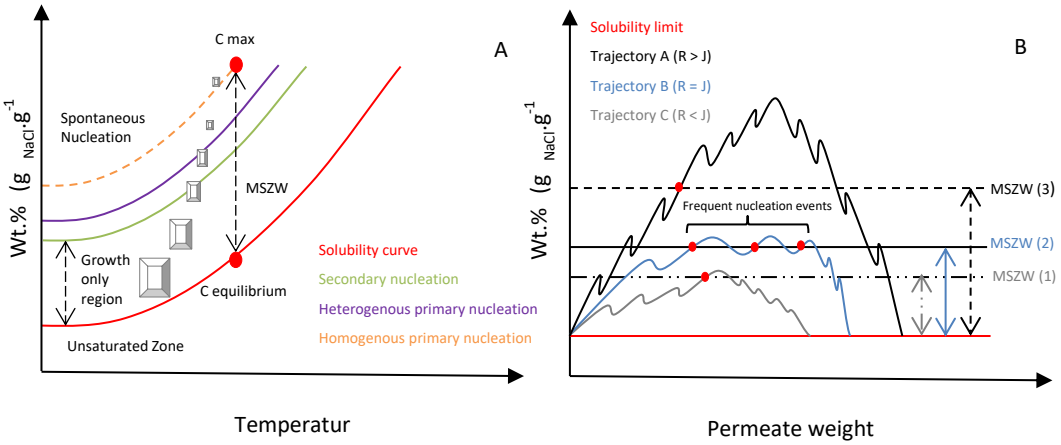

Figure 4.1 *(A) An illustration of metastable zone width boundaries; and (B) Schematic representation of the different supersaturation trajectories across the metastable zone width. For trajectory A, supersaturation rate following induction is greater than nucleation rate (R >J); trajectory B, supersaturation rate is equal to nucleation rate following induction (R=J); and trajectory C, supersaturation rate following induction is lower than nucleation rate (R<J).*

In MDC, supersaturation rate is typically modified through adjusting the membrane flux using feed temperature (T) or temperature difference (ΔT) to alter the vapour pressure difference across the membrane [28]. While evaporative crystallisation is generally preferred for salts with a relatively flat solubility-temperature dependency such as sodium chloride (NaCl) [11], adjustments to T or ΔT will nevertheless modify solubility and local solute concentration within the boundary layer, and will adjust complex mass and heat transfer processes across the membrane that can exacerbate polarisation within the boundary layer. Consequently, regulating the supersaturation rate to deliver a set supersaturation threshold is difficult to achieve making the kinetics of nucleation and crystal growth complicated to control, which restricts the opportunity to tailor final crystal quality [19,29,30]. This is an acknowledged limitation within conventional evaporative crystallisers, where temperature is the only regulatable variable and cannot be used as a method to initiate SSC or DNC strategies due to the limited precision of heating devices, and the long response times required to reach the desired temperature [23]. For MDC, the supersaturation rate must therefore be fixed to generate a sustained supersaturation gradient that can compensate for progressive primary nucleation events, while fostering reproducible crystal growth when transitioning across the MSZW. Jiang et al. [8] described using feed temperature and

temperature difference (ΔT) in MDC to transition across the MSZW by regulating supersaturation rate (*R*) to demonstrate distinct nucleation kinetics, but the supersaturation trajectory following the onset of primary nucleation that determines the primary nucleation mechanism (heterogenous or homogeneous), crystal growth mechanism and the potential for subsequent nucleation events is yet to be described.

In this study, we therefore seek to characterise a set of fixed supersaturation rates that foster distinct kinetic trajectories across the metastable zone to determine how this informs on the primary nucleation mechanism and the subsequent evolution of nucleation and crystal growth following induction. Each supersaturation rate is modified by a change in membrane area rather than using T or ΔT, as a method to sustain comparable solution chemistry, and mass and heat transfer characteristics within the boundary layer, independent of modifications to the MSZW. This permits comparative conditions with which to discern whether sufficient adjustment of the supersaturation rate can be achieved to sustain a consistent supersaturation gradient that offsets the consumption of supersaturation to foster subsequent nucleation events and crystal growth within specific regions of the metastable zone. In-line filtration is introduced as a method to retain crystals from the bulk solution within the downstream crystalliser, to permit crystal growth within a region of supersaturation closer to the 'growth only' zone, and to reduce the probability for scaling through deposition which we propose will improve consistency in the supersaturation rate following the preliminary primary nucleation event. Specific objectives are to: (i) characterise different supersaturation trajectories following primary nucleation through modulating the supersaturation rate using membrane area; (ii) determine how the nucleation kinetics are modified based on the shape of the supersaturation trajectory through the metastable zone; (iii) identify how the primary nucleation mechanism is adjusted by the supersaturation trajectory as a method to mitigate membrane scaling; and (iv) relate crystal properties to where within the metastable zone that supersaturation is primarily consumed for growth.

4.2 Materials and methods

4.2.1 Experimental setup

The commercial polypropylene hollow fibre (HF) membrane (Accural PP 300/1200, 3M, Wuppertal, Germany) comprised a 0.45 µm pore size, 300 µm wall thickness and porosity of 73±2% (Table 4.1). The fibres were potted into predrilled holes on a set of end plates that ensured a consistent spacing arrangement and were used to construct four membrane modules composed of 3, 7, 19, and 37 HF. The HF bundles were then mounted in a resealable acrylic membrane housing with a 15mm internal diameter and 150 mm effective membrane length. The MDC system was operated in a direct contact configuration (Figure 4.2). The feed solution volume and initial concentration were 450 ml and 23.9 wt.% sodium chloride (NaCl) concentration respectively.

Table 4.1 *Membrane and module specification*

Property	Units	Value	Fibre no.			
			3	7	19	37
Internal Diameter	$(\mathrm{di}, \mathrm{m})$	0.0012				
Outer diameter	$(\mathrm{do}, \mathrm{m})$	0.0018				
Wall Thickness	(m)	0.0003				
d_i/d_o	-	0.67				
Pore size	$(\mu\mathrm{m})$	0.45				
Porosity	(%)	73±2				
Contact angle[a]	(°)	131				
Fibre Length	(m)	0.15				
Shell inner diameter	(m)	0.015				
Packing density	(%)		4.4	10.2	27.7	53.9
Membrane area	(cm^2)		25.5	59.4	161.2	313.9

[a] Measured using water [29]

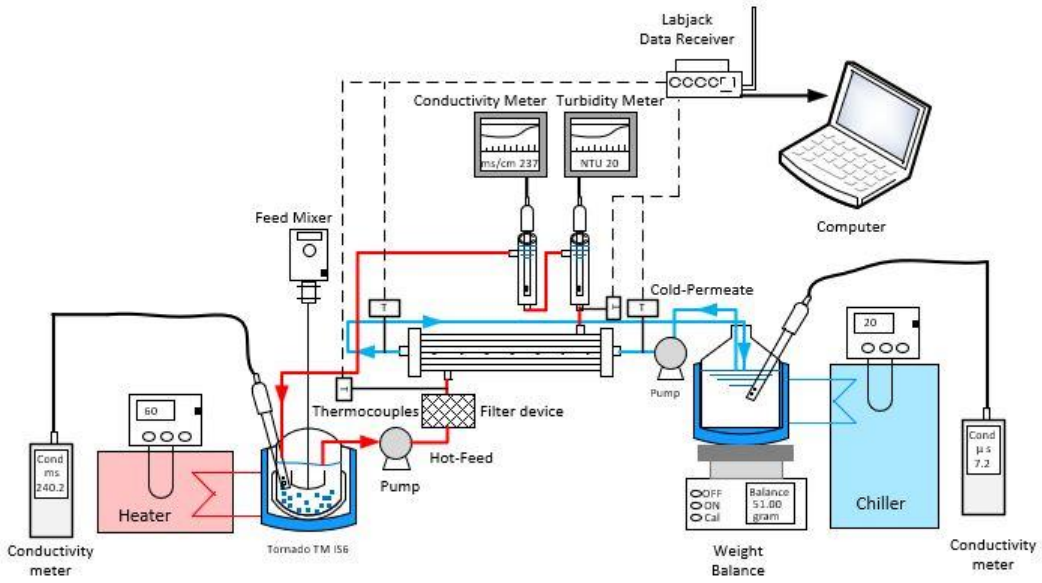

Figure 4.2 *Schematic diagram of the MDC setup.*

The feed solution was heated to 55±1°C using a heat exchange assembly (Tornado TM IS6, HUBER Ministat230; Radleys, Saffron Walden, UK) and circulated to the shell side of the membrane module. Deionised water was cooled down using a chiller (LT ECOCOOL 150, Grant Instruments, Shepreth, UK) and circulated co-currently through the lumen side of the hollow fibres. The feed and permeate velocities were fixed at 0.06 m s^{-1} to provide a laminar flow regime (*Re* 134 for 37 HF) within each membrane module that provided a consistent transmembrane ΔT of 20±2°C for each module. The temperature was recorded in-line using thermocouples with an accuracy of ±1°C (EI1034 Temperature Prop, LabJack Corporation, Lakewood, USA). The permeate flux was calculated by weighing the cumulative permeate mass with a balance (±0.5g accuracy, LBX model bench scale, Adam Equipment Co Ltd, Milton Keynes, UK) and normalising to membrane area. In-line dual optic fibre turbidimetry was employed to determine induction time for nucleation (InPro8200/S/Epoxy/120, Mettler Toledo, Manchester, UK). The dual optic fibre construction provides extremely sensitive detection of the onset of nucleation through backscatter technique, enabling the accurate determination of induction time. The supersaturation profile developed within the feed solution was monitored using a conductivity sensor (InPro 7100i conductivity

sensor, Mettler Toledo, Manchester, UK), offering responsive detection of conductivity changes following the utilisation of supersaturation for nucleation and crystal growth (range 0.02 to 500 mS cm^{-1}, accuracy ±5 mS cm^{-1}). The transformation of conductivity data (ms cm^{-1}) to concentration (g $_{NaCl}$ g^{-1} $_{solution}$) involved construction of a calibration curve that was developed through the direct measurement of conductivity within solutions of different supersaturation states (range between 24 to 29 g $_{NaCl}$ g^{-1} $_{solution}$) at a comparative temperature to the proposed experiment. The filtration device that was implemented to retain crystals within the crystalliser, consisted of a coarse filter (polyester 10 µm square mesh fabric, Monodur™, Clear Edge Filtration, Geldern, Germany). A 'just-suspended' stirring speed was estimated for the crystalliser providing 'off-bottom' particle stratification to aid retention of the crystal phase within the crystalliser. Experiments were carried out in triplicate, with the average reported.

4.2.2 Crystals and membrane scaling analysis

The crystalline solution was filtered through a 0.45 µm nylon filter (Whatman, Dorset, UK) to collect crystals from the bulk solution within the crystalliser. The crystals were weighed and sized after being dried over a desiccant (Genlabs drying cabinets 200L, Zoro, London, UK) for 48 hours (T ~23˚C). CSD were characterised using optical microscopy (Lumenera Infinity 3-3 Camera with 5/0.12 160/- lens), with captured images analysed using Image ProPremier software (v9.2, Media Cybernetics, Rockville, US). Each CSD was performed in triplicate. At least 800 crystals were used to construct each CSD to minimise the standard error of the distribution. The coefficient of variation (CV) was calculated according to the following equation [30]:

$$CV = \frac{L_{84\%} - L_{16\%}}{2\,L_{50\%}} \quad \textbf{(4-1)}$$

To determine the extent of crystal scaling via adhesive or deposition pathways, the membrane was dried over a desiccant for 48 hours (temperature ~23˚C) and weighed using a high precision balance (0.02-62g range, 0.0001g precision, Fisherbrand™, Loughborough, UK). Morphology of the crystals generated on the membrane and in the bulk suspension were analysed using a scanning electron microscope (SEM) (TESCAN VEGA3, Cambridge, UK) at an accelerating voltage of 20 kV.

4.2.3 Mass and heat transfer in membrane distillation

Permeate flux N (kg m^{-2} h^{-1}) was calculated using [31]:

$$N = \frac{m}{A \times \Delta t} \quad \textbf{(4-2)}$$

where m is the permeate mass (kg), A is membrane area (m^2), and Δt is the time interval (h).

The heat transfer in membrane distillation comprises of conductive heat through the membrane Q_c (W m^{-2}), and the latent heat from vapor flux Q_v (W m^{-2}) [31]:

$$Q = Q_c + Q_v = \left(\frac{k_m}{\delta_m}\right)\left(T_{fm} - T_{pm}\right) + NH_{V,T} \quad \textbf{(4-3)}$$

where δ_m is the membrane thickness (m), k_m is membrane thermal conductivity (W m^{-1} K^{-1}), T_{fm} , T_{pm} are feed and permeate temperatures at membrane film and $H_{V,T}$ is the latent heat of vaporisation (KJ kg^{-1}) [32]:

$$k_m = k_p(1 - \varepsilon) + k_g\varepsilon \quad \textbf{(4-4)}$$

$$\mathrm{HV,T} = 1.7535\, T_{m,avg} + 2024.3 \quad \textbf{(4-5)}$$

where k_p is polymer thermal conductivity (W m^{-1} K^{-1}), Ɛ is membrane porosity, k_g is the air thermal conductivity (W m^{-1} K^{-1}), and $T_{m,avg}$ is the average of film temperature (K) [32,33]:

$$T_{m,avg} = \frac{T_{fm} + T_{pm}}{2} \quad \textbf{(4-6)}$$

The feed T_{fm} and permeate temperatures T_{pm} within the membrane film can be expressed as [26,31]:

$$T_{fm} = T_f - \left(T_f - T_p\right)\left[\frac{1/h_f \times d_i/d_o}{1/h_f \times d_i/d_o + 1/(h_m + h_v) + 1/h_p}\right] \quad \textbf{(4-7)}$$

$$T_{pm} = T_p - \left(T_f - T_p\right)\left[\frac{1/h_p}{1/h_f \times d_i/d_o + 1/(h_m + h_v) + 1/h_p}\right] \quad \textbf{(4-8)}$$

where $d_i/d_\circ$ is inner/outer diameter ratio, bulk temperature in feed and permeate T_f and T_p (K), h_p is the permeate heat transfer coefficient (W m^{-2} K^{-1}), and h_f is feed heat transfer coefficient (W m^{-2} K^{-1}):

$$h_{f,p} = Nu \times \frac{k_{f,p}}{d_{h_{f,p}}} \quad \textbf{(4-9)}$$

where k_f and k_p are thermal conductivity of feed and permeate (W m^{-1} K^{-1}), d_{hf} and d_{hp} are hydraulic diameter of feed and permeate flow channel (m), Nu is Nusselt's number, $h_m = k_m/\delta_m$ is the membrane heat transfer coefficient (W m^{-2} K^{-1}) and h_v is the vapour heat transfer coefficient (W m^{-2} K^{-1}):

$$h_v = \frac{NH_{v,(T_{fm}+T_{pm})/2}}{(T_{fm}-T_{pm})} \quad \textbf{(4-10)}$$

From this, the temperature polarisation coefficient (TPC) can be calculated by iteration:

$$TPC = \frac{T_{fm}-T_{pm}}{T_f-T_p} \quad \textbf{(4-11)}$$

The bulk solute concentration leading up to nucleation was estimated by mass balance, assuming negligible solute breakthrough into the permeate, which was confirmed by directly monitoring permeate conductivity during experimentation. The membrane film concentration was calculated from the concentration polarisation coefficient (CPC) based on the film model [34]

$$CPC = \frac{c_{fm}}{c_f} = exp\left(\frac{N}{\rho \times k_s}\right) \quad \textbf{(4-12)}$$

where C_{fm} is the concentration adjacent to the membrane surface (g $_{NaCl}$ g^{-1} $_{solution}$), C_b is the bulk concentration (g $_{NaCl}$ g^{-1} $_{solution}$), ρ is the solution density (kg m^{-3}) and k_s is the solute mass transfer coefficient (m s^{-1}) which was calculated from Chilton-Colburn analogy based on the heat and mass transfer correlation [35,36].

$$\frac{Sh_f}{Sc_f^{0.33}} = \frac{Nu_f}{Pr_f^{0.33}} \quad \textbf{(4-13)}$$

where Sh_f is the Sherwood number, Sc is the Schmidt number, Nu_f is the Nusselt number and Pr_f is the Prandtl number of feed solution.

$$Sh_f = \frac{k_s D_h}{D_s} \quad \textbf{(4-14)}$$

$$Sc_f = \frac{\mu_f}{P_f D_s} \quad \textbf{(4-15)}$$

$$Nu_f = 1.86(Re\,\mathrm{Pr}\,{}^{D_h}/_{L})^{0.33} \quad \textbf{(4-16)}$$

$$Re = \frac{d_h V \rho}{\mu} \quad \textbf{(4-17)}$$

$$Pr_f = \frac{C_p \mu}{k_s} \quad \textbf{(4-18)}$$

where Re is Reynold number (-), D_h is hydraulic diameter (m), D_s is solute diffusion coefficient (m^2 s^{-1}), μ is viscosity (Pa s^{-1}), L is the hollow fibre length (m), v is the feed velocity (m s^{-1}).

4.2.4 Characterisation of nucleation and crystal growth kinetics

The MSZW was calculated from the developed method proposed by Nývlt [8]. This approach assumes supersaturation to be linearly related to the MSZW in the range of concentration where nucleation first occurs (induction). Therefore, the upper supersaturation limit at the membrane film $\Delta C_{max,fm}$ (mg $_{NaCl}$ g^{-1} $_{solution}$) is assumed to be proportional to the supersaturation rate R' (g .100g $_{solution}$ $.h^{-1}$), where both correspond to the nucleation rate by the power-law equation as follows:

$$J = k\left(\Delta C_{max,fm}\right)^{n} = \left(\frac{dc_0}{dt}\right)_t = \frac{F_p\, C_0}{m_0 - \int_0^t F_P d\tau} \quad \textbf{(4-19)}$$

$$R' = \left(\frac{dCo}{dt}\right)_t = \frac{F_p\, C_0}{m_0 - \int_0^t F_P d\tau} \quad \textbf{(4-20)}$$

where F_p is the permeate flow rate (kg h^{-1}), m_o is the initial mass of the crystalline solution (kg), C_o is the equilibrium concentration (g $_{NaCl}$ g^{-1} $_{solution}$), $\Delta C_{max,fm}$, (which is, c_{fm}-c*). The kinetic parameters, k (No. m^{-3-n} s^{-1+n}) and n (-) are the nucleation constant and nucleation order respectively and depend on the formation mechanism of the stable nucleus and its growth evolution into viable entities [37], which are determined from a linear fit between lnR' and $\ln\Delta C_{max,fm}$ [8]:

$$\ln(\Delta C_{max,fm}) = \frac{1}{n}\ln\left(\frac{C_0}{k}\right) + \frac{1}{n}\ln\left(\frac{F_p}{m_0 - \int_0^t F_P d\tau}\right) \quad \textbf{(4-21)}$$

Nucleation and crystal growth rates were calculated from the crystal suspension according to population balance theory [34]:

$$\frac{dn(l)}{dl} + \frac{n(l)}{Gt} = 0 \quad \textbf{(4-22)}$$

This assumes a well-mixed suspension during crystallisation and as crystal growth rate is independent of size at a given supersaturation [38], equation (22) can be expressed as:

$$n(L) = n(0)exp - \frac{L}{G\,t} \quad \textbf{(4-23)}$$

where n(L) is the crystal population density (m^{-4}), n° is the population density at (L=0) (m^{-1}), G is the growth rate (m s^{-1}), and t is the residence time (sec). From a linear fit of Ln,n(L) versus L, the intercept at (L=0) is equal to population density (n°) and the growth rate provided by the gradient (-1/Gt). The nucleation rate B^0 (No. m^{-3} s^{-1}) was therefore determined as follows:

$$B^0 = n^0\, G \quad \textbf{(4-24)}$$

4.3 Result and discussion

4.3.1 Consistent primary nucleation is achieved with or without in-line filtration

Comparable initial permeation fluxes of around 3.6 kg m^{-2} h^{-1} were observed for each HF membrane examined (Figure 4.3). This indicates consistent mass and heat transfer conditions were sustained when increasing membrane area; an assertion supported by the attainment of a comparable feed temperature and ΔT for each module of 55±1°C and 20±2°C respectively. The only exception was the 37 HF module, which recorded a marginally lower initial permeation flux of 2.6 kg m^{-2} h^{-1} (Figure 4.3). While a comparable superficial velocity was developed within this module (V_L, 0.06 m s^{-1}), the small modification in flux may be attributed to an adjustment of the local superficial velocity due to the higher packing density [39]. Importantly, the increase in membrane area was demonstrated to enhance the supersaturation level that could be achieved. Each of the flux profiles comprised of three stages (Figure 3b, inset): (i) a stable permeation flux that slightly decreased over time due to a reduction in water activity that is imposed by an increase in feed solution concentration [40–42]; (ii) a dramatic decline in permeation flux at a higher supersaturation level, which is thought to correspond to the onset of scaling, where a crystalline layer is initiated through either adhesive crystal growth (*heterogeneous* nucleation) or deposition of crystals formed within the bulk solution (*homogeneous* nucleation) which increases resistance to mass and heat transfer [34]; and (iii) the complete diminution of permeation flux [19,28]. Stage two flux decline was observed at higher levels of supersaturation as membrane area increased, while the time required to reach stage two was much less for modules comprising more HF. To illustrate, stage two flux decline was recorded at 338, 200, 78 and 56 minutes for 3, 7, 19 and 37 HF membrane modules respectively. Introducing filtration to advance crystal retention in the crystalliser downstream of membrane distillation, enabled the suppression of stage two flux decline to achieve a considerably higher supersaturation level. For example, the supersaturation level achieved at the onset of stage two flux decline with the 37 HF module, increased from c/c* 1.08 to 1.15 when using filtration.

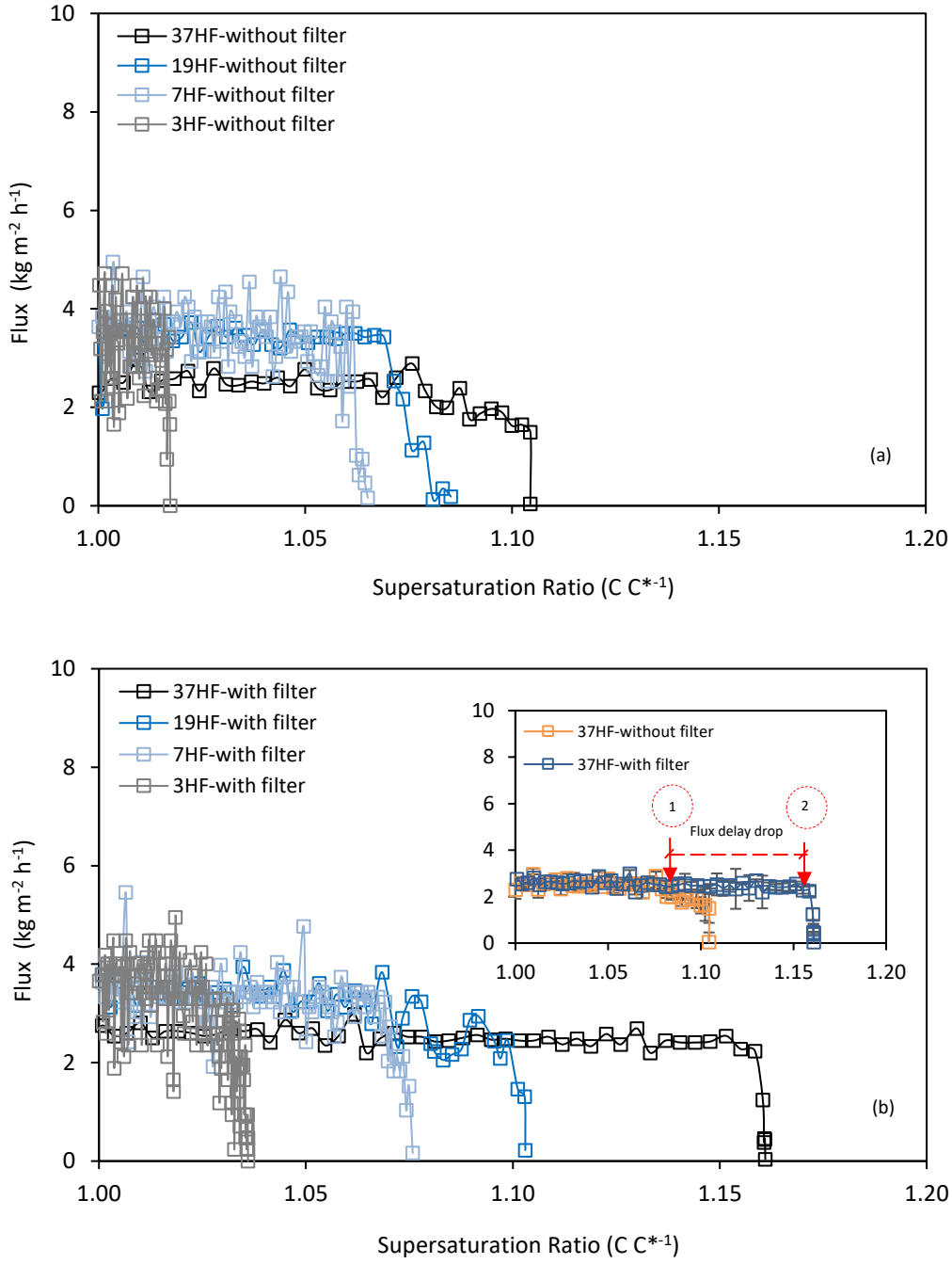

Figure 4.3 *Water vapour flux following progressive concentration of concentrated brine solution for different process configurations: (a) without filter device; and (b) with filter device. Inset: evidence for how inclusion of filtration extends residence time in the system. Bulk supersaturation is calculated based on flux mass balance. Conditions: Tbulk 55±1°C; ΔT 20±2°C; initial NaCl concentration, 23.9 Wt.%; feed and permeate velocity, 0.06 m s^{-1}. Standard error of permeation flux was calculated based on differences in triplicate measurements for each membrane modules; (A) 3HF, 3.6±0.4; 7HF, 3.7±0.4; 19HF, 3.5±0.2; 37HF, 2.6±0.1; (B) 3HF, 3.8±0.4; 7HF, 3.4±0.3; 19HF, 3.2±0.2; 37HF, 3.1±0.1.*

Turbidimetric measurements provided evidence for the onset of bulk nucleation and confirmed observation from the flux trends that nucleation proceeds at higher supersaturation through an increase in membrane area (Figure 4.4). The time elapsed from reaching a supersaturated state (c/c*, 1) to the first appearance of the bulk crystal phase is defined as the induction time [43,44]. While the inclusion of filtration downstream of MD was observed to increase the maximum supersaturation obtained for the duration of the experiment, both the supersaturation level and induction times achieved for primary nucleation were comparable regardless of whether filtration was used (Figure 4.5).

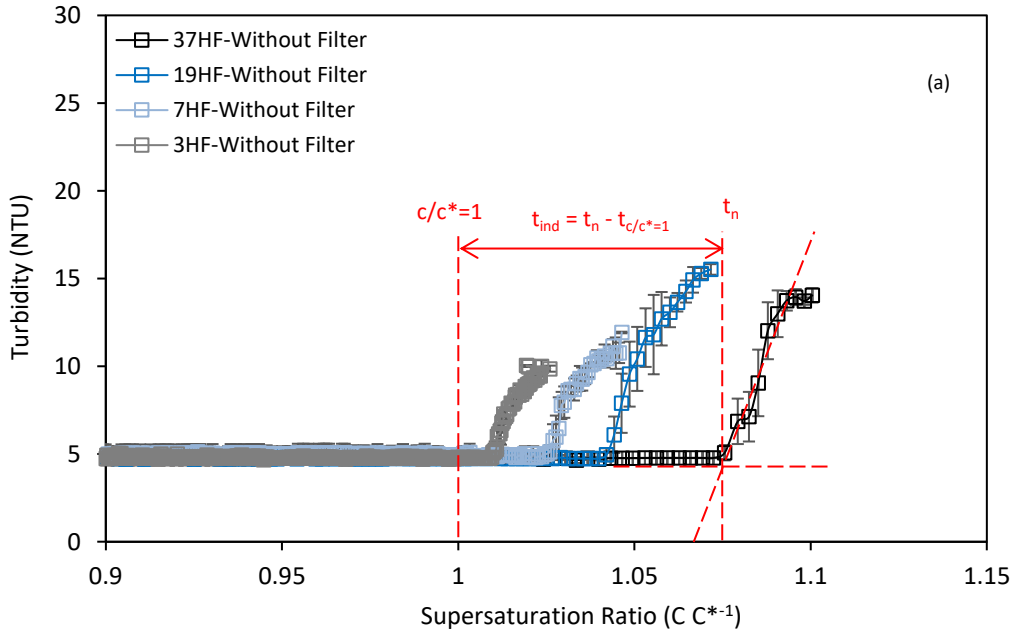

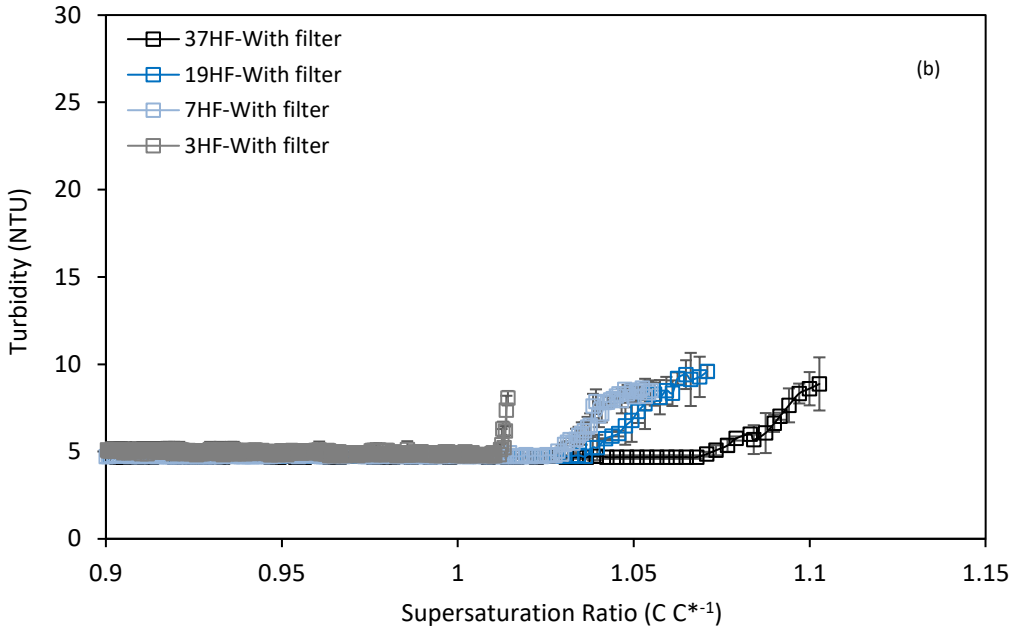

Figure 4.4 *Turbidity profiles characterising bulk nucleation events for operation: (a) without filter device; and (b) with filter device. Supersaturation at induction is increased by modifying membrane area. Conditions: Tbulk 55±1°C; ΔT 20±2°C; initial NaCl concentration, 23.9 Wt.%; feed and permeate velocity, 0.06 m s^{-1}.*

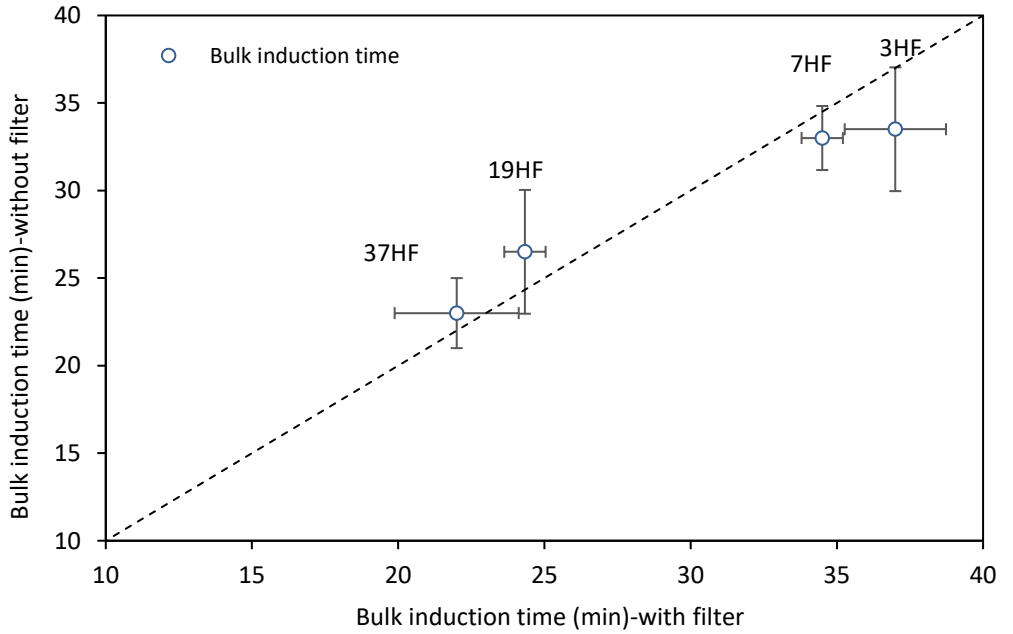

Figure 4.5 *Comparison of induction time between both MDC configurations (with and without in-line filtration) based on turbidity demonstrates that induction is achieved at the same time regardless of whether filtration is employed in the recycle line. Conditions: Tbulk 55±1°C; ΔT 20±2°C; initial NaCl concentration, 23.9 Wt.%; feed and permeate velocity, 0.06 m s^{-1}.*

We suggest that the extended operation of MD with filtration may therefore be due to the reduction of deposition onto the membrane through restricting recycling of the crystal phase, which is supported by the lower turbidity values recorded when operating with filtration in place. This not only enables higher supersaturation to be achieved, but also creates a more consistent flux over a longer period, which implies a greater control over supersaturation rate and thus should provide for closer control over the kinetics of nucleation and crystal growth. Critically, this study also demonstrates that the stage-two inflection point which many authors have previously employed as a surrogate measure for the onset of nucleation [2,34] is in fact mechanistically distinct from that of induction time as previously hypothesised by [19].

4.3.2 Distinct supersaturation profiles develop when increasing membrane area

The supersaturation profiles developed within the boundary layer (film) and bulk solution were characterised to distinguish their implications for adjusting crystallisation kinetics at the onset of primary nucleation. Typically concentration and temperature polarisation are modified by the mass and heat transfer mechanisms established within the boundary layer [19,42]. In this study, by increasing supersaturation rate with membrane area rather than T or ΔT, TPC and CPC were relatively consistent at the outset of filtration, due to the consistent flux established for each module, enabling total thermal losses to become proportional to membrane surface area, resulting in a constant ΔT of 20±2°C. However, at induction, a slight increase in TPC was noted (from 0.5 to 0.56) commensurate with a minor reduction in CPC (1.072 to 1.027 for 3 and 37 HF respectively when operating without filter) (Figure 4.6). This is due to the increase in supersaturation that was achieved as supersaturation rate was elevated, which slightly reduced the vapour pressure (and thus flux) at induction, approximately in proportion to the membrane surface area.

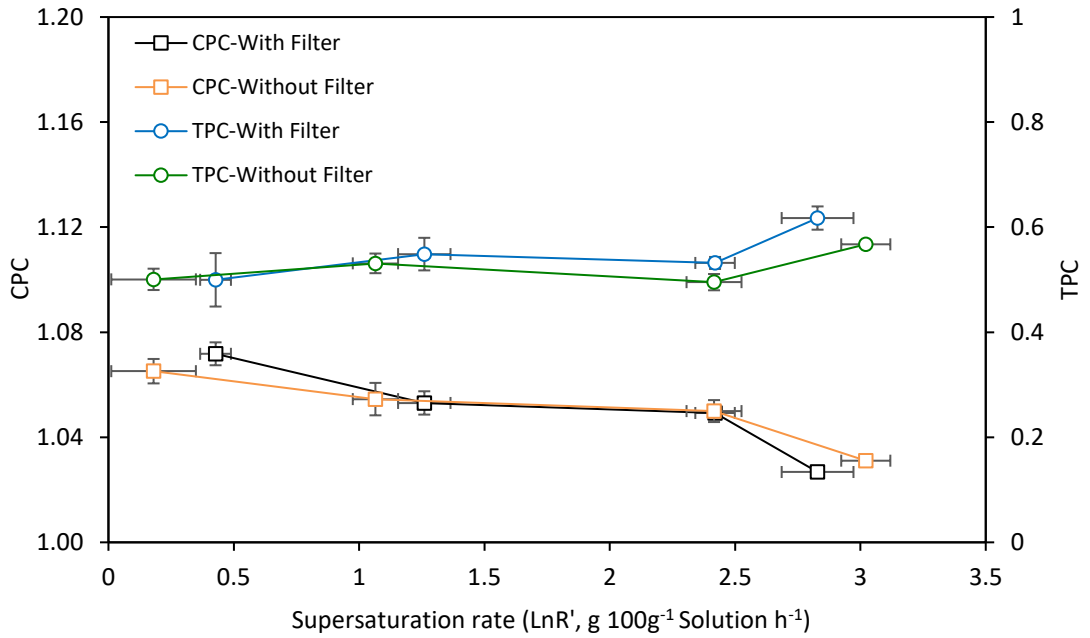

Figure 4.6 *Concentration and temperature polarisation coefficients (CPC and TPC) determined for each module determined when concentrating rate (LnR') is increased by membrane area. Comparison evidences boundary layer characteristics are similar at induction regardless of whether filtration is employed in the recycle line. Conditions: Tbulk 55±1°C; ΔT 20±2°C; initial NaCl concentration, 23.9 Wt.%; feed and permeate velocity, 0.06 m s^{-1}.*

While this thermal adjustment will introduce a subtle change in solute concentration in the boundary layer at induction, it is primarily the increase in membrane area that modifies the supersaturation rate and is ultimately responsible for the supersaturation that is achieved at induction [8,19]. Since temperature is sustained within the bulk conditions and is not subject to polarisation, the trajectory across the MSZW is likely to be characteristically distinct between these regions, and will determine the kinetics of nucleation, crystal growth and the predominant primary nucleation mechanism [8,11] (Figure 4.7). For the bulk conditions, the MSZW at induction increased from 27.0 to 28.8% when the membrane module increased from 3HF to 37HF (0.18 to 3.02 g 100g^{-1} solution h^{-1}). Comparable MSZW were developed for the initial primary nucleation event independent of whether in-line filtration was applied. Polarisation phenomena in the film increased the MSZW that was attained within the film, ranging from 28.3% for 3HF to 29.5% for 37HF. The wider MSZW can be attributed to the higher supersaturation rate (higher driving force) which introduces an excess free

energy into a non-equilibrium condition bringing the critical free energy requirement for nucleation to a minimum [8,10,14] (Figure 4.8). The relative difference between supersaturation ratios achieved in the bulk and film reduced at higher supersaturation rates. This is due to the modification in vapour pressure at induction, which will be lowest at the highest concentrating rate due to the elevated supersaturation in the film, subsequently adjusting C-C* due to the slight modification in TPC and CPC [29,31]. While this constitutes a reduction in the relative difference between supersaturation achieved in the bulk and film at induction, the absolute difference in supersaturation between bulk and film remains significant for each condition (Figure 4.7).

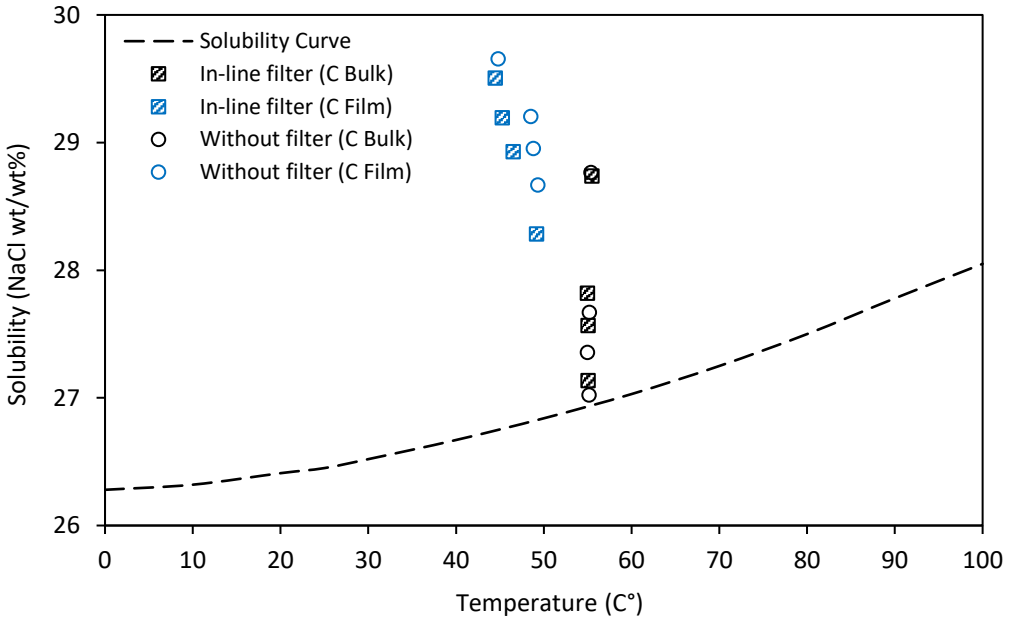

Figure 4.7 *The supersaturation achieved at induction is used to construct the metastable zone width (MSZW) using bulk and film concentrations (wt. NaCl/wt., %). Conditions: Tbulk 55±1°C; ΔT 20±2°C; initial NaCl concentration, 23.9 Wt.%; feed and permeate velocity, 0.06 m s^{-1}.*

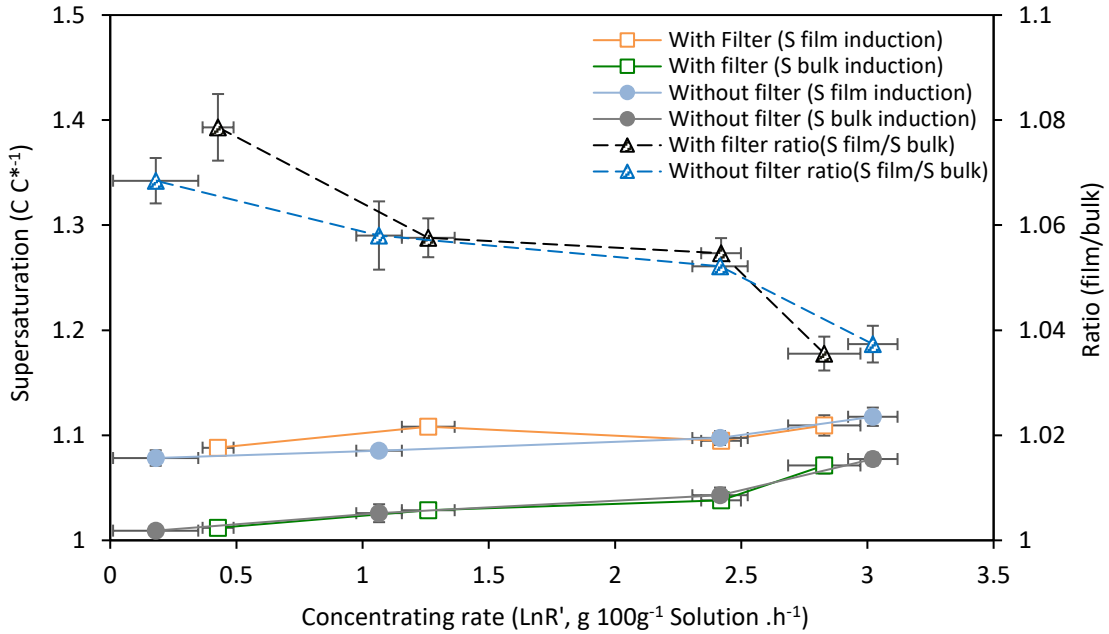

Figure 4.8 *Extent of supersaturation (c/c*) achieved based on the concentrating rate (LnR') imposed by an increase in membrane area; supersaturation attained within bulk and boundary layer (film) are compared. Bulk supersaturation is calculated based on flux mass balance and film concentration is calculated according to CPC values. Conditions: Tbulk 55±1°C; ΔT 20±2°C; initial NaCl concentration, 23.9 Wt.%; feed and permeate velocity, 0.06 m s^{-1}.*

Membrane scaling was greatest when the minimum supersaturation rate was employed (Figure 4.9), which corresponded to the lowest supersaturation level at induction, and the longest induction time (Figures 4.4 and 4.5). This condition can be described through classical nucleation theory as possessing a considerable free energy barrier to nucleation, increasing the relevance of a foreign substrate that can modify the interfacial energy of the system to permit primary heterogeneous nucleation to occur [2,45,46]. Previous authors have suggested that the modest reduction in film temperature identified in this study at the lowest supersaturation rate (3HF), will raise the probability for scaling through lowering of the solubility limit within the vicinity of the membrane [28,29]. However, the solubility-temperature dependency for NaCl is negligible [28]. As supersaturation increased, and induction time shortened, membrane scaling was considerably reduced. The higher supersaturation rate introduces the necessary excess free energy to lower the energy requirement for primary nucleation to proceed through a homogeneous mechanism [10,47].

Consequently, less scaling via adhesive growth (or heterogeneous nucleation) is observed at higher supersaturation rate. This transition to a primarily homogeneous mechanism is supported by comparison of scaling data from experiments with and without in-line filtration in place at high supersaturation rates. While the preliminary nucleation kinetics have been shown identical between the two scenarios (Figure 4.4 and 4.5), the difference in scaling between the filter and no filter systems, evidences the contribution of deposition from crystals formed through a homogeneous mechanism begins to dominate scaling as supersaturation rate is increased. Identification of conditions that minimise scaling by adhesive growth are critical to sustaining the supersaturation trajectory following the preliminary nucleation event. Mitigating deposition through in-line filtration should also support a sustained and consistent supersaturation rate (Figure 4.3b), providing greater control over crystallisation kinetics.

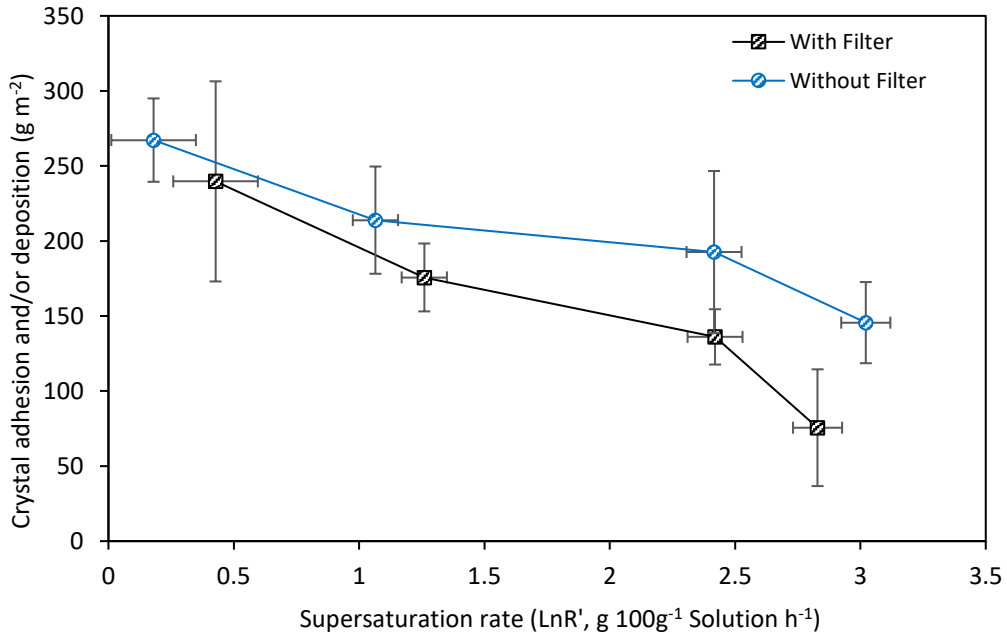

Figure 4.9 *The distinction in scaling mechanisms is observed, where the extent of surface adhesion and/or deposition at the membrane surface is dependent on the concentrating rate applied, and the presence of in-line filtration in the recycle line. Increasing concentrating rate (LnR') limits adhesive growth of scalant, while in-line filtration reduces deposition.*

Each supersaturation rate was evaluated (with in-line filtration applied) to ascertain how the supersaturation trajectory develops, as this provides the driving force for

crystallisation following the preliminary primary nucleation event (Figure 4.10). The supersaturation (c-c*) achieved for an equivalent permeate mass at the outset of permeation are comparable (e.g. see data at intercept of y-axis), whereas an increase in supersaturation rate achieved a greater supersaturation (c-c* 0.021 for 37HF, versus 0.004 for 3HF) prior to nucleation within the metastable solution. Despite some slight oscillation within the developed supersaturation profile, three general trends are observed: (i) preliminary primary nucleation occurs at the highest c-c* that has been achieved up to that point for the specific supersaturation rate; (ii) a modest decline in supersaturation occurs shortly after primary nucleation, indicating the consumption of supersaturation within the nucleation process [27]; and (iii) following primary nucleation, a distinct supersaturation trajectory is observed dependent upon the supersaturation rate applied [10,27]. The supersaturation profiles in the film and bulk solution are comparable in shape since the supersaturation rate is primarily determined by the relative increase in membrane area, but the distinction in trajectories is particularly evident within the film due to the higher c-c* that is developed through concentration and temperature polarisation [19]. Specifically, at the lowest supersaturation rate, c-c* gradually declined following the first primary nucleation event, whereas for the highest supersaturation rate, c-c* progressively increased over time. Since supersaturation provides the driving force for both nucleation and crystal growth [10,23], is it postulated that these different trajectories across the MSZW following induction will determine the extent to which primary and secondary nucleation occur, and the competition between nucleation and crystal growth mechanisms [29,48,49].

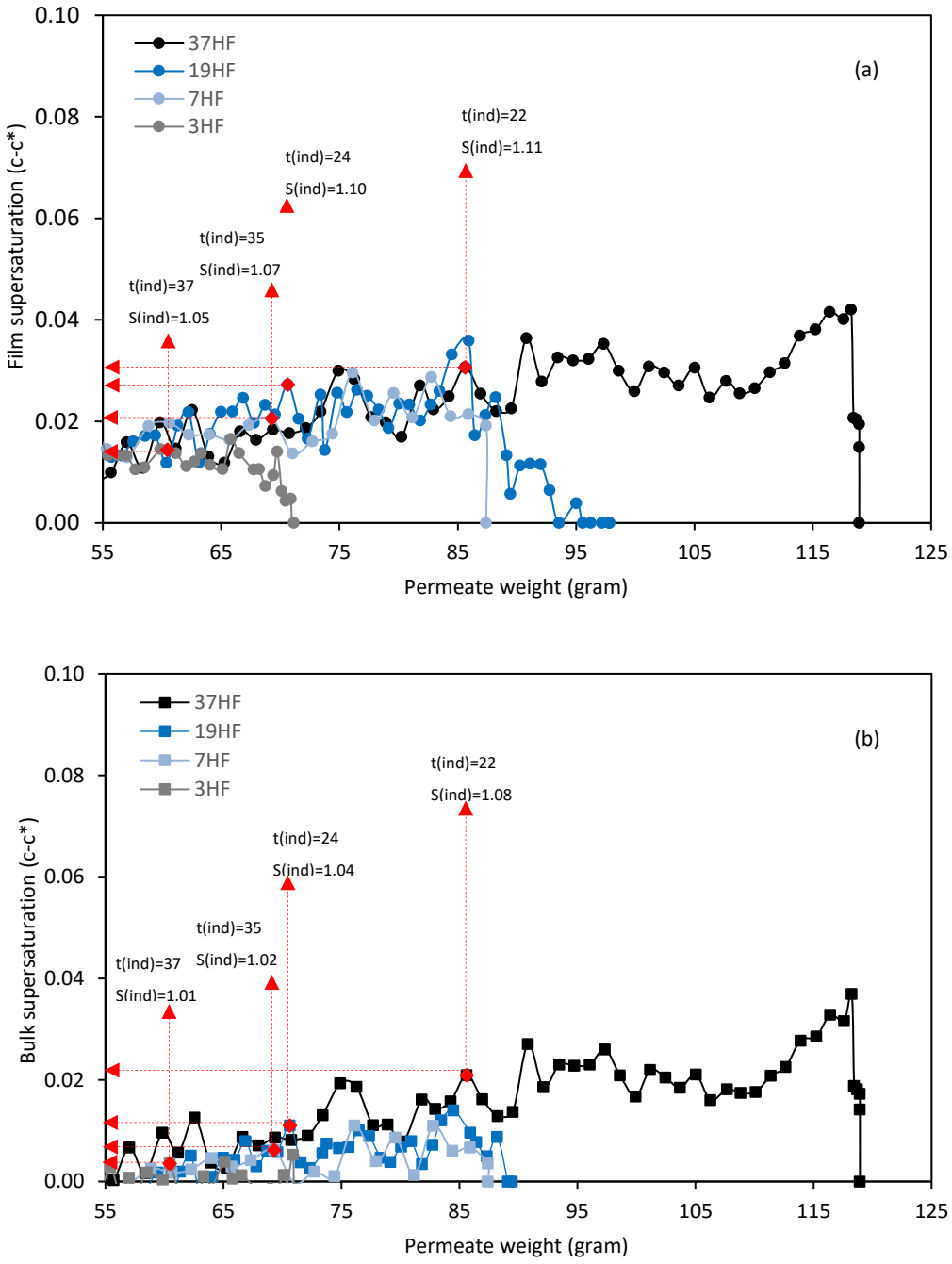

Figure 4.10 *Supersaturation profiles that develop before and after the initial primary nucleation event (induction), based on conductivity mass balance for: (a) boundary layer (or film) concentration; and (b) bulk solution concentration. Conditions: Tbulk 55±1°C; ΔT 20±2°C; initial NaCl concentration, 23.9 Wt.%; feed and permeate velocity, 0.06 m* s^{-1}.

4.3.3 Supersaturation trajectory determines crystal size, size distribution and morphology

The decline in solute concentration observed just after the onset of nucleation, implies an increase in total crystal surface area, indicating that crystalline particle growth is occurring within the system [22]. Construction of the metastable limits provides insight into the relative consumption of supersaturation following nucleation [29,50] (Figure 4.11). This repositions the system supersaturation in a region of the metastable zone between the primary nucleation limit and the solubility curve, which minimises primary nucleation and favours crystal growth, but may also incur secondary nucleation when transitioning across this domain [48,51,52]. In-line filtration increased hold-up time after induction, which can further contribute to secondary nucleation as the higher crystal number increases the probability for collision, leading to the production of fines [29,53]. Comparison of CSDs produced with and without in-line filtration (37HF) evidenced how the extension in hold-up time (14 mins) negatively skewed the CSD (Figure 4.12), indicating crystal growth is favoured over the production of fines (a response to secondary nucleation) [5,30,54]. For higher supersaturation gradients, secondary nucleation can be negligible, thus the elevated supersaturation is available to underpin crystal growth [51]. Similar growth rates of 5.31 $x10^{-8}$ and 5.05 $x10^{-8}$ m s^{-1} were observed within the systems with and without filtration respectively (Table 4.2), due to the comparable primary nucleation kinetics (and supersaturation trajectory) that were set at induction (Figure 4.4 and 4.7). However, analysis of the population balance indicates a reduction in nucleation rate with a longer hold-up time, which may result from the competition for supersaturation between nucleation and growth within a crystallising solution comprised of a considerably higher crystal density (15.9±3.9 and 7.9±0.1g respectively).

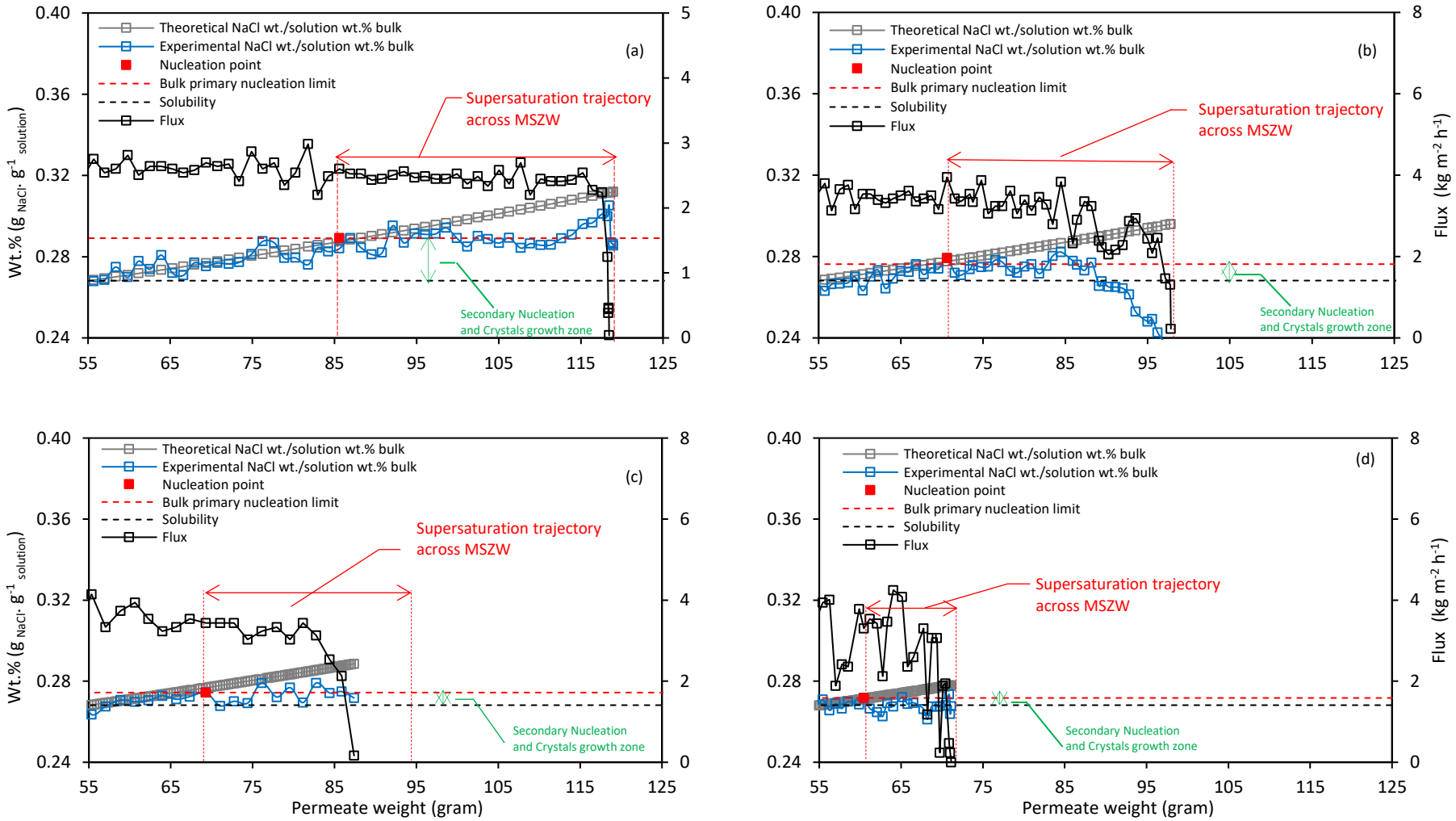

Figure 4.11 *Supersaturation trajectory during membrane distillation crystallisation, based on different supersaturation rates that are fixed by the membrane area used. In-line filtration is used in each configuration to limit deposition. The theoretical supersaturation profile is calculated based*

on conductivity mass balance assuming no consumption of NaCl for crystallisation, and compared to actual conductivity data, where the difference evidences where within the metastable zone width that nucleation and crystal growth are occurring: (a) 37HF; (b) 19HF; (c)7HF; (d) 3HF. Conditions: Tbulk 55±1°C; ∆T 20±2°C; initial NaCl concentration, 23.9 Wt.%; feed and permeate velocity, 0.06 m s^{-1}.

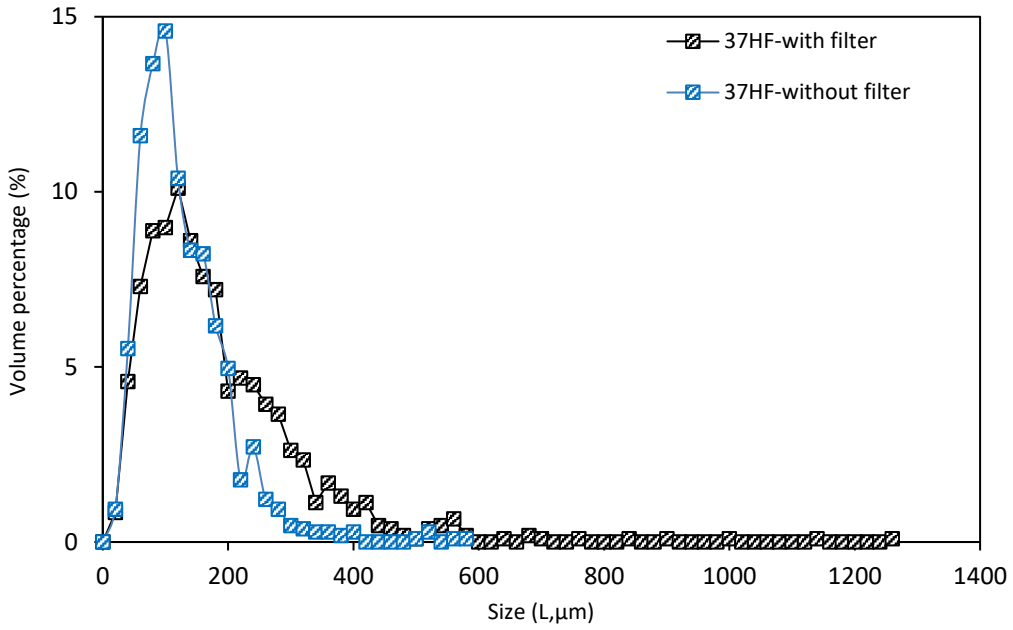

Figure 4.12 *Crystal size distributions (based on volume fraction, %) produced in the absence and presence of filtration to reduce deposition. The key difference is that in-line filtration extends residence time for crystal growth after induction which affects subsequent nucleation, crystal growth and yield. Conditions: Tbulk, 55±1°C; ΔTmembrane, 20±2°C; initial NaCl concentration, 23.9 wt.%.; feed and permeate velocity, 0.06 m* s^{-1}.

Table 4.2 *Comparison of crystallisation kinetics at different batch time from 37 HF experiment. Extension in residence time is provided by in-line filtration to reduce deposition.*

Parameters	Units	Without filter	With filter
Induction time	(min)	23±2	22±2
Concentrating rate at induction	(g.100 g^{-1} solution h^{-1})	3.02±0.09	2.83±0.14
Supersaturation at induction (c-c*) [b]	(g NaCl g^{-1} solution)	0.022±0.001	0.021±0.007
Maximum supersaturation (c-c*) [b]	(g NaCl g^{-1} solution)	0.026±0.003	0.037±0.007
ln(ΔC fm,max)	(mg NaCl g^{-1} solution)	3.45±0.07	3.37±0.12
Growth rate [a]	(x10^{-8} m s^{-1})	5.05±3.5	5.31±1.4
Nucleation rate [a]	(x10^{6} no. m^{-3} s^{-1})	22.50±0.15	1.95±1.2
Hold-up time after induction	(min)	13±1	27±2
Crystals median size (L_{50})	(µm)	100±15	142±8
Crystals yield	(g)	7.9±0.1	15.9±3.9

[a] Measured based on MSMPR theory, [b] calculated based on conductivity measurements.

For low supersaturation rates, the MSZW is narrow, and the supersaturation frequently approached the solubility limit in a region characterised as the ‘growth only’ zone [45,55]. The L_{50} of the final crystal product was 104±10µm for the lowest supersaturation rate, and progressively increased to 142±8µm for the highest supersaturation rate (Table 4.3). This contradicts classical crystallisation where fewer, larger crystals are typically produced at low supersaturation [36], and can be explained by the preferential use of supersaturation for growth at an elevated supersaturation state initiated through the higher supersaturation rate [22]. However, the supersaturation state has implications for scaling and crystal product quality (Figure 4.13). Detailed SEM imaging of the scaling layer revealed that even for a low supersaturation rate, the elevated supersaturation state in the film introduced imperfections within the crystal scaling morphology, as evidenced by hollows formed within the cubic structure (Figure 4.13a). These so called ‘hopper’ crystals are symptomatic of relatively low supersaturation conditions that are induced through unstable diffusion of molecules into the crystal lattice [56,57]. At higher supersaturation rates, SEM imaging confirmed less scaling, whereas the extent of hollows apparent in the crystal morphology appear exacerbated by the increase in local supersaturation. This is because higher supersaturation levels occur at edges and corners, rather than faces, subsequently generating these occlusions that can physically trap impurities, reducing product purity (Figure 4.13b) [56,60]. Distinct morphology was evident for the crystal product formed within the crystalliser within the same conditions, permitting a characteristic cubic form with smooth surfaces and facets, suggesting that the lower supersaturation rate and supersaturation level that manifests in the bulk solution, enables sufficient time for more homogeneous molecular diffusion into the crystal lattice [23]. This was coupled with a lower coefficient of variation (CV, 48%), indicating narrowing of the distribution around the mean size. Consequently, segregating crystal growth into the bulk solution in MDC can provide greater control over product quality, while independently promoting conditions that favour primary nucleation. However, cementation and aggregation are also indicated in the crystal product (Figure 4.13c) which occur at high primary nucleation rates through collisions in the significant population of small crystals, and may be unfavourable to product quality [61,62].

Table 4.3 *Crystallisation kinetics across different supersaturation profiles developed when using in-line filter configuration.*

Fibre No.	Induction time (min)	Concentrating rate at induction ($g.100g^{-1}$ Solution h^{-1})	Supersaturation at induction (c-c*) (g NaCl g^{-1} solution)[a]	Crystals yield (g)	Maximum Supersaturation (c-c*) (g NaCl g^{-1} solution)[a]	$\ln(\Delta C_{fm,max})$ (mg NaCl g^{-1} Solution)	Hold-up time after induction (min)	Median (L_{50}) (μm)[b]	Coefficient of variation (CV, %)
37	22±2	2.83±0.14	0.021±0.007	15.0±3.9	0.037±0.007	3.37±0.09	27±2	142±8	0.63±0.01
19	24±1	2.42±0.08	0.011±0.002	11.5±0.7	0.014±0.004	3.23±0.32	33±9	133±9	0.48±0.02
7	35±2	1.26±0.11	0.006±0.001	10.1±2.9	0.011±0.002	3.15±0.05	87±6	102±6	0.55±0.01
3	37±1	0.43±0.06	0.004±0.001	9.3±4.9	0.005±0.0003	3.04±0.02	89±10	104±10	0.69±0.03

[a] Calculated based on conductivity measurements, [b] Standard error was calculated based on differences in triplicate measurements.

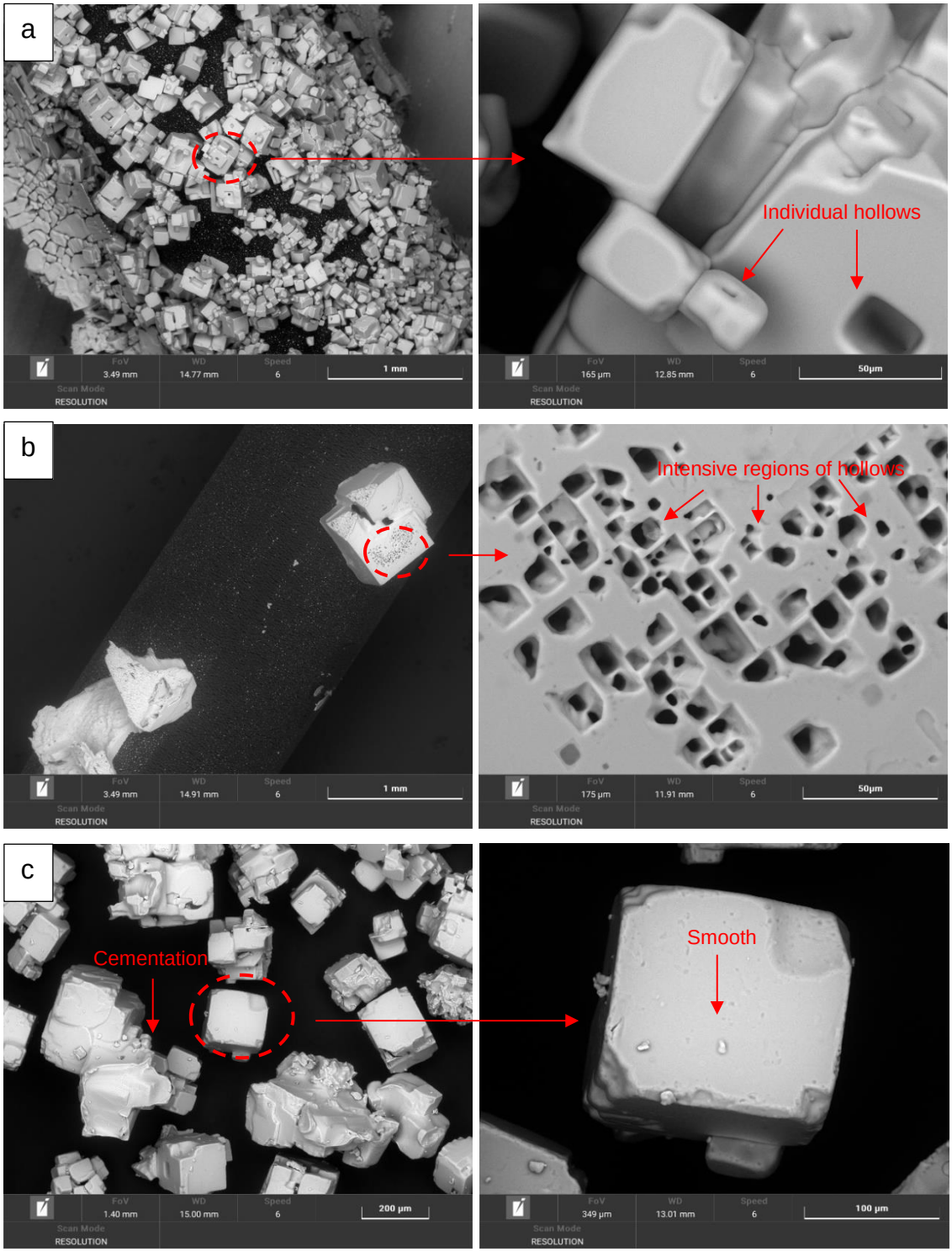

Figure 4.13 *Scanning electron microscopy (SEM) of produced crystals at the membrane surface and from the bulk solution: (A) 7HF, with filter device, sampled from membrane (c/c* 1.07, residence time after induction, 89 min); (B) 19HF, with filter device, sampled from membrane (c/c* 1.10, residence time after induction, 33 min); (C) 19HF, sampled from bulk solution in feed vessel, upstream of in-line filter configuration (c/c* 1.04,*

residence time after induction, 33 min). Distinct crystal growth patterns observed at membrane surface dependent on supersaturating rate, and when crystals are produced in the bulk solution, evidencing the potential to improve crystal morphology.

At the highest supersaturation rate, supersaturation exceeded the primary nucleation threshold on several occasions (PNT, which is the supersaturation level at which primary nucleation first occurred) (Figure 4.14). While analysis of the population balance implied that extension of the residence time favoured growth over nucleation, by exceeding the PNT, it can be inferred that the free energy barrier was sufficiently reduced to initiate further primary nucleation events [8,36,63]. Peaks up to a value of $\Delta c/c^*_{pnt}$ 0.006 were not observed to disturb flux, whereas flux was noted to decline shortly following a PNT peak exceeding 0.015. While supersaturation peaks exceeding the PNT were fewer in number, and lower in value for lower supersaturation rates, the stage three decline in flux was also preceded by a peak in supersaturation which exceeded the PNT (Table 4.4). It is therefore suggested that stage 3 flux decline is primarily a response to further primary nucleation events, where higher nucleatin rates elicited at supersaturation>PNT can be detrimental to sustained operation. The relative insensitivity of flux for 37 HF (Figure 4.14), implies that by broadening MSZW to favour homogeneous primary nucleation, membrane distillation crystallisation is more resilient to new primary nucleation events characterised by small transient PNT peaks. Consumption of supersaturation for nucleation was greatest following the first primary nucleation event (t=0, Figure 4.14), whereas the consumption of supersaturation following subsequent PNT peaks was less, despite achieving higher levels of supersaturation. This can be attributed to the competition between nucleation and growth of the existing crystal phase. By shortening the residence time for crystal growth (reducing the particle population), more supersaturation will be consumed in the creation of new nuclei which will lower the system supersaturation. In addition to mitigating stage 3 flux decline, closer regulation of supersaturation can also reduce the effect of aggregation and cementation within the final product.

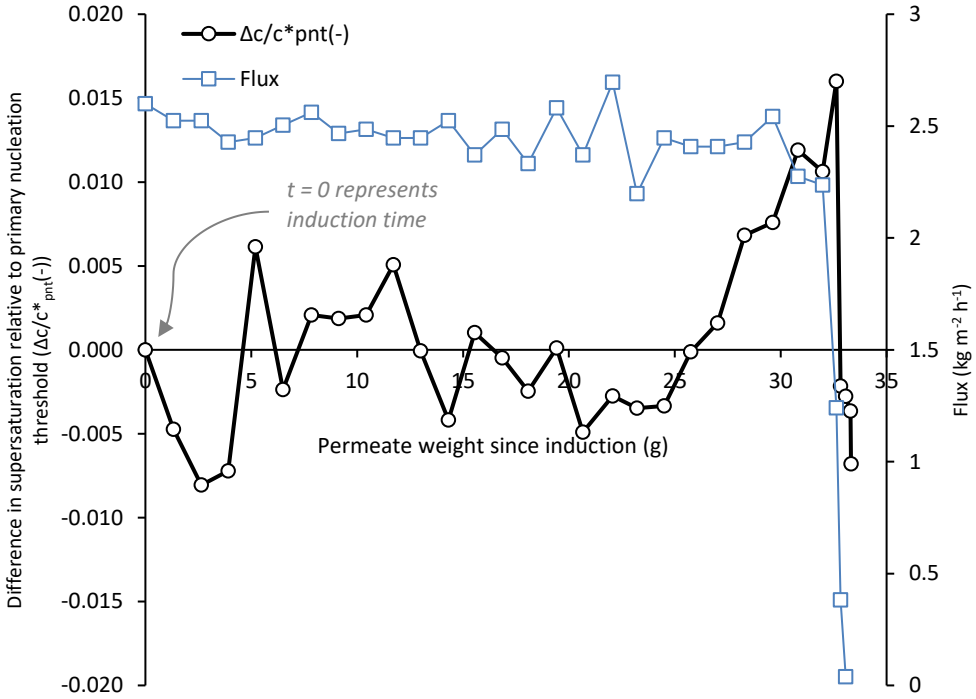

Figure 4.14 *Indicative illustration for how stage-three flux decline is seemingly dependent upon the system exceeding the supersaturation threshold for primary nucleation. 37 HF configuration used for illustration. Conditions: Tbulk 55±1°C; ΔT 20±2°C; initial NaCl concentration, 23.9 Wt.%; feed and permeate velocity, 0.06 m s^{-1}.*

Table 4.4 *Primary nucleation exceedance (PNT) pattern of different supersaturation profiles*

Fibre No.	$\Delta c/c^*_{(pnt)}$[a] (-)	$\Delta t(t_{stage3}-t_{PNTexceedence})$[b] (min)	$\Delta t(t_{stage3}-t_{ind})$[c] (min)
3	0	0	30
7	0.003	3	33
19	0.003	1	16
37	0.016	4	25

[a]The extent of supersaturation that was achieved in excess of the PNT at stage 3 flux failure; [b]time lag between previous PNT exceedance and start of flux failure; [c]operating time between start of stage 3 flux decline and induction time.

4.4 Conclusions

This study has demonstrated how facile supersaturation control strategies can be instigated within membrane crystallisation to enhance the governance over

nucleation and crystal growth kinetics following induction. An increase in membrane area, provides an adjustment of supersaturation rate and the nucleation kinetics, as evidenced by achievement of a broader metastable zone and shorter induction time. Consequently, the area to volume ratio can be used as a method to adjust the nucleation kinetics which is a facet unique to membrane crystallisation. While the interstitial fibre spacing was sustained between membranes, the increased packing density (53.9% max.) was not observed to increase scaling, deposition or entrapment of the crystal phase, indicating commercially relevant membrane geometries are likely to be exploitable within this application. However, using an ‘off-bottom just-suspended’ agitation rate within the crystalliser, complemented with in-line filtration, has been shown beneficial to minimise deposition, and to sustain a consistent supersaturation rate following induction. This permits an increase in crystal size and yield (crystals density), and the consistency in supersaturation rate following induction can be used to offset the consumption of supersaturation for nucleation and growth, to sustain the system within specific regions of the metastable zone. While increasing supersaturation rate mitigated scaling, crystal morphology was negatively affected by diffusion-limited growth within the elevated region of supersaturation contained within the boundary layer. However, crystal morphology (habit and occlusions) was markedly improved within the crystalliser ostensibly due to the lower region of supersaturation. Consequently, we propose that nucleation can be decoupled with membrane crystallisation to facilitate shorter induction times and higher nucleation rates, reducing process scale and throughput, with growth subsequently controlled downstream in a region of supersaturation that is more conducive to well-regulated growth. Retention of the crystal phase within the bulk reactor extended the residence time for crystallisation, however, stage-three flux decline was still observed and was related to the exceedance of the primary nucleation threshold. While the explicit mechanism is not yet clear, this preliminary evidence provides a basis on which to found mitigation strategies to further extend operation. Scale up of classical evaporators is challenging since the surface area for heat and mass transfer are

independent and do not linearly scale, mixing within the evaporative domain is difficult to characterise, and as such the supersaturation rate is difficult to control. This study therefore demonstrates supersaturation control strategies that cannot easily be developed within classical crystallisers, to provide greater control over the kinetics of nucleation and crystal growth. The regulation of supersaturation by membrane area following induction, is accounted for by the simultaneous heat and mass transfer that occur across a fixed interfacial area and provide early evidence that membrane crystallisation may offer an inherently scalable solution to evaporative crystallisation, affording richer opportunity for kinetic control.

4.5 Acknowledgements

This research was financially supported by European Research Council Starting Grant, ‘Sustainable chemical alternatives for reuse in the circular economy’ (StG, SCARCE, 714080).

4.6 Appendix A

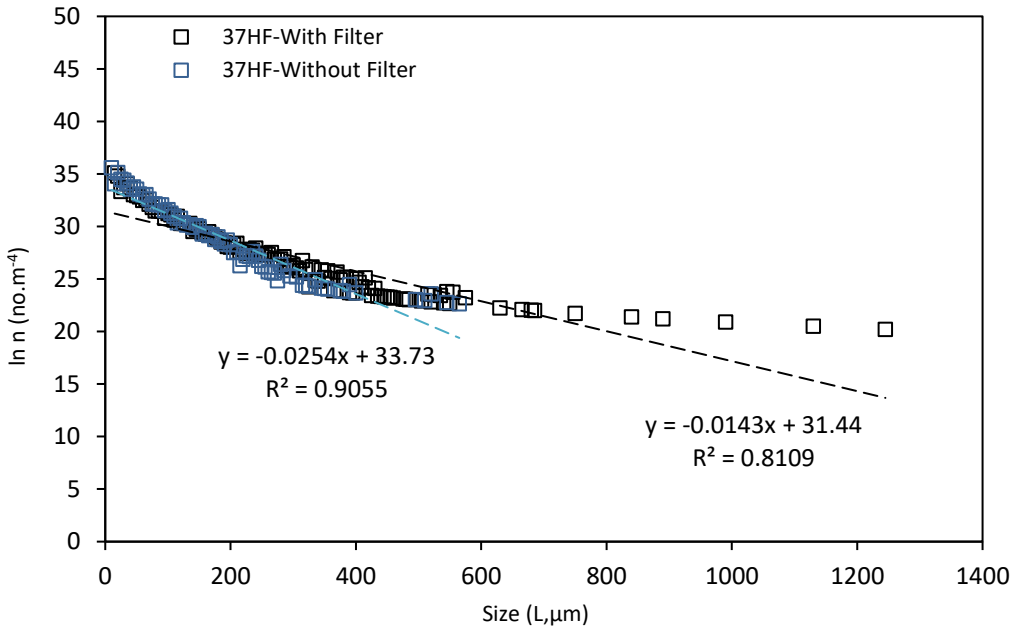

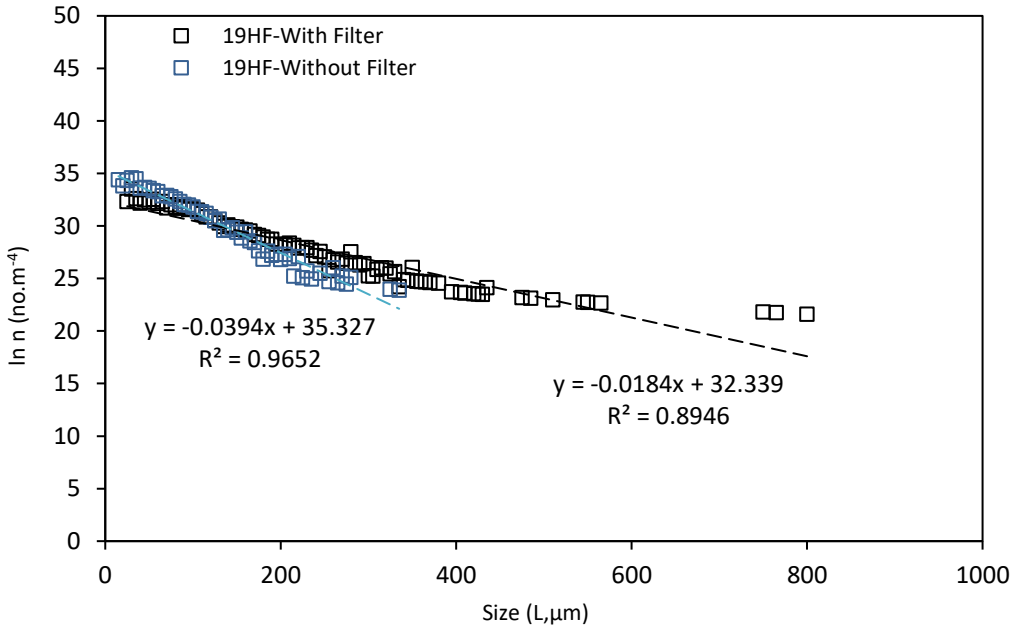
19HF-With Filter
19HF-Without Filter
y = -0.0394x + 35.327
R² = 0.9652
y = -0.0184x + 32.339
R² = 0.8946
ln n (no.m-4)
Size (L,µm)
0
5
10
15
20
25
30
35
40
45
50
0
200
400
600
800
1000

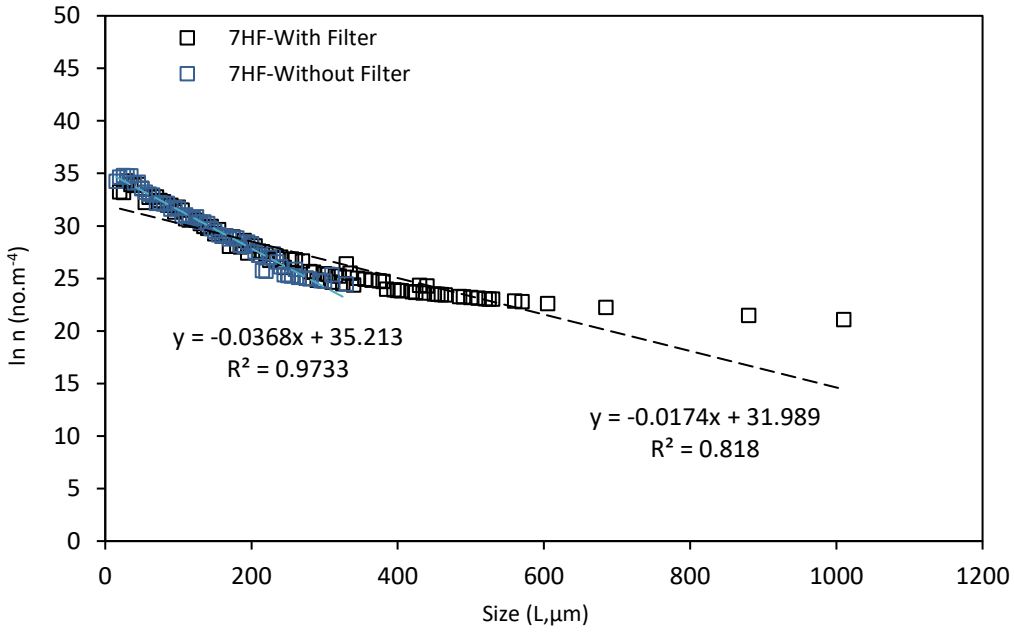
7HF-With Filter
7HF-Without Filter
y = -0.0368x + 35.213
R² = 0.9733
y = -0.0174x + 31.989
R² = 0.818
ln n (no.m-4)
Size (L,µm)
0
5
10
15
20
25
30
35
40
45
50
0
200
400
600
800
1000
1200

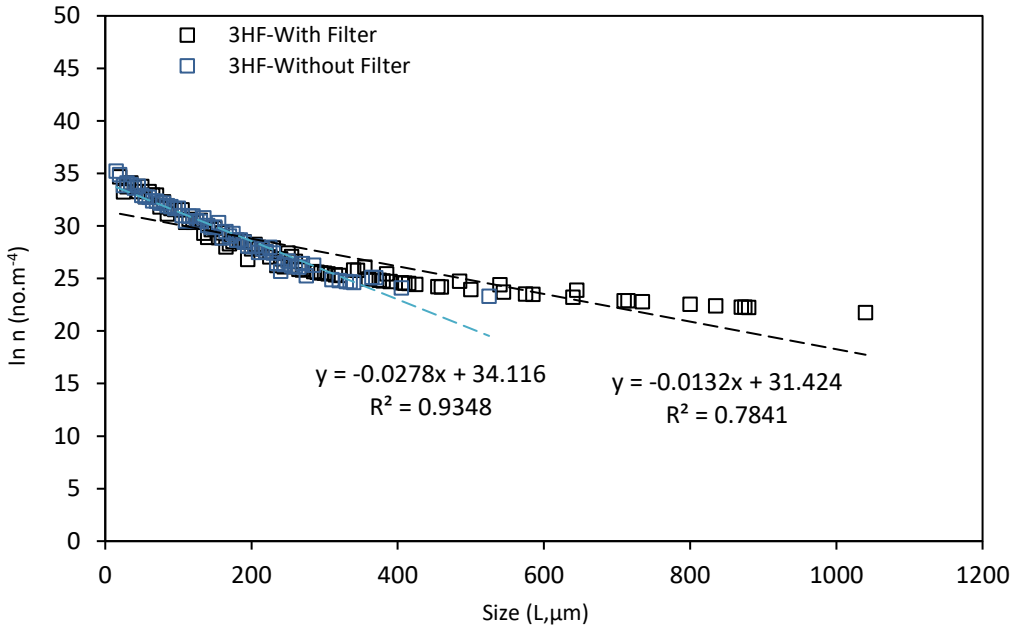

Figure A 4-1 *Population density ln n(no.m^{-4}) versus crystal size (L,µm) plot based on MSMPR model for nucleation rate and crystal growth calculation.*

4.7 References

[1] E. Drioli, G. Di Profio and E. Curcio, Progress in membrane crystallization, Curr. Opin. Chem. Eng. 1 (2012) 178–182.

[2] X. Jiang, L. Tuo, D. Lu, B. Hou, W. Chen and G. He, Progress in membrane distillation crystallization: Process models, crystallization control and innovative applications, Front. Chem. Sci. Eng. 11 (2017) 647–662.

[3] J. Kim, J. Kim and S. Hong, Recovery of water and minerals from shale gas produced water by membrane distillation crystallization, Water Res. 129 (2018) 447–459.

[4] G. Di Profio, E. Curcio and E. Drioli, Supersaturation control and heterogeneous nucleation in membrane crystallizers: Facts and perspectives, Ind. Eng. Chem. Res. 49 (2010) 11878–11889.

[5] G. Chen, Y. Lu, W.B. Krantz, R. Wang and A.G. Fane, Optimization of operating conditions for a continuous membrane distillation crystallization process with zero salty water discharge, J. Memb. Sci. 450 (2014) 1–11.

[6] S. Meng, Y. Ye, J. Mansouri and V. Chen, Crystallization behavior of salts during membrane distillation with hydrophobic and superhydrophobic capillary membranes, J. Memb. Sci. (2015) 165–176.

[7] A. Jones, S. Rigopoulos and R. Zauner, Crystallization and precipitation engineering, Comput. Chem. Eng. 29 (2005) 1159–1166.

[8] X. Jiang, X. Ruan, W. Xiao, D. Lu and G. He, A novel membrane distillation response technology for nucleation detection, metastable zone width measurement and analysis, Chem. Eng. Sci. 134 (2015) 671–680.

[9] E. Chabanon, D. Mangin, C. Charcosset, Membranes and crystallization processes: State of the art and prospects, J. Memb. Sci. 509 (2016) 57–67.

[10] G. Di Profio, S. Tucci, E. Curcio and E. Drioli, Controlling polymorphism with membrane-based crystallizers: Application to form i and II of paracetamol, Chem. Mater. 19 (2007) 2386–2388.

[11] Y. Choi, G. Naidu, L.D. Nghiem, S. Lee and S. Vigneswaran, Membrane distillation crystallization for brine mining and zero liquid discharge:

Opportunities, challenges, and recent progress, Environ. Sci. Water Res. Technol. 5 (2019) 1202–1221.

[12] M. Lenka and D. Sarkar, Determination of metastable zone width and nucleation kinetics for combined cooling and antisolvent crystallization of L-asparagine monohydrate in water-isopropanol mixture, J. Cryst. Growth. 501 (2018) 66–73.

[13] S. Karthika, T.K. Radhakrishnan and P. Kalaichelvi, Measurement of nucleation rate of ibuprofen in ionic liquid using induction time method, J. Cryst. Growth. 521 (2019) 55–59.

[14] K. Sangwal, On the interpretation of metastable zone width in anti-solvent crystallization, Cryst. Res. Technol. 45 (2010) 909–919.

[15] L. Zhou, Z. Wang, M. Zhang, M. Guo, S. Xu and Q. Yin, Determination of metastable zone and induction time of analgin for cooling crystallization, Chinese J. Chem. Eng. 25 (2017) 313–318.

[16] R.A. Bueno and D. Version, Crystallization of Active Pharmaceutical Ingredients in the Presence of Heterosurfaces, (2018) 32–48.

[17] E. Curcio, E. Fontananova, G. Di Profio and E. Drioli, Influence of the structural properties of poly(vinylidene fluoride) membranes on the heterogeneous nucleation rate of protein crystals, J. Phys. Chem. B. 110 (2006) 12438–12445.

[18] G. Di Profio, E. Curcio, S. Ferraro, C. Stabile and E. Drioli, Effect of supersaturation control and heterogeneous nucleation on porous membrane surfaces in the crystallization of L-glutamic acid polymorphs, Cryst. Growth Des. 9 (2009) 2179–2186.

[19] T. Horseman, Y. Yin, K.S. Christie, Z. Wang, T. Tong and S. Lin, Wetting, Scaling, and Fouling in Membrane Distillation: State-of-the-Art Insights on Fundamental Mechanisms and Mitigation Strategies, ACS ES&T Eng. 1 (2021) 117–140.

[20] X. Jiang, Y. Niu, S. Du and G. He, Membrane crystallization: Engineering the crystallization via microscale interfacial technology, Chem. Eng. Res. Des. 178 (2022) 454–465.

[21] N. Kubota, A new interpretation of metastable zone widths measured for unseeded solutions, J. Cryst. Growth. 310 (2008) 629–634.

[22] H. Takiyama, Supersaturation operation for quality control of crystalline particles in solution crystallization, Adv. Powder Technol. 23 (2012) 273–278.

[23] Y. Gao, T. Zhang, Y. Ma, F. Xue, Z. Gao, B. Hou and J. Gong, Application of pat-based feedback control approaches in pharmaceutical crystallization, Crystals. 11 (2021) 1–27.

[24] Mitsuko Fujiwara, Pui Shan Chow, David L. Ma, and Richard D. Braatz, Paracetamol Crystallization Using Laser Backscattering and ATR-FTIR Spectroscopy: Metastability, Agglomeration, and Control, Crystal Growth Des. 2 (2002), 363–370.

[25] S.G. Agrawal and A.H.J. Paterson, Secondary Nucleation: Mechanisms and Models, Chem. Eng. Commun. 202 (2015) 698–706.

[26] M.L. Briuglia, J. Sefcik and J.H.T. Horst, Measuring Secondary Nucleation through Single Crystal Seeding, Cryst. Growth Des. 19 (2019) 421–429.

[27] D. Duffy, M. Barrett and B. Glennon, Novel, calibration-free strategies for supersaturation control in antisolvent crystallization processes, Cryst. Growth Des. 13 (2013) 3321–3332.

[28] M.T. Chan, A.G. Fane, J.T. Matheickal and R. Sheikholeslami, Membrane distillation crystallization of concentrated salts - Flux and crystal formation, J. Memb. Sci. 257 (2005) 144–155.

[29] F. Edwie and T.S. Chung, Development of simultaneous membrane distillation-crystallization (SMDC) technology for treatment of saturated brine, Chem. Eng. Sci. 98 (2013) 160–172.

[30] M.C. Sparenberg, S. Chergaoui, V. Sang Sefidi and P. Luis, Crystallization control via membrane distillation-crystallization: A review, Desalination. 519 (2022) 115315.

[31] X. Yang, R. Wang, L. Shi, A.G. Fane and M. Debowski, Performance improvement of PVDF hollow fiber-based membrane distillation process, J. Memb. Sci. 369 (2011) 437–447.

[32] A. Ali, J.H. Tsai, K.L. Tung, E. Drioli and F. Macedonio, Designing and optimization of continuous direct contact membrane distillation process, Desalination. 426 (2018) 97–107.

[33] J. Phattaranawik, R. Jiraratananon and A.G. Fane, Heat transport and membrane distillation coefficients in direct contact membrane distillation, J. Memb. Sci. 212 (2003) 177–193.

[34] G. Chen, Y. Lu, X. Yang, R. Wang and A.G. Fane, Quantitative study on crystallization-induced scaling in high-concentration direct-contact membrane distillation, Ind. Eng. Chem. Res. 53 (2014) 15656–15666.

[35] M. Tomaszewska and M. Gryta, A.W. Morawski, Study on the concentration of acids by membrane distillation, J. Memb. Sci. 102 (1995) 113–122.

[36] F. Edwie and T.S. Chung, Development of hollow fiber membranes for water and salt recovery from highly concentrated brine via direct contact membrane distillation and crystallization, J. Memb. Sci. 421– 422 (2012) 111–123.

[37] K. Sangwal, A novel self-consistent Nývlt-like equation for metastable zone width determined by the polythermal method, Cryst. Res. Technol. 44 (2009) 231–247.

[38] K.J. Kim, Crystal growth in drowning-out crystallization using a T-mixer, Chem. Eng. Technol. 29 (2006) 1267–1272.

[39] R. Thanedgunbaworn, R. Jiraratananon and M.H. Nguyen, Shell-side mass transfer of hollow fibre modules in osmotic distillation process, J. Memb. Sci. 290 (2007) 105–113.

[40] L. Martínez, Comparison of membrane distillation performance using different feeds, Desalination. 168 (2004) 359–365.

[41] K.Y. Wang, S.W. Foo and T.S. Chung, Mixed matrix PVDF hollow fiber membranes with nanoscale pores for desalination through direct contact membrane distillation, Ind. Eng. Chem. Res. 48 (2009) 4474–4483.

[42] A. Alkhudhiri, N. Darwish and N. Hilal, Membrane distillation: A comprehensive review, Desalination. 287 (2012) 2–18.

[43] J.W. Mullin, Crystal growth, in: J.W. Mullin (Ed.), Cryst. (Fourth Ed., Fourth Edi, Butterworth-Heinemann, Oxford, (2001) 216–288.

[44] L. Nemdili, O. Koutchoukali, F. Mameri, I. Gouaou, M.S. Koutchoukali and J. Ulrich, Crystallization study of potassium sulfate-water system, metastable zone width and induction time measurements using ultrasonic, turbidity and 3D-ORM techniques, J. Cryst. Growth. 500 (2018) 44–51.

[45] M. Lenka and D. Sarkar, Determination of metastable zone width, induction period and primary nucleation kinetics for cooling crystallization of L-asparaginenohydrate, J. Cryst. Growth. 408 (2014) 85–90.

[46] Y. Liu, T. Horseman, Z. Wang, H.A. Arafat, H. Yin, S. Lin and T. He, Negative Pressure Membrane Distillation for Excellent Gypsum Scaling Resistance and Flux Enhancement, Environ. Sci. Technol. 56 (2022) 1405–1412.

[47] S. Datta and D.J.W. Grant, Effect of supersaturation on the crystallization of phenylbutazone polymorphs, Cryst. Res. Technol. 40 (2005) 233–242.

[48] M.R.A. Bakar, Z.K. Nagy, A.N. Saleemi and C.D. Rielly, The Impact of Direct Nucleation Control on Crystal Size Distribution in Pharmaceutical, Cryst. Growth Des. 3 (2009) 1378–1384.

[49] I. Ostergaard, B. Szilagyi, H.L. De Diego, H. Qu and Z.K. Nagy, Polymorphic Control and Scale-Up Strategy for Antisolvent Crystallization Using Direct Nucleation Control, Cryst. Growth Des. 20 (2020) 2683–2697.

[50] M. Porru and L. Özkan, Monitoring of Batch Industrial Crystallization with Growth, Nucleation, and Agglomeration. Part 1: Modeling with Method of Characteristics, Ind. Eng. Chem. Res. 56 (2017) 5980–5992.

[51] M. Barrett, M. Mcnamara, H. Hao, P. Barrett and B. Glennon, Chemical Engineering Research and Design Supersaturation tracking for the development , optimization and control of crystallization processes, Chem. Eng. Res. Des. 88 (2010) 1108–1119.

[52] J. Hou, S. Wu, R. Li, W. Dong and J. Gong, The induction time, interfacial energy and growth mechanism of maltitol in batch cooling crystallization, Cryst. Res. Technol. 47 (2012) 888–895.

[53] T.E. Fakatselis, Residence Time Optimization in Continuous Crystallizers, Cryst. Growth Des. 2 (2002) 375–379.

[54] S.Y. Misyura, Evaporation and heat transfer of aqueous salt solutions during crystallization, Appl. Therm. Eng. 139 (2018) 203–212.

[55] X. Ni and A. Liao, Effects of cooling rate and solution concentration on solution crystallization of L-glutamic acid in an oscillatory baffled crystallizer, Cryst. Growth Des. 8 (2008) 2875–2881.

[56] D. Pettit and P. Fontana, Comparison of sodium chloride hopper cubes grown under microgravity and terrestrial conditions, Npj Microgravity. 5 (2019) 1–7.

[57] M.A. Lovette, A.R. Browning, D.W. Griffin, J.P. Sizemore, R.C. Snyder and M.F. Doherty, Crystal shape engineering, Ind. Eng. Chem. Res. 47 (2008) 9812–9833.

[58] R. Brooks, A.T. Horton and J.L. Torgesen, Occlusion of mother liquor in solution-grown crystals, J. Cryst. Growth. 2 (1968) 279–283.

[59] M. Akrap, N. Kuzmanić and J. Prlić-Kardum, Effect of mixing on the crystal size distribution of borax decahydrate in a batch cooling crystallizer, J. Cryst. Growth. 312 (2010) 3603–3608.

[60] L.M. Terdenge, J.A. Kossuch, G. Schembecker and K. Wohlgemuth, Potential of gassing crystallization to control the agglomeration degree of crystalline products, Powder Technol. 320 (2017) 386–396.

[61] K. Sangwal, E. Mielniczek-Brzóska and S. Barylska, Solubility of ammonium oxalate in water-acetone mixtures and metastable zone width of their solutions, Chem. Eng. Res. Des. 92 (2014) 491–499.

5 Discussion

The chapters in this thesis have collectively provided an intellectual framework towards a better understanding of the fundamental crystallisation parameters that govern the sustainable and reproducible design of crystallisation processes within membrane distillation crystallisation (MDC) systems. We proposed supersaturation rate as a primary regulator to foster a wide set of crystallisation kinetics for improved crystal properties, in which different crystallisation perspectives were explored throughout to provide insight into the crystallisation kinetics control and scaling minimisation strategies, as follows:

5.1 MDC can be described through classical nucleation theory (CNT)

Many membrane distillation crystallisation (MDC) studies indicate that heterogeneous nucleation is more likely to occur initially within the MDC process compared to homogeneous nucleation [1,2]. The water vapour flux is considered as the surrogate parameter that regulates supersaturation rate and determines the onset of nucleation [3]. In this thesis, the rate of supersaturation within the crystalline solution is considered the key criterion to govern the onset of nucleation, which is fundamentally distinct from the start of irreversible flux decline [4]. This provides a summation of multiple parameters in a single term that extend rational system design beyond simply normalised membrane flux.

The crystallisation of NaCl is critical for brine management due to its prevalence in various waste streams, which makes membrane distillation exploitable for both Minimal Liquid Discharge (MLD) and Zero Liquid Discharge (ZLD) applications. Since NaCl is considered a highly soluble aqueous salt with a low interfacial energy between the NaCl crystal and the surrounding solution, the relative volume-free energy (and hence supersaturation) that is developed during crystallisation is small compared to those of high interfacial energy such as $CaSO_4$ and $CaCO_3$ [5]. Consequently, NaCl can exhibit a greater propensity for scaling compared to commonly known scalants like $CaSO_4$ and $CaCO_3$, which have limited solubility and depend on a higher volume free energy (higher supersaturation degree) to surpass the solubility limit and reduce the critical

energy barrier for nucleation [6]. Compounds like $CaSO_4$ have therefore been observed to form under high nucleation rates but with relatively small particle sizes, where this characteristic has a higher likelihood of deposition over adhesion [7]. This is supported by the observations of Warsinger et al. [8], in which scaling (via deposition) of $CaCO_4$ was shown to be mitigated once an in-line filter is placed in the system. While the NaCl system relies more on reducing the interfacial energy to lower the energy barrier for nucleation, the method adopted in this study to minimise scaling can be considered effective for all aqueous salts which are more disposed to scaling through deposition rather than adhesion, making the implemented approach applicable to mitigate scaling in a broader range of salt systems. This latter contribution is critical to various membrane crystallisation configurations as this directly determines the extent of hold-up time following nucleation before flux distortion, where there is an opportunity to enhance control over nucleation and effectively manage the growth of the produced crystals in the crystalline bulk. This was evidenced in Chapter 4, where the implementation of in-line filtration effectively reduces scaling caused by crystal deposition and supports a consistent supersaturation rate following nucleation, offering improved control over the nucleation and growth mechanisms. While the interfacial energy determines the likelihood of membrane scaling according to CNT, lower interfacial energy salt like NaCl will require a heterogeneous host more than salts with higher interfacial energy to initiate nucleation, where the nucleation sites can lower the energy barrier for nucleation [4]. This will exacerbate membrane scaling by adhesive growth, but it can be avoided by increasing the thermodynamic driving force (supersaturation) to balance the volume-free energy (ΔGv) and the surface-free energy (ΔGs). This allows the system to cross the critical energy barrier for nucleation in a homogeneous manner, where nucleation initiates within the bulk rather than on the membrane (Chapter 1). However, this transition towards homogeneous nucleation by increasing the supersaturation rate to initiate nucleation at high supersaturation degree is often linked to advanced scaling in membrane crystallisation literature [9,10]. This contradicts CNT, which suggests that when

high supersaturation at induction is achieved, the system is less dependent on heterogeneous catalysts to initiate nucleation.

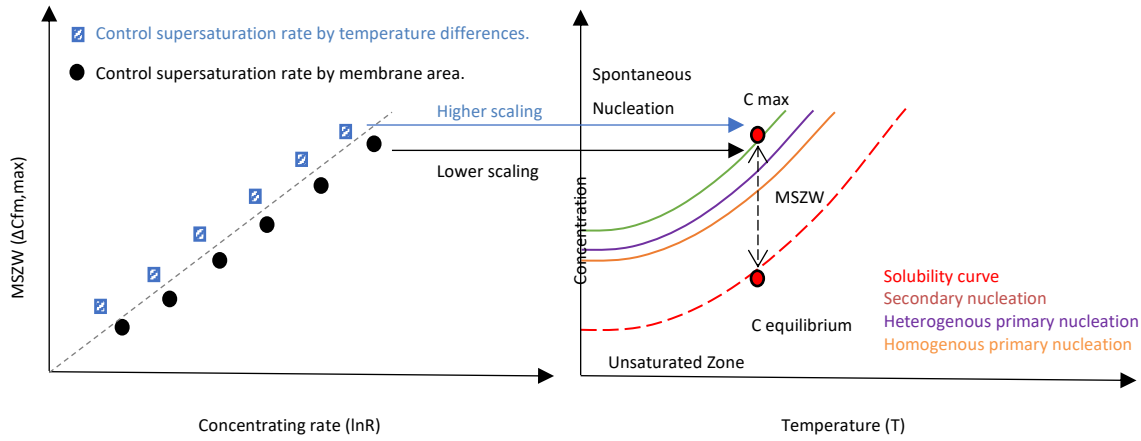

Figure 5.1 *Similar nucleation mechanisms during the transition across MSZW using different supersaturation rate parameters showed distinct scaling behaviour due to different boundary layer characteristics between two approaches.*

The contradiction arises from adjusting the supersaturation rate by membrane area rather than boundary layer in this work, which is not the case when the supersaturation rate is modified by ΔT/flux where supersaturation rate, solute concentration, and temperature polarisation are changed simultaneously (Figure 5.1). Therefore, adjusting the supersaturation rate by membrane area enables a closer alignment between bulk and film concentrations, which would favour bulk nucleation (Chapter 1). However, when the supersaturation rate is modified using ΔT/flux, there are significant differences in concentrations between the bulk and film, which creates a favourable environment for homogeneous nucleation within the supersaturated pores, promoting the formation of crystals within the membrane pores. Consequently, the study showed that operating at high supersaturation by increasing membrane area can decouple surface nucleation (scaling) from that in bulk, which would enable membrane distillation technology to yield a broader set of crystallisation trajectories under minimum scaling conditions and better control of bulk crystal phase.

5.2 Controlling crystal size, size distribution, and morphology in MDC

The induction time and supersaturation were measured to relate the kinetics of nucleation to the crystallisation conditions that would control growth phase in both the bulk solution and the film layer, which has rarely been discussed in MDC literature [4]. In MDC, the classical method to control the driving force of supersaturation for nucleation and crystal growth is by modifying the temperature, or ΔT (membrane flux), which has been recognised to alter the heat and mass transfer mechanisms within the boundary layer [9]. This will broaden the difference in supersaturation between the membrane interface and bulk solution, where supersaturation within the membrane film is likely to be greater compared to the bulk as the supersaturation rate increases. Therefore, most MDC studies recommend operating at a lower supersaturation rate (lower region of MSZW) to avoid the higher nucleation rate associated with high supersaturation during the nucleation stage [11]. This is not the case in this study, where the supersaturation rate is controlled by the membrane area instead of boundary layer characteristics, as this provides a unique method for simultaneously increasing supersaturation in both the bulk solution and the membrane film when the supersaturation rate is increased. This provides maximum supersaturation within bulk solution to enhance crystal growth despite the higher nucleation rate. As a result, the crystal size distribution shifts right with larger mean crystal size in Chapter 1, which contradict earlier study of Edwie et al., [9] that reported smaller average crystal sizes once supersaturation rate increased by feed temperature. Additionally, the modified supersaturation rate using crystalliser volume in Chapter 2 showed an increase in MSZW in bulk, whereas the flux sustains bulk solution at comparable supersaturation to favour growth at enhanced supersaturation conditions, which resulted in a narrow size distribution compared to Chapter 1. In their study, the supersaturation at induction was greater at membrane film, which is often cited to exhibit further scaling due to oversaturation at boundary layer compared to operating at lower supersaturation rate (lower feed temperature). Whilst the high supersaturation driving force in this work imposes kinetically favoured crystallisation, which leads to nucleation and growth in a higher energetic form

(metastable form) according to Oswald's ripening rules, where nucleation is less dependent on a heterogeneous host (less scaling) and the crystal growth differs for a broader size range [12,13]. This would favour crystal morphology differences depending on the supersaturation rate used, where spiral growth was favoured at a lower supersaturation rate compared to a rough growth pattern when the rate of supersaturation was increased. Whilst initiating nucleation at high supersaturation may exhibit unfavourable size distribution (due to Ostwald ripening), modifying induction time, supersaturation, or supersaturation rate independently by multiple conditional supersaturation parameters in Chapter 2 generate different sets of nucleation and growth kinetics for better control over crystal growth (reduced Oswald's ripening effect). Using crystalliser volume to modulate the supersaturation rate at fixed membrane area allowed for moderate supersaturation within bulk solution compared to that on membrane film, which promote equivalent bulk crystal size with a narrowed size distribution. An additional measure was implemented to enhance control over crystal growth in Chapter 3 by introducing in-line filtration into the system, which effectively segregates the crystal phase into the bulk solution, providing an opportunity for continued crystal growth. This was beneficial to minimise scaling by deposition and meanwhile control crystal morphology and purity of crystals grown within bulk crystalliser. However, aggregation and cementation were observed within crystals formed on bulk which can be avoided by further control of bulk local supersaturation and subsequent nucleation rate. Importantly, the improved bulk supersaturation utilised with NaCl can be employed for poorly soluble aqueous salts ($CaSO_4$ and $CaCO_3$) that have limited ion concentrations, in which the higher supersaturation at induction can facilitate higher concentrations of solute ions to assemble and form crystals [14]. Therefore, for each of the operating conditions outlined to control the growth phase, understanding of the supersaturation parameters and their impact on boundary layer characteristics is crucial for developing controlled-growth strategies in membrane distillation crystallisation.

5.3 The potential to design MDC for sustained and reproducible crystal growth

This study has demonstrated the capability to reconcile the heat and mass transfer mechanisms and the developed nucleation and growth kinetics for better governance over the crystal phase within MDC system. The employment of an area-to-volume ratio to regulate the rate of supersaturation is evidenced in this work as a practical solution to meet the commercial requirements of high crystal yield and well-controlled crystal properties. Previous studies of membrane distillation suggested a preference for operating at a lower supersaturation rate and turbulent flow regime (higher Reynolds number) to enable a well-controlled growth phase while simultaneously reducing the likelihood of membrane scaling [9,11,15]. In this study, we demonstrated the opportunity to control nucleation and growth by utilising a laminar flow regime with a lower Reynolds number, where a higher supersaturation rate was achievable by the increased membrane area rather than temperature differences across the membrane ΔT (Chapter 1). This enables a higher supersaturation rate, which is preferable commercially (higher yield), while also causing nucleation at a higher rate, which is not always beneficial for the size of the produced crystals (Chapter 1). However, this depends on where within MSZW this nucleation is commenced (induction time) and the rate of supersaturation employed, in which control over these two parameters were evidenced to tailor the final crystal size distribution (Chapter 2). There is potential to tune the membrane module performance with a higher packing density to favour commercial geometries; however, this should be carefully designed, particularly when fibres within the module intensely increase relative to the shell side, to ensure efficient spaces between adjacent fibres to avoid a dead zone on the shell side for a better mass transfer process [16]. Additionally, enlarging the module size by increasing the shell side diameter can reduce the turbulence within the flow channel. This reduces the heat transfer rates and presents difficulties in maintaining the desired thermal boundary layer properties near the surface of the membrane, resulting in an uncontrolled supersaturation rate [17]. Likewise, as the module length or fibre length increases, the control over the heat transfer becomes more significant since the

temperature profile along the fibre undergoes changes, resulting in a differential driving force along the fibres [18]. This will not only influence the overall supersaturation rate and nucleation kinetics but also affects the residence time of the feed stream within the module and therefore the crystal phase mechanism.

However, the increased membrane length may compensate for heat transfer to decouple nucleation and crystal growth, where the supersaturation is gradually decreased along the membrane, in which the lower supersaturation levels discourage nucleation and promote crystal growth [18,19]. By segregating nucleation to specific regions of higher supersaturation (which may be close to the module inlet) (Figure 5.1), the extended membrane length will allow the supersaturation profile to be allocated within MSZW to avoid excessive nucleation within the solution for enhanced crystal size and size distribution. Such a processing method (membrane continuous flow) can be beneficial in industrial applications as it accommodates the consistent hydrodynamics and well-defined membrane area provided by the membrane to offer greater control over the supersaturation rate and kinetics of nucleation and crystal growth to achieve the desired crystal properties. Conventionally, batch crystallisation has been favoured in industrial settings due to its adaptability to diverse custom design needs and its capability to produce a narrower crystal size distribution, which simplifies filtration and drying processes. Chan et al. [1] demonstrated that operating MDC in batch mode presents a relatively narrow size distribution, which aligns with most MDC studies. According to Edwie et al. [35], it was shown that adjusting the supersaturation rate, specifically through rapid or natural cooling rates, can generally be used to customise the crystal size distribution. However, achieving this level of control is not as straightforward in continuous mode due to the involvement of various factors and the complexity of nucleation and crystal growth processes. Meanwhile, the limitations of batch-to-batch variations and lower crystal yields currently confine MDC to continuous operations [20,3] . For instance, Gryta [34] demonstrated the potential to increase the crystal yield by switching from batch to continuous MDC. Therefore, establishing long-term

stable continuous MDC processes remains a significant challenge, which requires further detailed exploration in future work.

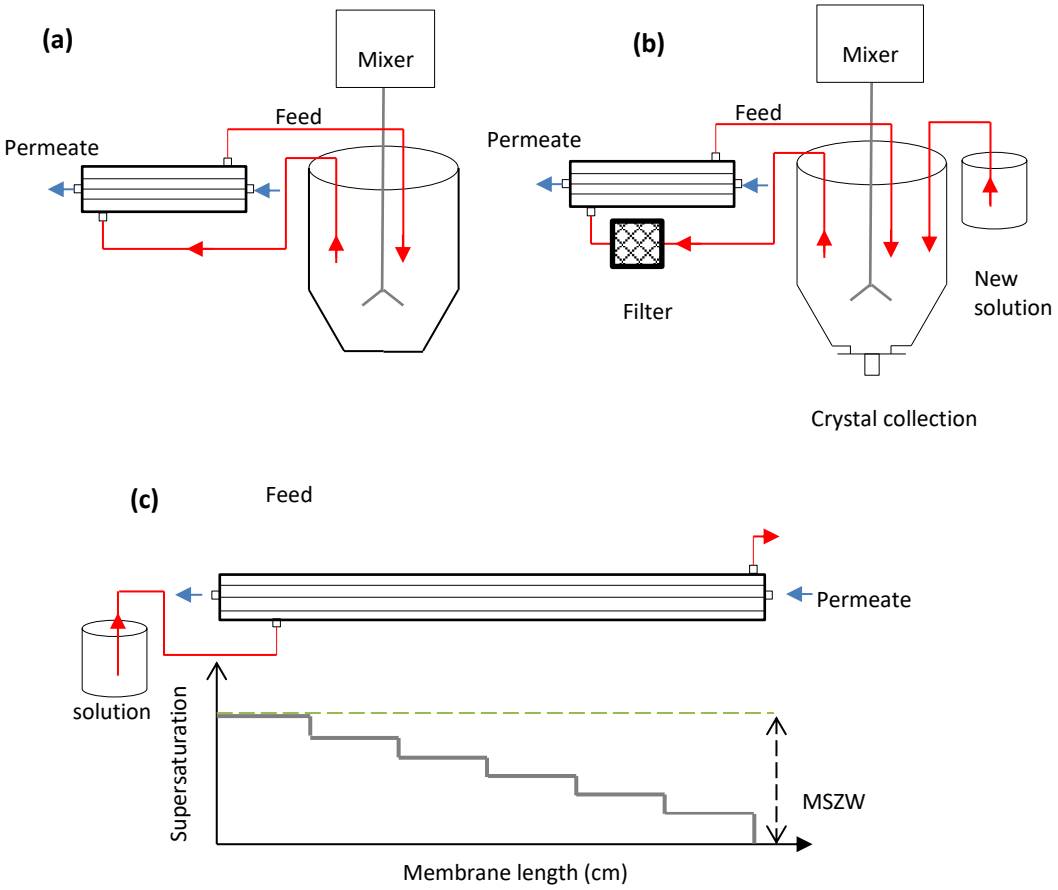

Figure 5.2 *Crystallisation design across different processes method: (a) batch crystallisation; (b) continuous batch; (c) membrane continuous flow.*

5.4 MDC is more scalable than classical crystallisation systems

Controlling the rate of supersaturation is challenging when scaling up a classical evaporative crystalliser, as it reveals critical prerequisites in the heat and mass transfer mechanism against membrane distillation crystallisation [15]. While the applied temperature will determine the extent of heat transfer within the crystalline solution in the system, the area of heat exchange is independent of the area for evaporation, in which both the heat exchanger and the surface area of evaporation will scale up differently [21–23]. This poses a complexity to match

the mass and heat transfer characteristics, particularly in large-scale crystallisers where imperfect mixing intensity is most likely to occur. This complicates both macromixing and potentially extend to micromixing, leading to a lack of supersaturation homogeneity within crystalline solution [24,25]. To illustrate, supersaturation degree is expected to be higher where this supersaturation is generated (e.g. at the crystalliser evaporation interface), whereas the process may exhibit a low level of supersaturation away from the evaporation interface. (e.g., close to the crystalliser surface) [26]. In this work, we demonstrated that control of supersaturation rate can be achieved using membrane area, which can be exploited for the informed control of supersaturation, induction time, and metastable zone when scaling-up the membrane process. This was associated with the flexible control of the boundary layer during regulating the supersaturation rate, which enables different sets of nucleation kinetics depending on the method used to modulate the supersaturation rate. To illustrate, modifying solution volume across different membrane areas (7 and 37 hollow fibre modules) allows transition across MSZW at different supersaturation rates, while this enables a comparable gradient between (LnR') and (Ln $\Delta C_{max,fm}$) for each module (Chapter 2). This means that both membranes can develop identical nucleation orders, which describe the consistency of the energy required to cross the critical barrier energy for nucleation despite the membrane area used [27]. The reproducibility at this scale suggests nucleation to be deterministic in its predictability, providing evidence that MDC is an inherently scalable technology compared to classical crystallisation systems. This approach relies more on adjusting bulk supersaturation independent of the boundary layer, which can be adapted to anticipate the boundary layer role of various aqueous salt solutions in a scalable platform technology. Furthermore, the ability to adapt the hydrodynamics (laminar in this study) to align with the desired characteristics of the boundary layer is achievable in MDC system due to the identified heat and mass transfer associated with the fixed interfacial area which is an essential facet for process scalability.

While regulating supersaturation rate using temperature is typically the only option within classical evaporative crystallisers, the control of supersaturation independent of bulk temperature (T) or temperature differences (ΔT) in this work suggests the potential to operate at lower temperature distillation which avoids the production of steam, and therefore enhances the thermodynamic efficiency of heat recovery. Furthermore, the heating devices in classical evaporative systems differ mostly in their precision to offer thermal stability, combined with the long response time to reach the target temperature which may complicate further control of supersaturation following primary nucleation [28–30]. This might preclude such a supersaturation control strategy (SSC), which is crucial during the crystallisation process scale-up to avoid the consumption of supersaturation gradient outside the constructed MSZW boundary for promoted crystal growth [31]. Furthermore, it adds complexity to the direct nucleation control strategy (DNC), which relies on particle formation to regulate the rate of supersaturation and maintains the supersaturation profile close to the growth zone threshold within MSZW [32,33]. Contrary to classical evaporative crystallisers, MDC allowed for better control over the supersaturation rate. The membrane can regulate heat and mass transfer mechanism, enabling precise control of the supersaturation level within the interfacial boundary layer and bulk solution. This can be used to decouple the nucleation and crystal growth to be adopted to different membrane based system scales. Additionally, the application of continuous flow through the membrane as a method to increase the crystal yield can be beneficial to meet the industrial requirements for a higher yield with better control over the growth phase. Therefore, MDC is expected to provide a richer suite of crystallisation kinetic trajectories by offering a well-disciplined supersaturation parameter for controlled crystallisation at an industrial level.

5.5 References

[1] M.T. Chan, A.G. Fane, J.T. Matheickal and R. Sheikholeslami, Membrane distillation crystallization of concentrated salts - Flux and crystal formation, J. Memb. Sci. 257 (2005) 144–155.

2] Y. Choi, G. Naidu, L.D. Nghiem, S. Lee and S. Vigneswaran, Membrane distillation crystallization for brine mining and zero liquid discharge: Opportunities, challenges, and recent progress, Environ. Sci. Water Res. Technol. 5 (2019) 1202–1221.

[3] X. Jiang, L. Tuo, D. Lu, B. Hou, W. Chen and G. He, Progress in membrane distillation crystallization: Process models, crystallization control and innovative applications, Front. Chem. Sci. Eng. 11 (2017) 647–662.

[4] T. Horseman, Y. Yin, K.S. Christie, Z. Wang, T. Tong and S. Lin, Wetting, Scaling, and Fouling in Membrane Distillation: State-of-the-Art Insights on Fundamental Mechanisms and Mitigation Strategies, ACS ES&T Eng. 1 (2021) 117–140.

[5] A.S. Myerson, D. Erdemir and A.Y. Lee, Handbook of Industrial Crystallization, Third Edit, Cambridge University Press, (2019) 46–63.

[6] H. Wang, V. Alfredsson, J. Tropsch, R. Ettl and T. Nylander, Formation of CaCO3 deposits on hard surfaces - Effect of bulk solution conditions and surface properties, ACS Appl. Mater. Interfaces. 5 (2013) 4035–4045.

[7] F. He, K.K. Sirkar and J. Gilron, Studies on scaling of membranes in desalination by direct contact membrane distillation: CaCO3 and mixed CaCO3/CaSO4 systems, Chem. Eng. Sci. 64 (2009) 1844–1859.

[8] D.M. Warsinger, E.W. Tow, J. Swaminathan and J.H.L. V, Theoretical framework for predicting inorganic fouling in membrane distillation and experimental validation with calcium sulfate, J. Memb. Sci. 528 (2017) 381–390.

[9] F. Edwie and T.S. Chung, Development of simultaneous membrane distillation-crystallization (SMDC) technology for treatment of saturated brine, Chem. Eng. Sci. 98 (2013) 160–172.

[10] J. Kim, J. Kim and S. Hong, Recovery of water and minerals from shale gas

produced water by membrane distillation crystallization, Water Res. 129 (2018) 447–459.

[11] M.C. Sparenberg, S. Chergaoui, V. Sang Sefidi and P. Luis, Crystallization control via membrane distillation-crystallization: A review, Desalination. 519 (2022) 115315.

[12] G. Di Profio, S. Tucci, E. Curcio and E. Drioli, Controlling polymorphism with membrane-based crystallizers: Application to form i and II of paracetamol, Chem. Mater. 19 (2007) 2386–2388.

[13] J. Hou, S. Wu, R. Li, W. Dong and J. Gong, The induction time, interfacial energy and growth mechanism of maltitol in batch cooling crystallization, Cryst. Res. Technol. 47 (2012) 888–895.

[14] A.E. Lewis, M.M. Seckler, H. Kramer, G. Van Rosmalen, Industrial crystallization: Fundamentals and applications, first Edit, Cambridge University Press (2015) 71–120.

[15] I. Ruiz Salmón and P. Luis, Membrane crystallization via membrane distillation, Chem. Eng. Process. Process Intensif. 123 (2018) 258–271.

[16] R. Naim and A.F. Ismail, Effect of fiber packing density on physical CO 2 absorption performance in gas – liquid membrane contactor, Sep. Purif. Technol. 115 (2013) 152–157.

[17] A. V Dudchenko, M. Hardikar, R. Xin, S. Joshi, R. Wang, N. Sharma and M.S. Mauter, Impact of module design on heat transfer in membrane distillation, J. Memb. Sci. 601 (2020) 117898.

[18] A. Ali, C.A. Quist-jensen, F. Macedonio and E. Drioli, Chemical Engineering and Processing : Process Intensi fi cation Optimization of module length for continuous direct contact membrane distillation process, Chem. Eng. Process. Process Intensif. 110 (2016) 188–200.

[19] M. Jiang and R.D. Braatz, Designs of continuous-flow pharmaceutical crystallizers: Developments and practice, CrystEngComm. 21 (2019) 3534–3551.

[20] B. Likozar and J. Orehek, Continuous Crystallization Processes in Pharmaceutical Manufacturing : A Review, 25 (2021) 16–42.

[21] J. Ulrich and P. Frohberg, Problems, potentials and future of industrial crystallization, Front. Chem. Sci. Eng. 7 (2013) 1–8.

[22] S.K. Jha, S. Karthikaa and T.K. Radhakrishnan, Modelling and control of crystallization process, Resour. Technol. 3 (2017) 94–100.

[23] H. Lu, J. Wang, T. Wang, N. Wang, Y. Bao and H. Hao, Crystallization techniques in wastewater treatment: An overview of applications, Chemosphere. 173 (2017) 474–484.

[24] Z. Sha and S. Palosaari, Mixing and crystallization in suspensions, Chem. Eng. Sci. 55 (2000) 1797–1806..

[25] E. Kougoulos, A.G. Jones and M. Wood-Kaczmar, CFD modelling of mixing and heat transfer in batch cooling crystallizers aiding the development of a hybrid predictive compartmental model, Chem. Eng. Res. Des. 83 (2005) 30–39.

[26] A. Jones, S. Rigopoulos and R. Zauner, Crystallization and precipitation engineering, Comput. Chem. Eng. 29 (2005) 1159–1166.

[27] K. Sangwal, A novel self-consistent Nývlt-like equation for metastable zone width determined by the polythermal method, Cryst. Res. Technol. 44 (2009) 231–247.

[28] M. Fujiwara, Z.K. Nagy, J.W. Chew and R.D. Braatz, First-principles and direct design approaches for the control of pharmaceutical crystallization, J. Process Control. 15 (2005) 493–504.

[29] A. V. Mohod and P.R. Gogate, Improved crystallization of ammonium sulphate using ultrasound assisted approach with comparison with the conventional approach, Ultrason. Sonochem. 41 (2018) 310–318.

[30] S. Fotowat, S. Askar and A. Fartaj, A Transient Response Comparison of a Conventional and a Meso Heat Exchanger under Mass Flow and Temperature Step Changes, J. Fluid Flow, Heat Mass Transf. 8 (2021) 199–216.

[31] I. Ostergaard, B. Szilagyi, H.L. De Diego, H. Qu and Z.K. Nagy, Polymorphic Control and Scale-Up Strategy for Antisolvent Crystallization Using Direct Nucleation Control, Cryst. Growth Des. 20 (2020) 2683–2697.

[32] D. Duffy, M. Barrett and B. Glennon, Novel, calibration-free strategies for supersaturation control in antisolvent crystallization processes, Cryst. Growth Des. 13 (2013) 3321–3332.

[33] Y. Gao, T. Zhang, Y. Ma, F. Xue, Z. Gao, B. Hou and J. Gong, Application of pat-based feedback control approaches in pharmaceutical crystallization, Crystals. 11 (2021) 1–27.

[34] M. Gryta, Concentration of NaCl solution by membrane distillation integrated with crystallization. Sci. Technol. 37 (2002) 3535–3558.

[35] F. Edwie and T.S. Chung, Development of hollow fiber membranes for water and salt recovery from highly concentrated brine via direct contact membrane distillation and crystallization, J. Memb. Sci. 421-422 (2012) 111-123.

6 Conclusions and future work

6.1 Conclusions

This thesis has introduced a strategic kinetics framework based on classical nucleation theory to decouple surface nucleation and bulk crystal growth for improved crystal quality and minimum membrane scaling. The key conclusion from the work are:

(i) The increased membrane area-to-volume ratio resulted in an elevated supersaturation rate, enabling higher nucleation rate at the upper region of the metastable zone width (MSZW), where the supersaturation differences between the bulk solution and the interfacial boundary layer were reduced to promote bulk nucleation (homogeneous) rather than surface nucleation (scaling) (Objective 1).

(ii) The measured induction time relates the extent of supersaturation at induction (metastable zone width) to nucleation kinetics according to the classical nucleation theory (CNT), which reveals two distinct scaling mechanisms: adhesion growth due to heterogeneous nucleation and crystal deposition following bulk homogeneous nucleation mechanism (Objective 1).

(iii) The employment of higher packing density modules demonstrated an increase in crystal yield with less scaling, whether through adhesion or deposition, which suggests the potential to project the applied condition in a broader range of membrane-based systems characterised by narrow channels (e.g. spiral wound) without significant scaling risk (Objective 1).

(iv) The modified membrane area-to-volume ratio delivered a set of conditions to reduce Ostwald ripening by operating at a high level of supersaturation at a low supersaturation rate (reduced crystalliser volume) , where a comparable large crystal size was observed with a narrower size distribution (Objective 2).

(v) While water flux has been thought to govern the kinetics of nucleation in many previous MDC studies, the supersaturation rate generated from multiple supersaturation parameters coupled with direct measurement of induction

time provided a broad set of nucleation kinetics for improved control of growth mechanisms and final crystal quality (Objective 2).

(vi) The modified crystalliser volume at a fixed membrane area demonstrated the potential to adjust metastable zone width without incurring significant implications from the boundary layer characteristics at which the supersaturation ratio between bulk solution and interfacial boundary layer was consistent while the supersaturation rate was increased (Objective 2).

(vii) The implementation of in-line filtration before the membrane module, along with the utilisation of an 'off-bottom just suspended' agitation rate within the crystalliser, showcased the ability to reduce scaling while maintaining a consistent supersaturation rate for an extended operating period following induction, affording enhanced crystal size and yield. However, this could not prevent a drastic drop at the last flux stage, where the supersaturation profile was unable to compensate for the higher nucleation rate associated with higher supersaturation rate conditions (Objective 3).

(viii) Modifying the membrane area-to-volume ratio controlled the supersaturation profile following induction to offset the nucleation rate, which enabled the system to reposition supersaturation within a specific region of MSZW for the advanced growth phase. The consumed supersaturation due to primary nucleation lowered the supersaturation level within the bulk crystalliser, and this lower supersaturation over a longer residence time (increased hold-up time after induction) facilitated improved crystal morphology compared to crystals grown at a higher supersaturation level within the boundary layer (Objective 3).

(ix) The opportunity to scale up the crystallisation process using a membrane distillation-based system to meet industrial requirements is applicable since both mass and heat transfer mechanisms and membrane area are scaling-up simultaneously without complex supersaturation rates, which provides a milestone towards supersaturation control strategies in future commercial MDC modules (Objective 3).

6.2 Future work

The following areas for further research were identified and summarised:

(i) Further investigation into the Ostwald ripening phenomenon is crucial to distinguishing it from agglomeration, which is more likely to occur at higher degrees of supersaturation where there is high competition between nucleation and growth.

(ii) The applied hydrodynamic condition within the membrane module (fixed velocity under laminar flow regime) enabled consistent boundary layer conditions, in which the applied supersaturation rate was able to decouple between two scaling mechanisms. However, crystal deposition was not prevented, necessitating future research into other hydrodynamic profiles (e.g. varying shear forces) for further reducing crystal deposition.

(iii) The scaling potential within membrane pores still exists despite the supersaturation rate applied and the nucleation mechanism undergone in the system. The membrane autopsy in Chapter 1 suggested membrane pores might offer favourable supersaturation conditions for crystal growth even under a high area-to-volume ratio, where a homogeneous nucleation mechanism is most likely to occur. Therefore, future studies focusing on real-time microscopy at the nano level within certain time intervals are necessary to explore the developed crystallisation within membrane pores for enhanced scaling prevention and elimination strategies.

(iv) Further research on introducing mixing salts (thermodynamically distinct) with different volume-free energy and surface-free energy would be beneficial to investigate the influence of salt interactions on nucleation kinetics and scaling mechanisms. A thermodynamically distinct salt with different solubility may affect the solubility of other salts, leading to changes in the overall crystallisation process. This might involve complex nucleation and growth rates resulting in different crystal sizes and size distributions in the bulk, as well as scaling mechanisms in the membrane boundary layer. Therefore, exploring different concentration ratios of the solutes would be the first step in determining whether mixing salts can be effectively crystallised under

conditions of controlled kinetic trajectories and minimum scaling, or whether pre-treatment is required before the MDC process to eliminate specific salts and simplify the crystallisation process.

(v) Although in-line filtration successfully extended the operational conditions by reducing crystal deposition, the continuous supersaturation rate could not be maintained after a significant process point failure due to the presence of tiny crystals that could bypass the filtration device and deposit on the membrane. This highlights the necessity of upgrading the process to a fully continuous operating method, where the introduction of fresh solution can dissolve these tiny crystals, allowing for the repositioning of the supersaturation trajectory within the boundary of the metastable zone width (MSZW), while the in-line removal of larger crystals can help prevent blockage in the system.